UNIVERSITÀ
DEGLI STUDI
FIRENZE

DOTTORATO DI RICERCA IN INGEGNERIA INDUSTRIALE
CICLO XXIX
COORDINATORE: *Prof. Ing. Maurizio De Lucia*

Development of Predictive Models for Synchronous Thermal Instability

Settore Scientifico Disciplinare: ING-IND/08 - *Macchine a Fluido*

Dottorando: Ing. Duccio Griffini

Tutore: Prof. Ing. Francesco Martelli

Co-Tutore: Dr. Ing. Daniele Panara

Coordinatore: Prof. Ing. Maurizio De Lucia

Anni 2013/2016

Alla mia Famiglia

Acknowledgements

I wish to thank Prof. Francesco Martelli for having supported my PhD activity and for the precious suggestions provided during all the research period. I would like to express sincere thanks to Dr. Daniele Panara and Dr. Simone Salvadori, whose support and useful advices have been fundamental for reaching the results presented in this work.

Special thanks go to Dr. Alessandro Mattana with whom I have collaborated for obtaining some of the results presented in this thesis. Moreover, Dr. Andrea Rindi, Dr. Enrico Meli and Mr. Simone Panconi, from the MDMlab of the Department of Industrial Engineering of the University of Florence, are acknowledged for their precious contributions to the work. Finally, Dr. Massimiliano Insinna, Dr. Alessandro Cappelletti, Dr. Adriano Spadi, Dr. Chiara Bernardini and all the other members of the "TCR" research group of the Department of Industrial Engineering of the University of Florence are sincerely acknowledged for the help and friendship demonstrated in all of these years.

"O frati", dissi "che per cento milia perigli siete giunti a l'occidente, a questa tanto picciola vigilia d'i nostri sensi ch'è del rimanente, non vogliate negar l'esperienza, di retro al sol, del mondo sanza gente. Considerate la vostra semenza: fatti non foste a viver come bruti, ma per seguir virtute e canoscenza".

Dante Alighieri (Inferno XXVI, 112-120)

Abstract

The increasing demand of higher efficiency and increased equipment compactness is pushing the modern rotordynamic design towards higher and higher bearing peripheral speed. Due to the increased viscous dissipation, modern fluid film bearings are prone to the development of complex thermal phenomena that, under certain conditions, can result in synchronous thermal instability, often referred to as Morton effect.

Although the phenomenon is known and studied from the late 1970s a lack of knowledge is highlighted in literature and the strategy to approach its prediction and analysis is yet debated within the scientific community.

This work presents the development and validation of the numerical models for the prediction of the synchronous thermal instability. The proposed models are derived from a preliminary analysis of the physical time scales of the problem and of the orders of magnitude of the equations, which allowed an aware selection of the modelling strategies from a dual point of view: the physical genesis of the Morton effect (i.e., the differential heating of the shaft) and the assessment of the stability of the rotor-bearing system under the influence of the thermal effects.

Particular focus is devoted to the fluid-dynamical problem with the description of two dedicated codes, developed, respectively, for the analysis of the thermo-hydrodyanmics of fluid film bearings and for the modelling of the differential temperature developed across the shaft. This latter phenomenon is due to the differential heating and results to be the driving parameter of the problem.

Once the two codes has been individually validated, these have been

inserted in more complex systems in order to evaluate their ability to enable the prediction of the Morton effect. A linear stability analysis has been firstly performed and results, although affected by discrepancies with respect to the experimental data, have shown the potential of the codes to reach the objective of the work. Better results have been finally obtained when the models have been inserted in a more complex architecture. This latter has been developed in collaboration with the MDMlab of the Department of Industrial Engineering of the University of Florence in order to model the synchronous thermal instability by means of an iterative approach. A comparison with available experimental data, derived from a dedicated test campaign carried out at the GE Oil & Gas facility in Florence, is shown in order to validate both the procedure and the models. Moreover, some key parameters driving the Morton effect are presented and a study of the sensitivity of the phenomenon to the thermal expansion coefficient is proposed in order to improve researchers' knowledge on the topic.

Contents

List of Figures

List of Tables

Nomenclature

Acronyms

API	American Petroleum Institute
CFD	Computational Fluid Dynamics
CHT	Conjugate Heat Transfer
FDM	Finite Difference Method
FEM	Finite Element Method
$FFTB$	Flux Forward Temperature Back
GE	General Electric
$hFFB$	heat transfer coefficient Forward Flux Back
$hFTB$	heat transfer coefficient Forward Temperature Back
HTC	Heat Transfer Coefficient $[W/(m^2K)]$
LBP	Load Between Pads
LE	Leading Edge
LOP	Load On Pad
NDE	Non-Drive End side
NP	Number of pads of the tilting pad
ORC	Over-Relaxation Coefficient
PAM	Pad Assembly Method
PJB	Plain Journal Bearing
$TFFB$	Temperature Forward Flux Back
THD	Thermo-HydroDynamic
$TPJB$	Tilting Pad Journal Bearing
URC	Under-Relaxation Coefficient

Letters

A, B, C	Terms of the linear stability analysis	
B	Bearing axial length	$[m]$

Bi	Biot number	$[-]$
Br	Brinkman number	$[-]$
C	Radial clearance, Damping coefficients	$[m]$, $[N \cdot s/m]$
c	Specific heat	$[J/(kg \cdot K)]$
D	Diameter	$[m]$
Fr	Froude number	$[m]$
H	Heat transfer coefficient	$[W/m^2 \cdot K]$
h	Film-thickness	$[m]$
k	thermal conductivity	$[W/m \cdot K]$
K	Spring coefficients	$[N/m]$
Kn	Knudsen number	$[-]$
L	Static load	$[N]$
m	Preload	$[-]$
$MT3$	Turbulence model with the constants of Hirs	
NX, NY, NZ	Number of grid elements along x, y, z	$[-]$
$NR, N\delta, NZ$	Number of grid elements along r, δ, z	$[-]$
$\dot{m}$	Mass flow rate	$[kg/s]$
p	Pressure	$[Pa]$
Pe	Peclet number	$[-]$
Pr	Prandtl number	$[-]$
Pf	Frictional power	$[W]$
q	volumetric oil flow (recirculation)	$[m^3/s]$
$\dot{q}$	Thermal flux	$[W/m^2]$
R	Radius	$[m]$
r	Radial coordinate	$[m]$
Re	Reynolds number	$[-]$
Re_s	squeeze Reynolds number	$[-]$
Re^*	modified Reynolds number	$[-]$
So	Sommerfeld number	$[-]$
T	Temperature	$[K]$
t	Time	$[s]$
Ta	Taylor number	$[-]$
u, v, w	Flow velocity	$[m/s]$
U, V, W	Shaft speed	$[m/s]$
x_1, x_2, x_3	Local spatial coordinates	$[m]$
x, y, z	Local spatial coordinates	$[m]$
X, Y	Global spatial coordinates	$[m]$

Greek Letters

α	angular coordinate; relaxation coefficient	$[rad]$; $[-]$
α'	angular coordinate	$[rad]$
α''	angular coordinate	$[rad]$
β	exponent of the Reynolds equation, shaft bowing angle	$[K^{-1}]$,$[rad]$
γ	attitude angle	$[rad]$
Γ	Boundary condition	
δ	tangential coordinate	$[rad]$
ϵ	relative eccentricity or thermal strain	$[-]$
η	effectiveness	$[-]$
θ	tilt angle of the pad	$[rad]$
$\dot{\theta}$	tilt angle velocity	$[rad/s]$
Θ	reference differential temperature	$[K]$
ι	corrective term for the mixing model	$[-]$
λ	thermal expansion coefficient	$[K^{-1}]$
Λ	film parameter (lubrication regimes)	$[-]$
μ	Dynamic viscosity	$[Pa \cdot s]$
ν	Kinematic viscosity	$[m^2/s]$
ρ	Density	$[kg/m^3]$
σ	Standard deviation	
τ	time scale	$[s]$
τ_{ik}	i,k element of the viscous stress tensor	$[Pa]$
ϕ	phase of the B term, hot spot position	$[deg]$, $[deg]$
Φ_{ij}	displacements phase, dissipation function	$[deg]$, $[W/m^3]$
ψ	phase of the differential temperature	$[deg]$
Ω	rotational speed	$[rad/s]$

Subscripts

0	referred to equilibrium position/feeding oil
1	referred to inlet section
2	referred to outlet section
amb	referred to the external ambient
ave	average or effective
app	applied value
ax	in axial direction
b	referred to the assembled clearance or to the bush
$bush$	referred to the bush

$calc$	calculated
cav	cavitated
cht	referred to convective heat transfer term
$crit$	critical
des	referred to design
eff	effective
f	referred to friction
fcd	referred to the fluid conduction term
fcv	referred to the fluid convection term
fd	referred to the fluid viscous dissipation term
$flow$	referred to the oil flow
in	inlet
$i-th$	referred to the i-th value
j	referred to the journal (shaft)
lat	referred to the lateral surface of the domain
m	referred to the m-th element
max	maximum
$m, mean$	mean value
min	minimum
mod	modeled
mwa	mass-weighted average
$n.d.$	non-dimensional
$press$	referred to the pressure
pso	points around the orbit
oh	overhung
oil	lubrication oil
out	outlet
p	pad machined (bearing clearance)
$pad/pads$	referred to the pad/pads
pjb	referred to plain journal bearing
rec	recovery
red	reduced
ref	reference quantity
s	referred to solid (shaft, pads and bush)
sc	referred to the solid conduction term
$shaft$	referred to the shaft
t	referred to turbulent quantity
TLP	referred to TILTPAD
td	referred to the solid thermal deformation
th	thermal

tpjb	referred to tilting pad journal bearing
u	unitary value
wall	referred to the wall

Superscripts

$*$	non-dimensional
$\star$	value effectively calculated

Symbols

$\overline{[\,]}$	Vector
$\tilde{[\,]}$	Differential (temperature)

Introduction and motivations of the work

The demand of higher efficiency and increased equipment compactness is pushing modern rotordynamic design towards higher and higher bearing peripheral speed. As a consequence, due to the increase in viscous dissipation, modern fluid film bearings are prone to the development of complex thermal phenomena, which heavily affect the machine rotordynamics. In detail, the increased viscous dissipation generates rotor asymmetrical heating (see the work of De Jongh and Morton [1]), which drives the formation of a differential temperature across the shaft and hence induce thermal rotor bowing. This latter, generates rotor thermal imbalance and can consequently increase synchronous vibrations. Since differential heating and synchronous rotor vibration are directly linked, a complex feedback loop can be generated causing, in the worst scenario, the thermal rotor instability, which is often referred to as Morton effect.

Since the described problem is strictly related to the increase in machine performance, a raising interest on the topic has been shown both from the academical and industrial communities. This trend has been also recently confirmed by the introduction, in 2005, of a dedicated chapter in the second revision of the American petroleum Institute rotordynamic tutorial (API Recommended Practice 684 [2]), demonstrating also the recognition of the technological challenge to be solved by the industrial community.

Although the phenomenon has been recognized and studied for the

first time during the late 1970s, a lack of knowledge is nowadays yet highlighted in literature, as underlined in the work of De Jongh [3], dated 2008, where is clearly stated that "synchronous thermal instability, due to bearing journal differential heating, is not a well-known rotordynamic phenomenon". Furthermore, the technological challenge results to be yet discussed. In fact, the API rotordynamic tutorial reports that "while synchronous thermal instability fits the classical definition of an unstable system, rotor stability codes are currently not used to predict its existence".

Motivated by the aforementioned lack of knowledge, this thesis, realized in collaboration with GE Oil & Gas, presents the development and validation of numerical codes to be used for the prediction of the Morton effect. The purpose is pursued always having in mind the need for a trade off between accuracy and computational costs in order to obtain an useful tool attractive also for the industrial community.

The activity has been divided into two parts. The first one is dedicated to the development and validation of numerical codes both for the thermo-hydrodynamic analysis of plain and tilting pad journal bearings and for the calculation of the differential temperature developed across the shaft. A discussion and quantification of the uncertainties in the operating conditions is also considered. The second part is aimed to validate the numerical codes in way to prove their ability to identify the onset of the synchronous thermal instability. Moreover, some key parameters driving the Morton effect are studied in order to identify strategies of solution and improve researchers' knowledge of the phenomenon.

Before the two aforementioned parts, a description of the problem, with its implications, and a literature survey are proposed. These, are aimed to characterize the physics and evaluate the solution strategies currently considered by researchers. The objective of this latter analysis is to enable an aware discussion, based on some physical considerations, in order to select the best strategy to be adopted for the purpose of the work.

Chapter 1

Synchronous thermal instability: physics

Contents

Thermal phenomena in rotordynamics are known from the early years of the 20^{th} century, when Newkirk published a work [4] concerning a thermally-induced problem affecting a water wheel generator. The presented unit experienced severe vibrations, which abruptly increased in the space of a few minutes, necessitating a machine shut-down. Observations showed that the shaft was bowed immediately after shut-down and that the bow disappeared after a few minutes. Newkirk concluded that the problem was due to rubbing of the shaft against the bearing, which promoted the generation of an hot-spot on the surface of the rotating shaft. He also reported the following considerations: "if the journal becomes heated along one element of its surface, the shaft bows so that this

element is pressed against the bearing and becomes still hotter, which results in further bowing, etc. Thus, when a cycle of this sort starts it progresses rapidly, and violent vibration develops". Moreover, referring to an experimental campaign made at the General Electric Company's research laboratory, Newkirk observed that if the shaft was running below its first critical speed then the rubbing increased in intensity as a consequence of a positive feedback mechanism. On the contrary, when operated above its critical speed the rubbing, if not too severe, was not able to build up. This phenomenon is nowadays known as Newkirk effect.

Further study on the phenomenon has increased researchers' knowledge highlighting that the light rub can be promoted for different rub locations (e.g., bearings, seals and oil deflectors) and, more recently, that it can affect high-speed turbomachinery rotors running above the first critical speed. In such a background the work of Dimarogonas [5] was the first to quantitatively evaluate the Newkirk effect and indicated its three different modes: a spiralling one, with vibrations increasing in time, an oscillating one, which consisted in constat-amplitude sinusoidal vibrations, and a constant mode, with time-independent vibrations. Dimagoronas concluded that the main factor determining the mode of the system is the phase difference between the static mechanical bow and the dynamic thermal bow, both evaluated with respect to a reference system fixed with the spinning rotor.

In the late 1970s another thermal phenomenon has been considered as a root cause for the synchronous thermal instability. Better known as Morton effect, this latter is the main topic of the present work. It has strong similarities with the Newkirk effect, particularly in the way the feedback mechanism drives the system towards instability, but the hot spot has a different physical genesis, which, in this case, is related to the viscous dissipation within the bearings.

Although this thermo-hydrodynamic source for the shaft differential heating has been recognized for the first time during the 1970s, it is only in 1987, with the work of Schmied [6], that this mechanism has been proposed in the open literature as a root cause for the rotor spiral vi-

brations. In fact, according to the work of De Jongh [3], the pioneering study of the synchronous thermal instability, performed at the General Electric Company Ltd. in the United Kingdom and at the Stal-Laval Turbin AB in Sweden respectively by Morton [7], [8] and Hesseborn [9] during the late 1970s, are internal reports which are not widely available. Fortunately, information about these works are given in the work of De Jongh [3]. According to this latter, Morton, in 1975, performed an experimental campaign on a 711 mm diameter shaft running at 1800 rpm. The temperature distribution along the tangential direction of the shaft at the bearing section was measured by means of 12 thermocouples equally spaced on the circumference. It was found that significant differential temperatures were measured across the shaft for orbits of only a few percent of the radial clearance, without any rubbing. This has been the first experimental proof of the shaft differential heating due to viscous dissipation and, due to this work, the consequent rotor thermal instability is usually referred to as Morton effect.

Nowadays, the Morton effect is gaining more and more attention from the turbomachinery community due to the increasing number of registered events. This is due to two main reasons: the first one is objective and is due to the trend adopted by the turbomachinery producers of increasing the rotational speed, the second one is instead subjective and is due to the increase in awareness of the phenomenon. In fact, the increased rotational speed, which pursue the need for increasing the turbomachinery performance, practically induce an increase in the frequency of the spiral vibration events, particularly if overhung rotor (or couplings) configurations are considered. At the same time, the increase in the number of events is related to the ability and opportunity to detect the phenomenon that is given by the increase in Morton effect's knowledge. Since this kind of thermal instability can be experimentally recognized only measuring the temperature across the shaft, which is not an easy task, it is possible to imagine that before some general rules of the phenomenon were given, some cases of Morton effect could have not been recognized nor even hypothesized. In fact, from the work of

the De Jongh [3], which gives an excellent historical excursus, Morton reports that prior to the 1975 several empirical approaches were used by its company to cure the rotordynamic problems, without having an in depth comprehension of the physics behind them. Referring to the words of Morton it is stated that "a reduction on overhang mass proved beneficial and another approach was simply to increase the bearing clearance, so that the cooling oil flow was increased". In a number of cases, he indicated that "it was sufficient to wait until the troublesome machine was rigidly coupled to another machine, thereby reducing the overhang sensitivity". All of the cited empirical approaches highlight some of the parameters which have been shown over the years to play a key role in driving the Morton effect.

The increase in attention revealed by the scientific community, as stated in the introduction of the present work, can be confirmed observing Figure 1.1, taken from the work of Panara et al. [10], which is in turn taken and integrated from the work of De Jongh [3]. It shows an overview of the number of publications related to the Morton effect from the 1975, year of the first known study, up to the end of the 2014. As it is possible to observe a trend underlying the increase in interest is clearly defined.

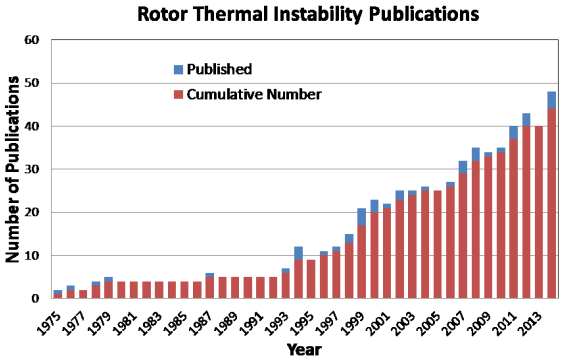

Figure 1.1: Number of technical publications about the rotor thermal instability over the years, from the work of Panara et al. [10].

From the point of view of the industrial community, such an increase in attention is confirmed by the fact that rotor thermal instability has gained a dedicated chapter in the second revision, dated 2005, of the American Petroleum Institute rotordynamic tutorial [2], demonstrating that the rotor thermal instability is more and more recognized as a technological challenge whose solution is still to be debated in the technical community.

Although the increasing interest has driven researchers towards a better knowledge of the phenomenon, De Jongh [3], in 2008, states that the Morton effect is yet "not a well known rotordynamic phenomenon". Moreover, in the closure of the cited API Recommended Practice 684 is reported that "while synchronous thermal instability fits the classical definition of an unstable system, rotor stability codes are currently not used to predict its existence". This highlighted lack of knowledge has encouraged the present work in order to overcome current code limitations and present some instruments for the Morton effect prediction and analysis.

1.1 Introduction to the physics of the problem

In this first chapter an overview of the physics of the thermal rotor instability is given. The purpose is to highlight its main characteristics and underline similarities and differences with the more famous Newkirk effect.

As previously stated, synchronous thermal instability, better known as Morton effect, is driven by non-uniform bearing journal heating. This is an uncommon approach since, in the traditional bearing literature, the shaft is considered with a uniform journal heating and hence, with uniform temperature distribution. This latter hypothesis is a fair assumption when the shaft rotates on its stable equilibrium position but is no more reliable when the journal orbits around its stable equilibrium position with a whirling frequency synchronous with respect to the rotor speed. As it is possible to imagine, this second condition results to be a more realistic

scenario due to the residual mechanical imbalance, which characterize real rotordynamic applications and which results to be unavoidable.

Research confirmed the previously cited mechanism and has shown that during a synchronous orbit, rotors supported in fluid film bearings exhibit a non-uniform temperature distribution. According to API684 [2] this unavoidable thermal gradient can be explained as follow: "one specific point on the shaft will always be on the outside of the orbit and will therefore be closer to the bearing wall (see Figure 1.2). This surface will have a smaller film thickness averaged over the period of one orbit than the opposite side of the shaft". This point of minimum film-thickness is referred to as high-spot.

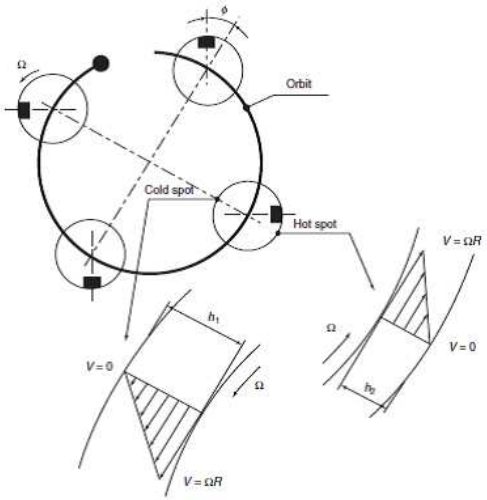

Figure 1.2: Differential heating mechanism from the second revision of API684 standard [2].

Since oil temperature is directly proportional to the amount of viscous dissipation, which in turn is directly proportional to the viscous shear, it is easy to understand that oil temperature grows inversely with respect to the oil film thickness, producing a hot and cold spots on the rotating shaft.

The larger the size of the orbit, the larger the differential temperature will be. The obtained rotating thermal gradient, determines shaft thermal bending (see Figure 1.3) and hence rotor thermal imbalance is generated. If the increased thermal imbalance couples positively with vibration orbit enhancement, the resulting feedback loop can drive the rotor unstable in the sense that the synchronous vibration will grow unbounded.

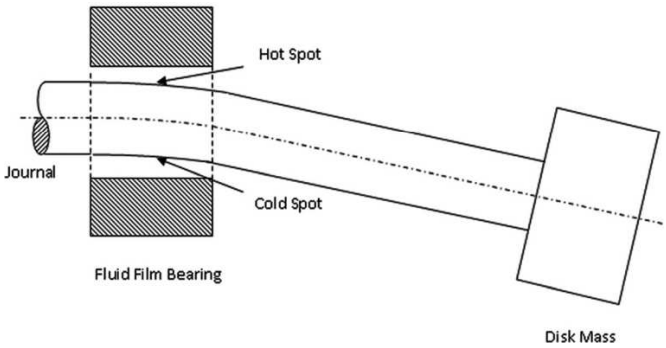

Figure 1.3: Thermal bending inside of the bearing section from the work of Guo and Kirk [11].

Looking at the problem from a general view it is possible to observe three main actors driving the phenomenon. These three main physical aspects interconnected in a loop to each other, shown in Figure 1.4, constitute the Morton effect core: the mechanical imbalance generates an elliptical orbit, which generates a thermal gradient across the shaft, which in turn generates a thermal bending and, as a consequence, thermal imbalance is added to the initial mechanical imbalance closing the loop.

Due to the variety of the phenomena involved, showing the Morton effect's highly inter-disciplinary nature, different models with different degree of complexity have been proposed over the years. All of these models confirm that, in order to approach and study the problem, the three proposed terms (highlighted in Figure 1.4) need to be numerically, analytically or empirically defined.

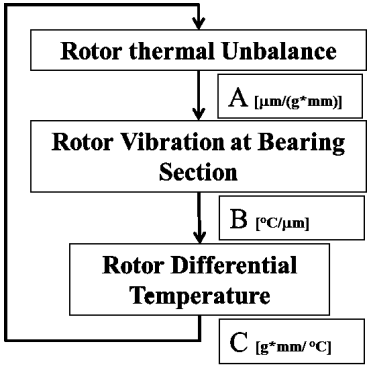

Figure 1.4: Rotor thermal instability loop, from the work of Panara et al. [10].

The three terms can be summarized as follow:

- the link between thermal imbalance and rotor vibration at bearing section (hereafter referred to as A term);
- the link between rotor vibration at bearing section and rotor differential heating (hereafter referred to as B term);
- the link between rotor differential heating and thermal imbalance (hereafter referred to as C term).

Among all of these terms the most challenging one remain the B term, which connects the vibration orbit to the thermal gradient. In fact, it relates two very different problems and involves the unsteady thermo-hydrodynamic analysis of the oil within the film-thickness of the bearing, managing the dynamics of the shaft and the pads, thermal and elastic deformations, oil cavitation as well as the heat transfer and heat conduction within the shaft, pads and housing. Such a problem is characterized by very different length and, above all, time scales. These latter, constitute the main challenge and entail different choices to approach the problem on the base of the needed level of accuracy and efficiency.

1.2 Main characteristics of the phenomenon

Along this section the main characteristic of the phenomenon are considered. The objective is to present some general rules regarding the Morton effect and have a comparison with the more famous Newkirk effect.

The vibrations related to both the thermal phenomena presented are synchronous ($1x$) with respect to the rotor running speed. Moreover, in both cases the Nyquist plot is composed of a spiral vibration at constant rotor speed due to the moving hot-spot, which induce the thermal bending. Although under certain aspects the behaviour is very similar, some characteristics can help in recognizing the Morton effect between the two. First of all, the Newkirk effect is associated with rubbing, hence, signs of the erosion have to be found on statoric or rotoric components. Moreover, shaft orbit plots register usually smooth variations in case Morton effect is developing, while, on the contrary, the Newkirk effect shows clear signs of the bounces taking place when rubbing occurs, as shown in the work of Phuttipongsit [12]. The effect of the bounces is clearly visible in Figure 1.5 where a typical shaft orbit plot of a machine experiencing Newkirk effect is presented.

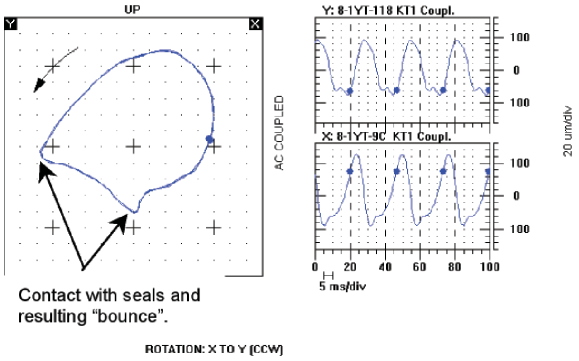

Figure 1.5: Shaft orbit plot of a mechanical drive steam turbine experiencing seal rub, from the work of Phuttipongsit [12]

Another difference between Newkirk and Morton effects is reported in the work of De Jongh [3]. The author states that the Morton effect can show instability upper limit, and hence, the phenomenon can occur in more than one speed range. In fact, De Jongh recall the results from an experimental campaign carried out by De Jongh and Morton [1], where the tested rotor was run through an instability zone with a regain in stability at higher peripheral speed.

Time scales also characterize the problem. Both Newkirk and Morton effect, as thermal problems, involve the thermal inertia of the solid parts (e.g., shaft, pads, bush). As a consequence, very high thermal time scales are related to these phenomena, as presented in the work of Newkirk [4], where experimental observations made immediately after one of the events of thermal vibration "indicated that the shaft was bowed in its lowest section, and that the bow disappeared within a few minutes after shut-down." A characteristic hysteresis loop is the direct consequence of the thermal time scales and is shown in Figure 1.6. If the shaft is running at a constant rotational speed the vibration slowly increases due to the highlighted thermal mechanisms, when a quick reversal of the speed is performed an hysteresis loop raises since time is needed by the shaft bending to restore its original configuration.

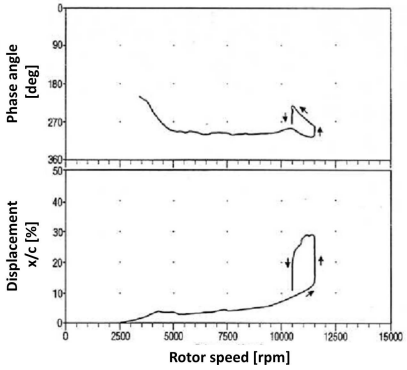

Figure 1.6: Typical hysteretical bahaviour when performing a quick reversal of machine speed (De Jongh [3])

Another characteristic of the Morton effect is a phase lag existence between the high and the hot spots, where instead in the Newkirk effect, which is driven by a different genesis of the hot spot, this latter coincide with the point where the shaft rubbing occurs. The thermal mechanism which generates the shifting between the phases, see Figure 1.7, is explained in the work of De Jongh [3]. In his work, the author reported that the oil is convected counter to the journal rotation with respect to the axis and, as a consequence, "the hot spot must lag the high spot". Although this difference could be used for distinguishing between the phenomena, it has to be considered that the knowledge of the phase lag can be obtained only if data of the shaft circumferential temperature distribution are available.

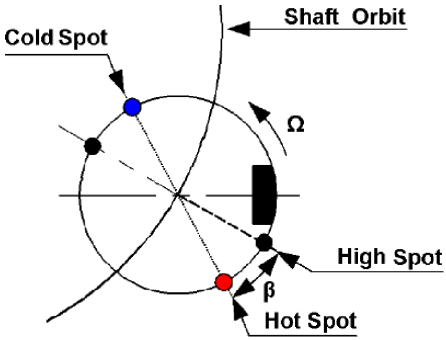

Figure 1.7: Detail of the journal cross-section showing the phase lag between hot-spot and high-spot, taken from the work of De Jongh [3].

Due to the lack of dedicated experimental campaigns, information about the phase lag are yet debated. De Jongh and Morton [1] experimental measurements, obtained on a test rotor at a speed of 10500 rpm, showed a phase lag of about 20 deg with the hot spot lagging the high spot. A range from 0 deg to 60 deg, with the hot spot lagging the high spot, is reported in the work of Murphy and Lorenz. Gomiciaga and Keogh [13] calculated by means of CFD analysis the thermal gradient across the shaft in plain journal bearings ongoing a forward or a back-

ward circular orbit. They found that the maximum journal surface point was always upstream or downstream from the point of minimum dynamic film thickness respectively for a forward and backward whirl orbit. Finally, in the work of Suh [14] a range between -20 *deg* and $+60$ *deg* is reported, where a positive value means that the hot spot is lagging the high spot.

Another characteristic which can be used from vibration analysts on field in order to distinguish between the two effects is the feeding oil flow rate. In fact, only the Morton effect, which is related to the viscous shear, is directly driven by this parameter.

Some of the main similarities and differences between the Newkirk's and Morton's effects are resumed in Table 1.1.

Characteristic	Newkirk effect	Morton Effect
rotor motion	synchronous	synchronous
rotor overhung	not required	generally required
coupling overhung	not required	generally required
hot spot cause	rotor-stator rubbing	viscous shearing
hot spot location	seals, bearings, oil deflectors	inside bearings
time scales	long (conduction)	long (conduction)
hysteresis	yes	yes
phase lag (hot-high)	no	yes
mechanical erosion	yes	no

Table 1.1: Main similarities and differences between Newkirk and Morton effects.

1.3 Consequences of the phenomenon

The described self-feeding loop which composes the Morton effect can have very different consequences on the rotordynamic behaviour depending on its intensity. In particular, three main behaviours can be obtained: a stable behaviour (generated by a converging spiral), with bounded and fixed vibrations, a marginally stable or "borderline" behaviour (usually obtained in proximity of the spiral instability threshold), with bounded but oscillating vibrations, and an unstable behaviour with its typical spiral vibrations. Converging, borderline and diverging vibrations, calcu-

lated for a two overhung impeller turboexpander in the work of Grigorev et al. [15], are shown in Figure 1.8. The black circle marker on the plots represent the starting point of the calculation, that is the resulting vibration considering the residual mechanical imbalance only.

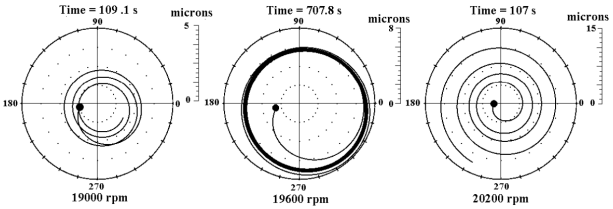

Figure 1.8: Spiral vibrations in polar plot for a two impellers overhung turboexpander, presented in the work of Grigorev et al. [15].

More in detail, the stable behaviour drives the system towards a steady vibration operating point which is generated by means of a blend between the residual mechanical unbalance and a fixed constant thermal unbalance (generated by a converging thermal spiral). When on the threshold between stable and unstable behaviour, the vibration response is a circle centered on the point of the corresponding stable solution (generated by an oscillating thermal unbalance). Finally, the unstable behaviour is generated by the typical spiralling thermal imbalance. A representation of the typical thermal behaviours from the work of Murphy and Lorenz [16] is presented in Figure 1.9.

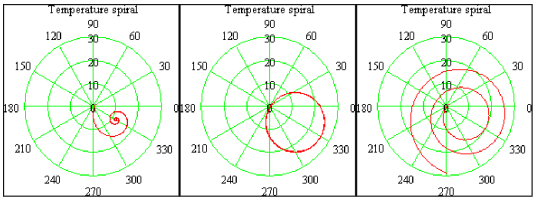

Figure 1.9: Examples of thermal spirals from the work of Murphy and Lorenz [16].

These sets of general behaviours can lead to very different working

conditions. As it is possible to observe from the following proposed subdivisions, it is not necessary to operate in a spiral vibrations regime for a designed machine to be rejected, although this latter is of course the worst scenario in terms of safety in operation. The aim of the following list is to present the consequences of the phenomenon in relation with industrial recommended practices and with customer needs and expectations since both these factors have an impact from the economic point of view.

Stable behaviour:

- No synchronous vibration change is obtained: vibrations are unaffected by the thermal phenomenon;
- Bounded and acceptable vibration change: vibrations are represented by converging spirals on a Nyquist plot to a single value of phase and amplitude which is acceptable considering API standards;
- Bounded and acceptable but unusual: vibrations are represented by converging spirals on a Nyquist plot to a single value of phase and amplitude which is acceptable considering API standards, but the vibrations exceed the customer expectations;
- Bounded and unacceptable vibration change: vibrations are represented by converging spirals on a Nyquist plot to a single value of phase and amplitude which is not acceptable considering API standards.

Marginally stable behaviour (borderline):

- Bounded and acceptable vibration change: the vibrations realize circles on the Nyquist plot. Amplitude and phase oscillates between a maximum and a minimum values which are within the API standards acceptability;
- Bounded and acceptable vibration change, but unusual: the vibrations realize circles on the Nyquist plot. Amplitude and phase

oscillates between a maximum and a minimum values which are within the API standards acceptability, but the maximum vibrations exceed the customer expectations;

- Bounded and unacceptable vibration change: the vibrations realize circles on the Nyquist plot. Amplitude and phase oscillates between a maximum and a minimum values which are outside of the API standards acceptability;

Unstable behaviour:

- Unbounded vibration change: the vibrations realize diverging spirals on the Nyquist plot. Vibrations grows unbounded with continuous phase change. The machine needs an immediate shutdown.

Only three among the eight possible operating conditions results to be completely acceptable both by norms (e.g., API standards) and customer needs and expectations.

1.4 Driving parameters and corrective actions

All of the variables related to the rotor, to the journal bearings, to the operating conditions and the ambient surrounding the system can have a role in the phenomenon, as for example: the geometry both of the rotor and the bearings, the construction materials both of the rotors and the bearings, the residual imbalance, the oil characteristics in terms of viscosity and temperature (which are strictly connected), the couplings with other machineries and so on. Among all of this variables, only the most important driving parameters will be reported further and for each one of them some corrective actions presented.

From the existing literature it has been highlighted that the Morton effect can be observed either during the preliminary testing or when the machine is installed on the field. In both cases, this kind of problem arises for newly designed machineries or when modifications to an existing one have been done. Depending on the stage of the project where the Morton effect reveal itself, some corrective actions result to be less or

more attractive. In fact, if for example the phenomenon is highlighted in a preliminary phase, some design parameters can be simply modified (e.g., rotor material or geometry). The same parameters, if modified when the machine is on the field would cause a strong increase in costs and time delay of the whole project. This highlights once more, if necessary, the importance of the development of predictive models dedicated to the present problem.

Morton effect is usually related to fast spinning machines with highly flexible rotors and high overhung masses. Moreover, it has been stated that the heat exchange within the bearing is the main driving parameter. As a consequence, it is easy to imagine that the corrective actions will be devoted to increase rotor stiffness, to decrease the heat input inside of the shaft and finally to increase the heat elimination in the bearing area.

Once the synchronous thermal instability has been recognized has the root cause for the vibration problem, the following parameters and corrective actions can be considered:

- Limit the operating/design speed: by means of this modification the vibration level usually decreases. It has to be noted that this parameter is usually not considered since it negatively affects the machine performance. Moreover, in certain cases it could not be possible to modify the working frequency or simply it would be expensive due to the required control systems (as in the case of electric motors).

- Reduce the overhung moments: overhung masses can be reduced choosing lighter materials for rotors and for couplings, as for example titanium or aluminium. This approach, successfully applied on a drive-through compressor rotor by De Jongh and Morton [1], can be easily adopted if the problem has raised during the design phase and only if the application of the machine allow the selection of materials with different physical properties (e.g., mechanical or thermal resistance).

- Modify the rotor shaft: this action can be done for having a dif-

ferent mechanical behaviour, a different thermal behaviour or both of them. In particular, the geometry of the shaft can be modified in order to obtain a stiffer configuration, as presented in the work of Schmied et al. [17], where the thrust collars have been eliminated and the diameter of the central section of the shaft increased. The material of the shaft can be also modified, in order to reduce the thermal expansion coefficient. In the work of De Jongh [3] is reported to consider, if possible, a ferritic steel instead of an austenitic one. Some considerations on construction steel composition, in relation to the phenomenon, are reported in the last chapter of the present work.

- Apply an heat barrier sleeve: this action reduces the heat input inside of the shaft applying a thermal barrier between the shaft and the oil, where viscous dissipation is produced. Presented in the work of De Jongh and Van Der Hoeven [18] this solution proved to be very effective as it is possible to observe in Figure 1.10, where the thermal gradients with and without barrier sleeve are presented.

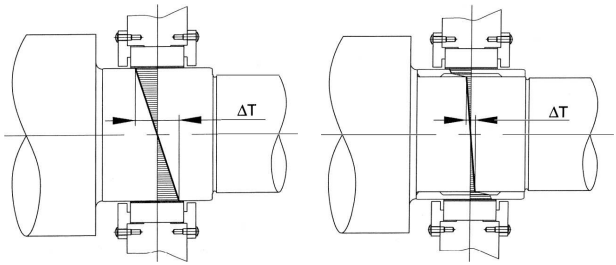

(a) Temperature distribution without heat barrier sleeve **(b)** Temperature distribution with heat barrier sleeve

Figure 1.10: Effects of the application of a heat barrier sleeve, form the work of De Jongh and Van Der Hoeven [18].

The selected thermal barrier sleeve, among all of the materials considered by the authors of the work, has been built with the same

material of the shaft and uses a small air gap as a heat barrier. Once mounted on the shaft the compressor rotor behaviour resulted to be perfect over the entire operating speed range. Moreover, the system resulted no more sensitive to the instability problem.

- Change bearing geometry: this solution, which is composed of various different actions on the parameters and geometry of the bearing, can be adopted in the phase of design but can be also attempted as a first option in case of field development of the Morton effect. In fact, it is one of the less cost effective actions.

  Many parameters can be modified: number of pads, geometry (e.g. pads' preload, clearance), the offset, the configuration (e.g. Load On Pad (LOP) or Load Between Pads (LBP)) and so on.

  Although working on the journal bearing characteristics could be one of the first choices, for the majority of the parameters presented in literature there are only a few informations about the consequences on the phenomenon. Some of these main actions will be detailed in the following.

- Change of the journal bearing clearance: when a reduction in journal bearing clearance is performed two counterposed effects are obtained. Since an increase of the viscous shear is promoted, a larger differential temperature is usually obtained. Simultaneously, the dynamic coefficients of the bearing will increase resulting in a system less sensitive to overhung unbalance. The global behaviour is then related to the effect which will dominate between the two proposed.

- Change of bearing length (change of B/D ratio): a reduction in the bearing length B increases specific or unitary loading L_u, as shown in Equation 1.1, where L represents the weight of the rotor supported by the bearing and R_j is the journal radius.

$$L_u = \frac{L}{2R_j B} \tag{1.1}$$

The increasing of the specific load drives the equilibrium position of the shaft towards higher eccentricities. As reported in the work of Balbahadur [19], an increase in eccentricity result in a better cooling effect lowering the differential temperature across the shaft. Furthermore, the increase in eccentricity of the shaft allows bigger amplitudes of the orbit motion before the bearing center is surrounded. Such a condition, that is easy to understand considering a plain bearing, magnifies the differential temperature promotion. In fact, when the orbit does not surround the center the high-spot will see an averagely minimum thickness, while if the orbit surrounds the center, the high-spot will be the minimum film-thickness condition along the whole precession motion. The reduction of the B/D ratio has been adopted for the pipeline direct inlet compressor presented in the work of Berot and Dourlens [20].

Moreover, as reported in the work of Schmied et al. [17], which applied this solution to a turboexpander with a double overhung wheels, the reduction of the axial length lower the heat input inside of the shaft, reducing the contact surface, and reduces the thermal deflection β_{th} which is proportional to the length of the section of the shaft affected by the differential temperature. Equation 1.2 reports the differential angle of the shaft evaluated between the shaft axis at the inlet section and the shaft axis at the outlet section of the bearing. In the proposed equation λ is the thermal expansion coefficient of the shaft.

$$\beta_{th} = \frac{\lambda \Delta T}{R_j} B \tag{1.2}$$

- Modify lubrication oil viscosity (μ): this action can be done by means of selection of a different lubrication oil or by the use of a different oil feeding temperature. In fact, the dynamic viscosity is function of the pressure and temperature of the fluid, $\mu(T, p)$, although for usual applications the pressure effects on the dynamic viscosity can be disregarded ($\mu(T)$). If the dynamic viscosity is

decreased the viscous shear and consequently the fluid dissipation are decreased. Thus obtaining a lower differential heat input in the shaft. This has been applied by Schmied et al. [17] on a turboexpander. It has to be noted that changing oil viscosity, all of the bearing working conditions will be affected (e.g., the eccentricity, attitude angle and dynamic coefficients). Furthermore, reducing viscosity drives the system towards a greater eccentricity value with the previously highlighted benefits.

- Increase inlet oil flow: by means of increasing the inlet oil flow, an increase in the cooling effect of the oil is obtained, reducing the differential temperature development. In contrast with this useful behaviour, having more cooling oil in the system, will increase the effective viscosity of the oil. According to the work of De Jongh [3], this solution has been applied by Morton [8] to a $61MW$ gas turbine. The clearance of the upper part of the bearing was increased resulting in a higher cooling flow rate.

- Ambient temperature: the ambient temperature can affect the feeding oil temperature, and hence, the feeding oil viscosity. Moreover, the ambient temperature affects the external heat exchange, which in turn affects the temperature both of the oil and of the metallic parts. In particular, geometry variations, as for example clearance variations, can be obtained by means of thermal deformations. Ambient temperature in the majority of the cases is not under control of the operator and results to be one of the uncertainties affecting the study of the problem.

- Evolving gas temperature: De Jongh and Van Der Hoeven [18] has revealed an interesting effect related to the temperature of the gas adopted for the process. For their specific machine, with a cartridge consisting of relatively large steel part around the impeller-end bearing (see Figure 1.11), they found a high sensitivity of the cooling effect produced by the process gas, evolving at $5°C$, on the steel. The result was a decrease in the bearing clearance and a decrease

of the stability margin. Temperature of the evolving gas is only dependent on the gas process and hence usually not under control of the operator and can range from high-values, as in the first high-pressure stages of gas turbines, to very low values, as for machines used in cryogenic applications.

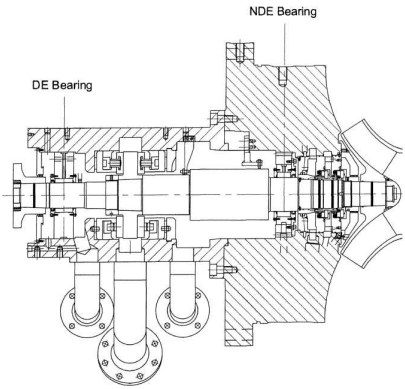

Figure 1.11: Longitudinal section of compressor cartridge from the work of De Jongh and Van Der Hoeven [18].

1.5 Affected machines

Many different typologies of turbomachinery result to be affected by the rotor thermal instability. As widely reported in literature, machines affected by such a phenomenon are usually fast rotating machines, highly loaded, with heavy overhung masses both in terms of impellers and couplings.

In the work of De Jongh [3] a resume of the case studies found in literature is shown. The cases have been grouped on the base of the rotor geometry. The classification proposed by De Jongh is here reported in order to list the typical geometrical configurations affected by the phenomenon.

- single overhung wheel (Berot and Dourlens [20], Kocur and de Jongh [21], De Jongh and Van Der Hoeven [18], Kirk et al. [22])
- double overhung wheels (Faulkner et al. [23], Schmied et al. [17])
- 1 overhung coupling (Kocur and de Jongh [21])
- 2 overhung couplings (De Jongh and Morton [1])
- integrally geared, 1 overhung wheel (Carrick [24])
- integrally geared, 2 overhung wheels (Marscher and McGinley [25])

Moreover, a list of some of the referenced machines affected by the synchronous thermal instability is reported below. The objective is to show the potential of the Morton effect to occur across-the-board of the turbomachinery world.

- air compressors (as presented in the work of Phuttipongsit [12]);
- gas boost compressors (as presented in the work of De Jongh [3]);
- pipeline direct inlet centrifugal compressor (as presented in the work of Berot and Dourlens [20]);
- gas turbines (as results from the work of De Jongh [3] which reports about Morton studies [8]);
- radial inflow turbines (as results from the work of Kocur and de Jongh [21] which reports about the work of Faulkner et al. [23]);
- turbine generators (as presented in the work of Schmied [6]);
- turbo-expanders for cryogenic industry (as presented in the work of Schmied et al. [17]);
- large turbochargers with overhung turbine wheel (as reported in the work of Saha [26] about the case study in the work of Faulkner et al. [23]).

Chapter 2

Synchronous thermal instability: prediction strategies

Contents

One of the main outcome of Chapter 1 is that the Morton effect optimal prediction strategy has yet to be identified. This chapter aim to present and discuss the prediction strategies proposed in literature in order to entail a selection of the optimal solution for the purpose of this work.

2.1 Literature survey

After the pioneering works of Morton [7] and Hesseborn [9], which are not available in open literature, many researchers have proposed different approaches to the problem.

The first step is the evaluation of the strategy to approach the three physical terms A, B and C, which resulted to characterize the phenomenon. This can be done by means of the following approaches:

- experimental evaluations;
- numerical calculations;
- analytical studies.

Once the driving terms are physically represented, the global system analysis, that is to assess the stability of the system, can be obtained by means of the following strategies:

- simulating with time accuracy the evolution of the complete system;
- iterating between the quasi-steady solutions of each of the above physical aspects assuming a segregation of effects;
- using some stability theory criteria or empirical evaluation of stability based on the assessment of A, B and C term mutual importance;

Some works with a full analytical approach have been published over the years, from the works of Keogh and Morton [27] [28] of the early 1990s, to the work of Gu and Chu [29], dated 2013, where the effects of thermal excitations on a rotor shaft are studied. In the first work of Keogh and Morton [27] the mechanism of the differential heating is evaluated by means of a theoretical treatment based on short bearing theory and iso-viscous lubricant. In their second work, the feedback mechanism is analysed in order to assess stability of the system, yet again considering strong simplifications. These evaluation strategies, although important in order to increase the awareness of the physics of the problem, result to

be lacking of practical sense due to the necessary simplifications adopted, which results to be far from the realistic industrial applications.

Schmied [6] proposed in his work a beam finite element model for A and C terms evaluation. An equivalent of the B correlation is adopted on the base of an empirical equation proposed in the work of Kellenberger [30] and coupled with the finite element method. The system stability could be assessed studying the overall finite element method evolution in time or on the base of the evaluation of the so called thermal eigenvalues related to the finite element system solution matrix.

De Jongh and Morton [1] were the first to laboratory reproduce and openly publish a thermal instability field issue occurred on an offshore centrifugal compressor. They directly measured the rotor thermal gradient and explained the thermal instability assessing from theory the A and C terms while the B term was evaluated through laboratory measurements. To assess stability, they successfully applied a control theory criterion evaluating the gain of the coupled system in loop.

Larsson [31] characterized the B and C terms using an analytical formulation derived from the numerical work of Ericsson (Ericsson 1980). He obtained an analytical correlation between bow and shaft vibration. The A term was evaluated using a beam finite element rotor model. Finally, everything was coupled in order to compute the overall system solving matrix eigenvalues and assess stability.

Balbahadur and Kirk [32] approach was to characterize B by simply averaging the temperature results of a steady state bearing solver at different imposed orbital positions. The C term was determined using a simple analytical relation depending on thermal gradient and equivalent shaft overhung dimensions. The main advantage of this approach is to quickly solve the thermal gradient but its accuracy is debated due to a quasi-unsteady approach, which aim to represent the real unsteady behaviour of the system. A criteria for thermal instability was given by means of comparison between estimated thermal unbalance and rotor weight.

Murphy and Lorenz [16], following the strategy used by De Jongh

and Morton [1] and the method of Balbahadur and Kirk [32], proposed a simplified method based on linear stability theory to predict rotor thermal instability. For the evaluation of the A term a standard rotordynamic code was used. To evaluate B and C, the same approach of Kirk and Balbahadur was used taking advantage of a standard bearing code. A, B and C can be then expressed as complex coefficients and the criterion for thermal stability is simply depending on the real part of the composition of A, B and C which should not exceed a threshold value.

Gomiciaga and Keogh [13] instead used CFD techniques to numerically predict rotor thermal gradients on plain bearings depending on imposed forward and backward circular rotor orbits. The Navier-Stokes fluid and energy equations were solved in a 3D cylindrical reference frame. Similarly, Lee and Palazzolo [33] solved the transient thin film thermohydrodynamic (THD) equations together with the transient shaft heat conduction. The bearing and shaft thermal solution was then coupled with a finite element rotordynamic code in order to simulate with time accuracy the evolution of the complete system. This approach resulted to be computationally very demanding.

A possible computationally less demanding but still accurate approach was proposed by Childs and Saha [34]. The method needs to pre-compute the rotor thermal gradient amplitude and phase for a given set of forward and backward circular orbits with different amplitude at different rotational speed. Starting from a first response to unbalance, the code computes, for a generic elliptical orbit, the rotor thermal gradient interpolating from the pre-computed thermal table. Based on the rotor thermal gradient, the shaft thermal bowing and the induced thermal unbalance is computed and the calculations are iterated. Stability is assured when the computed orbit converges to a bounded value. According to their work the approach results to be less demanding due to the preceding orbit calculations needed for the thermal table production. About six to eight hours are needed for the evaluation of a thermal gradient of a specific orbit at a certain shaft running speed.

Grigorev et al. [15] computed the B term solving the perturbed (os-

cillating) thin film Reynolds equations. A similar method was used by Ericsson [35] who first derived the set of equation for the oscillating temperature, film thickness and pressure. The oscillating temperature is then used to compute the shaft bowing and the equations are coupled into a beam finite element transient rotordynamic code. Stability can be monitored looking at the time evolution of the computation or through the evaluation of the numerical stability of the solution by means of the computation of the spectral radius of the time solver numerical matrix.

As stated in Chapter 1, for all the mentioned models, the most challenging term to be evaluated is the B term. The numerical estimation of the link between rotor vibration at bearing section and rotor thermal gradient requires in fact very demanding and time consuming simulations, whose accuracy remains still questionable due to the lack of accurate rotor thermal gradient measurements, with the only exception of the De Jongh and Morton [1]. This highlights the need for dedicated experimental campaigns to be carried out by the industry in order to validate or develop prediction models which suit their own product needs. In the present work, results of the developed predictive models are compared, where available, with experimental measurements coming from a dedicated experimental test campaigns carried-out by GE Oil & Gas facility in Florence.

2.2 Physical time scales of the problem

When introduced in Chapter 1, the Morton effect has been presented as an highly interdisciplinary phenomenon, composed of various different physical processes, characterized by very different length and time scales. In order to improve the knowledge of the problem and allow an aware selection of the approach to be used for its prediction and analysis, it is necessary to perform a study of the orders of magnitude of the involved time scales. In particular, these latter are necessary when choosing between time accurate solutions or simplified approaches. Before this analysis is presented, some considerations on length scales are given.

Length scales, which in turn play a role in the calculation of time scales, have a major role when approaching the specific tasks of the physics in order to simplify the involved equations and select the dimensional strategy (one, two or three-dimensional calculations). This kind of analysis is performed in a dedicated section, where details of the numerical codes are given.

About the analysis of the physical time scales, the first step is to evaluate some reference values to be used as a comparison. The analysed phenomenon is driven by synchronous vibrations and hence, time scales of the rotation are selected for the purpose. Three different rotational speed are selected in order to span some typical working range: 3000 rpm, 8000 rpm, 13000 rpm.

Table 2.1 reports the rotational speed, frequencies and reference time scales for the three selected cases. As it is possible to observe, the reference time scales (τ_{ref}) of the phenomena related to the synchronous precession motion are of the order of $10^{-2} \div 10^{-3}$ s.

Rotational speed [rpm]	Frequency [Hz]	Reference time scale [s]
3000	50	0.020
8000	133.3	0.0075
13000	216.7	0.0046

Table 2.1: Reference values of rotational speed, frequency and time scales.

In order to introduce the time scales related to the thermal problem, let's imagine a step change of one of the variables affecting the rotordynamic behaviour. Once the perturbation is applied, the system finds a new working condition characterized by a new equilibrium point and orbit. About the oil flow, the thermo-hydrodynamic behaviour is suddenly modified and the variation is transmitted through the whole system transported by convection, diffusion and conduction mechanisms. When these perturbations reach the solid surfaces, which constitute the boundaries of the fluid system, an interaction is performed by means of what we will refer to as convective heat transfer terms. Finally, the perturbation is diffused inside of the solid parts by means of conduction, which drives the

thermal deformation of the system and hence, affects the rotordynamics and in turn the fluid-dynamics again. Elastic phenomena are not considered since their time scale are lower than the thermal ones and since thermal phenomena are the main topic of the work.

In order not to weigh down the text, the complete analysis of the thermal time scales of the problem is reported in Appendix A, where the analysis of the orders of magnitude of the equations is also extensively presented. The proposed results have been obtained following the Lord Kelvin approach. This consists in selecting physical quantities representative of the phenomenon in order to give dimensionless terms of the equations of an unitary order. If reference quantities are well selected, the analysis enables a comparison among the terms in order to weigh their importance. As a consequence, equations can be simplified, neglecting lower order of magnitude terms, or a comparison among the terms can be performed in order to evaluate, for example, the characteristic time scales.

Results obtained from the introduced analysis are summarized in Table 2.2.

time scale type	symbol	value [s]	normalized value τ/τ_{ref} [-]
reference	τ_{ref}	$10^{-3} - 10^{-2}$	1
fluid convection	τ_{fcv}	$10^{-3} - 10^{-2}$	1
fluid conduction	τ_{fcd}	10^{-1}	$10^{-2} - 10^{-1}$
fluid dissipation	τ_{fd}	10^{-3}	$10^{-1} - 10^{0}$
convective heat transfer	τ_{cht}	$\geq 10^{2}$	$\geq 10^{4}$
solid conduction	τ_{sc}	$10^{2} - 10^{3}$	$10^{4} - 10^{6}$
thermal deformation	τ_{td}	$10^{2} - 10^{3}$	$10^{4} - 10^{6}$

Table 2.2: Comparison among the thermal time scales of the problem.

The main outcome, as expected, is that thermal inertia of the metallic parts is responsible for very long conductive time scales and hence, results to be the bottleneck of the physical process. The formulations of the conductive time scales of the shaft and pads/bush are reported in the

following Equations 2.1 and 2.2:

$$\tau_{sc-shaft} = \frac{\rho_s c_s R_j^2}{k_s} \tag{2.1}$$

$$\tau_{sc-pads/bush} = \frac{\rho_s c_s (\Delta R)^2}{k_s} \tag{2.2}$$

where ρ_s is the density, c_s and k_s are respectively the specific heat capacity and the thermal conductivity of the material composing shaft, pads and bush. R_j is the journal radius and ΔR is the thickness of the pad or of the bush.

Four to six orders of magnitude are highlighted when considering conductive terms with respect to the reference time scales of the system. Furthermore, it has to be noted that, if time accurate simulations need to be performed, the physical time step necessary to solve higher frequency phenomena should be selected as a fraction of the reference time scale.

2.3 Evaluation of the strategies for prediction and analysis

As shown in Section 2.1, various approaches have been considered by researchers to evaluate the A, B and C terms characteristic of the Morton effect and to assess the system stability. The objective of the present work is to develop numerical predictive models for the thermo-hydrodynamic problem in order to enable the evaluation of the B term and hence, by means of integration in more complex analysis, the evaluation of the Morton effect onset.

2.3.1 B term evaluation

Among the predicting strategies for the B term found in literature, and presented in Section 2.1, the experimental approach has been rejected a priori since the purpose of the work is to develop analytical/numerical predictive models.

The most simple approach resulted to be the analytical one, which is

based on strong simplification hypothesis. As a consequence, the obtained models result to be fast and interesting from the point of view of the physical comprehension of the phenomenon but usually impractical. In fact, the adopted simplifications (e.g., cylindrical bearings, iso-viscous approach, infinitely long or short bearings and so on) result to be far from the realistic problem and hence not attractive for modelling industrial cases.

Among the possible numerical approaches, the complete transient models have been rejected due to impractical reasons. This time, the impracticability is a consequence of the time scale previously analysed. In fact, very demanding calculations have to be protracted in time before the effects of the thermal diffusion exhibit. From a preliminary evaluation of the proposed time scales, an order of magnitude of various thousands orbits have to be simulated before the onset of appreciable thermal effects.

The consequence is that only simplified approaches, among the numericals, result of interest. Two main possibilities are in literature: quasi-unsteady approach and perturbation models. Between the two, the quasi-unsteady approach has been selected as a first choice for the purpose of the work. The choice is derived from an increasing complexity attitude. Therefore, the quasi-unsteady approach has been considered in order to test its potential in the forecast of the Morton effect onset, before eventually adopt a more complex, but in any case simplified, model. Furthermore, the quasi-unsteady approach enable the use of a steady state code, which was scheduled to be developed, since, for the numerical analysis of the Morton effect, rotordynamic codes rely on numerically evaluated dynamic coefficients. Finally, the choice is supported by the promising results obtained in literature following the same approach.

2.3.2 System stability

Once the thermo-hydrodynamic problem is solved and a strategy for the estimation of the B term individuated, the global system stability has to be assessed. Three main strategies have been highlighted in Section

2.1: simulating with time accuracy the evolution of the complete system, iterating between the quasi-steady solutions of each of the physical aspects or using some stability theory criteria.

Yet again, time accurate simulation of the complete system are rejected due to the evaluated time scales and therefore iterative approaches and stability analysis result to be the available choices. Both the approaches have been considered for the purpose of the present work.

2.3.3 Adopted strategy for the Morton effect prediction

In conclusion a numerical code for the thermo-hydrodynamic analysis is developed and validated in order to calculate the static and dynamic bearing characteristics (called TILTPAD, is presented in Chapter 3). Furthermore, a numerical code for the calculation of the B term is developed and validated on the base of the selected quasi-unsteady approach (called SNAPSHOT, is presented in Chapter 4). These models have been then used in order to assess the Morton effect stability both via a stability theory analysis and by means of an iterative procedure.

The global system representative of the Morton loop, adopted for the iterative approach, has been developed in collaboration with the MDMlab of the Department of Industrial Engineering of the University of Florence, which developed the rotordynamic models.

Results are compared with the available experimental data obtained from a dedicated test campaign carried out at the GE oil & Gas facility in Florence, which is detailed in the work of Panara et al. (2015).

Part I

Numerical codes

Chapter 3

Plain and tilting pad journal bearings performance

Contents

Various types of bearings are adopted in industry on the base of the technical and economical characteristics both of the field of application and of the bearing itself. In particular, among the hydrodynamic bearings, Tilting Pad Journal Bearings (TPJB) are widely used in the turbomachinery field due to their stability performance, which largely overtakes the fixed geometry ones. Hence, modern machines, such as turbines, compressors and pumps, benefits from their application and these components result to be widely adopted and consequently result of particular interest for the topic of the present work. Anyway, for sake of generality, also fixed geometry bearings are considered in the present work.

Although PJBs and TPJBs are quite simple components, the physics behind their operating conditions could reach an unexpected complexity. For example, during a real operation the fluid is subject to viscosity variations, there could be strong effects of thermal and elastic deformations, and the film could be subject to oil cavitation. Moreover, modern machines could drive these components towards transitional or fully turbulent oil flow conditions. Therefore, if accurate results are needed, all of these features should be considered when approaching the numerical modelling of the hydrodynamic lubrication problem.

3.1 Friction, Wear and Lubrication - Tribology

In the above introduction a direct reference to the hydrodynamic lubrication in bearings has been given. This is a specific condition of lubrication and hence, in order to propose a more general point of view, it is necessary to introduce first the general lubrication problem and its possible forms and then give evidence, for the cases of the present work, to be in the range of hydrodynamic lubrication. It is therefore unavoidable to introduce the word "tribology", which unifies the classical subjects of science and technology concerning friction, wear, and lubrication.

From the advent of machine-based civilization such a topic results of great interest since many pairs of machine parts are in relative motion (e.g., gear teeth, systems with cams and rolling element bearings). In such cases friction always exists and as a result not only energy losses and wear are obtained but also seizure may take place. These phenomena are prevented, or at least mitigated, by supplying a suitable substance such as oil, which take place between the two sliding surfaces, lubricating the conjunction.

3.1.1 Lubrication regimes

Fluid film lubrication occurs when opposing surfaces are separated by a film of lubricant. Actually various different regimes of lubrication exist on the base of the characteristics of the sliding surfaces (e.g., conformal

or nonconformal, roughness, physical properties of the materials), on the base of the lubricant adopted and on the base of the operating conditions.

A useful tool for understanding the role of different regimes of lubrication is the classical Stribeck's curve, dated 1902, and presented in Figure 3.1. The ordinate represents the friction coefficient and the abscissa rep-

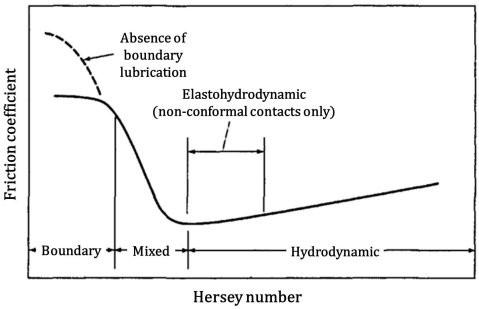

Figure 3.1: Stribeck curve: friction coefficient with respect to the Hersey number

resents the Hersey number. This latter is an operating parameter which increases increasing rotational speed or viscosity of the oil and decreases increasing the load to be carried by the bearing. As a consequence high values of Hersey number imply thick lubricant films and low values results in very thin films.

Varying the operating conditions four main lubrications regimes are obtained: the hydrodynamic lubrication, the elastohydrodynamic lubrication, the mixed lubrication and the boundary lubrication.

The first one, obtained for high Hersey number values, is characterized by thick layers of lubricant so that the opposing solid surfaces are prevented to come into contact. The lubrication in this case is driven by the bulk flow characteristics of the oil and the pressure is usually not enough large to cause elastic deformations ($p \leq 5\ MPa$).

The second one is a form of lubrication characterized by elastic deformation of the lubricated surfaces due to the pressure developed. There are two kind of elastohydrodynamic lubrications (hard and soft) and both

of them are usually strongly related to nonconformal surfaces. According to the work of Hamrock et al. [36], in fact, the conformal surfaces usually goes directly from hydrodynamic to mixed lubrication.

If the loads to be carried are too high or the rotational speed too low the lubricant film will be penetrated and the third condition is obtained. In fact, in the mixed lubrication some contact between the asperities due to the surface roughness take place and the lubrication results to be governed by a mix of boundary and fluid film effects.

The last condition is the case at very low Hersey number. This case, called boundary lubrication, is characterized by considerable asperity contacts and negligible lubrication effects. Hence, the frictional characteristics are determined by the properties of both solids and lubricant at the common interfaces.

3.1.2 Film parameters for different lubrication regimes

According to the work of Hamrock et al. [36] a film parameter (Λ) can be defined in order to differentiate the lubrication regimes presented in the previous section. Proposed in Equation 3.1 the parameter is a function of the minimum film thickness and of the root mean square surface finish of the sliding surfaces (R_q).

$$\Lambda = \frac{h_{min}}{(R_{q,shaft}^2 + R_{q,pad/bush}^2)^{0.5}} \tag{3.1}$$

A rough estimate of the range of the parameter characterizing the various regimes is presented in the previously cited work [36] where Figure 3.2 has also been taken from. According to such a rough estimation, values of the film parameter of about $5 < \Lambda < 100$ are referred to the hydrodynamic lubrication regime.

From an analysis of the parameters of the journal bearings adopted for the experimental test campaign dedicated to the Morton effect, presented in Chapter 6, values of the film parameter (Λ) between 30 and 70 are obtained. As a consequence, looking at Figure 3.2, hydrodynamic lubrication with complete separation of the solid sliding surfaces is ex-

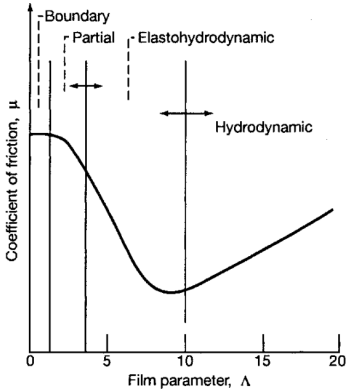

Figure 3.2: Variation of the friction coefficient with the film parameter (from the work of Hamrock et al. [36])

pected confirming the need to model this latter state of lubrication at least preliminary.

3.1.3 Lubrication regimes of the rotor thermal instability

Since the present thesis is devoted to the thermal phenomena affecting the turbomachinery rotordynamic behaviour, some considerations are here suggested about the lubrication regimes in case of rotor thermal instability.

When the Newkirk problem is considered, the displacement amplitudes are sufficiently high in order for the shaft to reach contact with some statoric components. Hence, different kind of lubrication regimes may be encountered along the shaft orbital motion.

The Morton effect has instead a different physical genesis and usually there is no need to model different lubrication regimes, at least up to the very end of the process.Moreover, it has to be underlined that the Morton effect mainly affects high rotational speed machines which are characterized by reduced eccentricities and hence by higher values of the film parameter Λ. The consequence is that the hydrodynamic lubrication models are usually suitable for the modeling of the Morton effect.

Although roughness effects will not be considered in the present work, due to the expected fully hydrodynamic regime, here a brief outline on the approaches found in literature about the topic is proposed.

While the theoretical bases required to obtain an in-depth analysis of the mixed lubrication regime has been established a long time ago, only small scale numerical modeling is available due to computing limitations. In fact, due to the grid refinement requested, roughness-scale simulations results only attractive for very small lubricated contacts. As a consequence averaging models have gained popularity due to their ability to generalize the trends observed in very small cases and to transfer these effects to large scale numerical simulations.

The first deterministic simulations of very small bearings in mixed lubrication regime have been considered in the works of Patir and Cheng [37], [38].In their work, the results obtained by means of the deterministic approach have been adopted to obtain an average flow model, able to generalize the roughness-effects on a large scale numerical simulation. This stochastic approach, based on some flow factors to be included in the Reynolds equation, results the mainly adopted strategy to numerically solve mixed lubrication related to commonly sized bearings. The same approach has been in fact adopted by various researchers. For example, in the works of Wang et al. [39] and Shi and Wang [40] the authors adopted the previously cited flow factors for the mixed thermo-elastohydrodynamic analysis of plain journal bearings. All of these works and all of the more recent ones, as for example the work of Liu et al. [41], based on the same approach make the assumption that the results obtained with the deterministic simulation on very small (below 1 mm^2 in area) parallel bearings can be transposed to "large scale problems".

Although the stochastic approach results to be the only way to approach the analysis of "large scale" journal bearings, effort is also made on deterministic flow models. One of these works is the one of Dobrica et al. [42], where mixed elastohydrodynamic lubrication of a partial journal bearing (3 cm of diameter) is presented.

3.2 General description of the numerical code

TILTPAD is an in-house numerical code, developed at the Department of Industrial Engineering of the University of Florence, for the thermo-hydrodynamic analysis of both plain and tilting pad journal bearings performance (lemon bore bearings could also be analysed, although results of these latter will not be shown).

The starting point of the present work has been the numerical code for the isoviscous analysis of plain bearings presented in the work of Martelli and Manfrida [43]. The original code has been firstly modified and updated in order to overcome some of its drawbacks, in particular the limit imposed to the refinement of the numerical grid, then, the routines for the pressure field evaluation have been adopted in order to develop the tilting pad bearing code. Once the isoviscous version of the TPJBs solver has been obtained, thermal effects, the effects of superlaminar regimes and the calculation of the dynamic coefficients have been implemented. Finally, the obtained code, presented in the following of the present chapter, has been modified in order to allow also the thermo-hydrodynamic analysis of plain bearings. Such a choice has been dictated by the opportunity to simply obtain a plain bearing solver with the same features of the tilting pad one.

Since, as previously stated, TPJBs are widely diffused for industrial applications, TILTPAD is detailed in the present work referring mainly to this kind of bearings. However, different strategies to be adopted for different journal bearings will be explicitly highlighted.

The main hypothesis behind the code are summarized below and represent the classical assumptions to approach the hydrodynamic lubrication problem:

- $h/B \simeq C_b/B << 1$
- $h/R_j \simeq C_b/R_j << 1$
- The continuum description is valid ($Kn << 1$)
- Incompressible fluid

- Newtonian fluid
- Laminar flow
- Negligible volume forces
- Constant specific heat capacity of the oil
- Constant thermal conductivity of the oil

where B and R_j are respectively the axial extension of the bearing and the radius of the journal, h and C_b are the film-thickness and the radial bearing clearance and Kn is the Knudsen number.

The obtained code is steady-state, is based on a 2D thin-film approach and is able to find either the resulting hydrodynamic load using the shaft equilibrium position and the rotational speed (i.e., direct problem) or the shaft equilibrium position once the load to be carried and the rotational speed are prescribed (i.e., inverse problem). More in detail, the code handles only direct problem data types and hence a dedicated search procedure for the evaluation of the equilibrium's eccentricity and attitude angle is followed in case of inverse problems. The procedure uses the method of chords when dealing with eccentricity and a bisection method for the attitude angles. The choice of using two different procedures allowed obtaining faster solutions and a higher convergence rate.

3.3 Film-thickness calculation

Once values of eccentricity and attitude angle are provided, together with the geometrical features of the analyzed bearing, it is possible to calculate the film-thickness distribution along axial and tangential directions (in the present code only the tangential film thickness variations are considered since neither misaligned bearings configurations nor thermal and elastic deformations are considered). Moreover, when dealing with tilting pad bearings, preload (m_{TLP}) and pads' tilt angles (θ_{i-th}) have also to be provided. These latter are evaluated by means of a dedicated procedure described in a dedicated section (Section 3.5). The

final formulation, shown in Equation 3.2 for the $i-th$ pad, is composed of three terms: the first one is the same in both plain and tilting pad bearings while the second and the third account for the variation of the film-thickness respectively due to pads' tilt angle and preload.

$$\begin{aligned} h(\delta,z)|_{i-th} =& h(\delta)|_{i-th} = C_b(1-\epsilon\cos(\delta-\gamma))+ \\ & -2R\sin(\alpha')\theta_{i-th} + C_b m_{TLP}(1-\sin(\alpha'')) \end{aligned} \tag{3.2}$$

In Figure 3.3 a sketch of a tilting pad bearing with its local and global reference systems is reported.

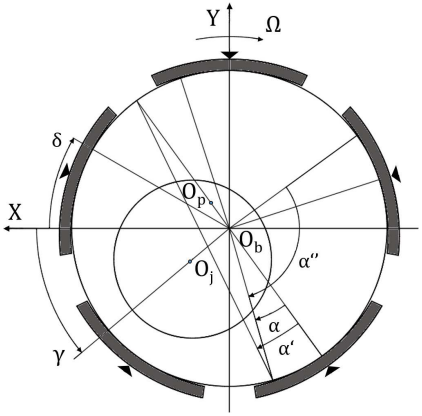

Figure 3.3: Sketch of a tilting pad bearing and its local angular reference systems.

The pad preload adopted in the code (m_{TLP}) is differently defined from the classical definition found in literature (m). Both the formulations are reported in Equations 3.3 and 3.4, where C_b and C_p are respectively the assembled bearing clearance and the pad machined clearance.

$$m = \frac{C_p - C_b}{C_p} \tag{3.3}$$

$$m_{TLP} = \frac{C_p - C_b}{C_b} = m \cdot \frac{C_p}{C_b} \tag{3.4}$$

Finally, pads are set in prescribed positions (i.e., tilt angle $\theta_{i-th} = 0$) in order to approach cylindrical bearings, while lemon bore bearings are obtained by means of the preload effect on the fixed configuration.

3.4 Pressure field calculation: Reynolds' equation

The pressure field of the hydrodynamic problem applied to plain or tilting pad bearings is calculated by means of a numerical solution of the Reynolds' equation. A review of the widely known physics of the problem is presented, together with details of the numerical approach.

3.4.1 Orders of magnitude of the equations

In order to obtain the representative equations for the lubrication problem the first step is the dimensional analysis of the incompressible Navier-Stokes equations, whose details are reported in Appendix A.

The main consequence of the geometrical condition related to the length scales of the problem ($C_b/R_j \simeq 10^{-3} << 1$) is the opportunity to neglect curvature effects and hence, adopt Cartesian coordinates. The general reference system adopted for the dimensional analysis is shown in Figure 3.4.

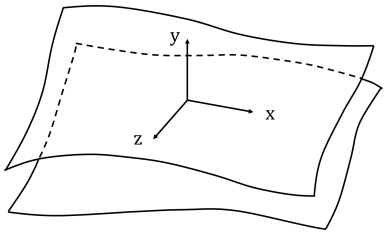

Figure 3.4: General reference system adopted for the lubrication problem.

Introducing the non-dimensional variables, defined in Appendix A, in the continuity and momentum equations enable to write their non-dimensionalised form. Once obtained, lower order viscous terms of the

momentum equations, which result to be multiplied by a factor $(C_b/R_j)^n$ (with $n = 3, 4$), are simplified and Equations 3.5, 3.6, 3.7, 3.8 are obtained.

$$\frac{UC_b}{VR_j}\left(\frac{\partial u^*}{\partial x^*} + \frac{\partial w^*}{\partial z^*}\right) + \frac{\partial v^*}{\partial y^*} = 0 \tag{3.5}$$

$$Re_s\frac{\partial u^*}{\partial t^*} + Re^*\left[\left(u^*\frac{\partial u^*}{\partial x^*} + v^*\frac{\partial u^*}{\partial y^*} + w^*\frac{\partial u^*}{\partial z^*}\right)\right] = -\frac{\partial p^*}{\partial x^*} + \frac{\partial\left(\mu^*\frac{\partial u^*}{\partial y^*}\right)}{\partial y^*} + \\ + \frac{Re^*}{Fr}f_x^* \tag{3.6}$$

$$Re_s\left(\frac{C_b}{R_j}\right)^2\frac{\partial v^*}{\partial t^*} + Re^*\left(\frac{C_b}{R_j}\right)^2\left(u^*\frac{\partial v^*}{\partial x^*} + v^*\frac{\partial v^*}{\partial y^*} + w^*\frac{\partial v^*}{\partial z^*}\right) = -\frac{\partial p^*}{\partial y^*} + \\ + \frac{Re^*}{Fr}\frac{C_b}{R_j}f_y^* \tag{3.7}$$

$$Re_s\frac{\partial w^*}{\partial t^*} + Re^*\left[\left(u^*\frac{\partial w^*}{\partial x^*} + v^*\frac{\partial w^*}{\partial y^*} + w^*\frac{\partial w^*}{\partial z^*}\right)\right] = -\frac{\partial p^*}{\partial z^*} + \frac{\partial\left(\mu^*\frac{\partial w^*}{\partial y^*}\right)}{\partial y} + \\ + \frac{Re^*}{Fr}f_z^* \tag{3.8}$$

The nondimensional groups introduced in the proposed equations are defined as given in Equations 3.9, 3.10, 3.11, 3.12.

$$Re = \frac{\rho U C_b}{\mu_{oil}} \tag{3.9}$$

$$Re^* = Re\left(\frac{C_b}{R_j}\right) \tag{3.10}$$

$$Re_s = \frac{\rho\Omega C_b^2}{\mu_{oil}} \tag{3.11}$$

$$Fr = \frac{U^2}{gR_j} \tag{3.12}$$

Further simplifications are enabled considering Table 3.1, which reports some of the main nondimensional groups evaluated for various test cases found in literature. Due to the choice of the reference time scale $\tau = 1/\Omega$, the modified Reynolds number Re^* and the squeeze Reynolds number

Re_s result identical, and hence only the first one is reported.

Reference work	C_b/R_j	Re	Re^*	Ta	Fr
Ferron et al. [44]	0.0029	93	0.27	5.02	895.2
Fitzgerald and Neal [45]	0.001	59	0.059	1.87	2728
Lund and Tonnesen [46]	0.00134	81	0.11	2.97	1398
Daniel and Cavalca [47]	0.00152	606	0.92	23.7	6874
Fillon et al. [48]	0.00158	51	0.08	2.04	894.6
Knight [49]	0.00158	60	0.095	2.39	2721
Monmousseau et al. [50]	0.00158	51	0.08	2	895.2
Taniguchi et al. [51]	0.00256	1429	3.65	72.3	2412

Table 3.1: Main nondimensional groups of the momentum equations for some typical test cases found in literature.

As previously stated, from the analysis of the proposed groups, further simplifications can be obtained. In particular, inertial terms of the momentum equations result to be negligible ($Re^* << 1$) for the majority of the cases, except for the test cases proposed in the works of Daniel and Cavalca [47] and Taniguchi et al. [51], where centrifugal and parallel terms of instability are of importance, as noticed from the Taylor and Reynolds numbers (see Section 3.8 for more details). Furthermore, volumetric force terms are simplified due respectively to the low value of the modified Reynolds number Re^* and to the high value of the Froude number Fr.

Hence, since the terms with lower order of magnitude of the momentum equations can be disregarded, at least within the usual geometrical and operating conditions, the study of the incompressible lubrication problem can be accomplished by means of the following formulation, where Equation 3.13 is the continuity equation and Equations 3.14, 3.15 and 3.16 are the simplified momentum equations.

$$\frac{\partial u}{\partial x} + \frac{\partial v}{\partial y} + \frac{\partial w}{\partial z} = 0 \tag{3.13}$$

$$\frac{\partial p}{\partial x} = \frac{\partial(\mu \frac{\partial u}{\partial y})}{\partial y} \tag{3.14}$$

$$\frac{\partial p}{\partial y} = 0 \tag{3.15}$$

$$\frac{\partial p}{\partial z} = \frac{\partial(\mu \frac{\partial w}{\partial y})}{\partial y} \tag{3.16}$$

One of the main outcome of such analysis, together with the simplification of the momentum equations is that pressure variation across the fluid film result also to be negligible ($p(x, y, z, t) \simeq p(x, z, t)$), thus enabling a two-dimensional thin-film approach.

3.4.2 Reynolds' equation

Velocity component in the axial and tangential direction can be directly evaluated by means of integration of the momentum equations (Equations 3.14, 3.16), which gives, with suitable boundary conditions, the following velocity formulations:

$$u(x, y, z) = \frac{y}{2\mu}(y - h)\frac{\partial p}{\partial x} + U\frac{y}{h} \tag{3.17}$$

$$w(x, y, z) = \frac{y}{2\mu}(y - h)\frac{\partial p}{\partial z} \tag{3.18}$$

Then, the continuity equation is integrated across the fluid film with the substitution of the obtained velocity components. The final result is the well-known Reynolds' equation, shown in Equation 3.19, which is widely reported in literature, as for example in the work of Szeri [52], Hamrock et al. [36] and Frene et al. [53].

$$\frac{\partial}{\partial x}(\frac{h^3}{12\mu}\frac{\partial p}{\partial x}) + \frac{\partial}{\partial z}(\frac{h^3}{12\mu}\frac{\partial p}{\partial z}) = \frac{U}{2}\frac{\partial h}{\partial x} + \frac{\partial h}{\partial t} \tag{3.19}$$

The present code uses a local reference system fixed with the bush/pads and with the cross-film coordinate that increases moving from the bush/-pads towards the shaft.

In terms of Boundary conditions (BC), the code can handle both pressure (Γ_{press}) or oil flow rates (Γ_{flow}). Usually, feeding oil pressure is applied to the inlet (Γ_{in}) and outlet (Γ_{out}) of the pads, while ambient

pressure is applied at the external pad's border-lines (Γ_{amb}), as shown in Figure 3.5. Relative pressure is specified in the code and hence zero is usually adopted for the external borders.

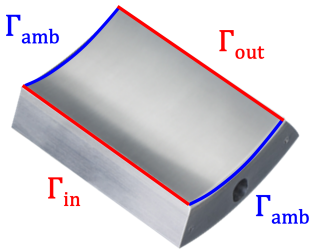

Figure 3.5: Boundary conditions for the numerical solution of the Reynolds equation.

3.4.3 Cavitating region

Swift-Stieber conditions, also known as Reynolds conditions, are adopted in order to easily consider the effects of cavitation on the pressure field and to allow for reliable simulations (more physically consistent than the Sommerfeld's and Gumbel's conditions). Under such hypothesis, the pressure field at the inception of the cavitated region is set as p_{cav} and the tangential gradient is smoothly brought at zero $\frac{dp}{d\delta} = 0$. Usually, since the cavity pressure differs little from the ambient pressure, the relative pressure in the cavitated region is set as zero. The proposed conditions are widely used in literature and constitute the preliminary approach to the problem (see the works of Frene et al. [53] and Szeri [52]).

This is of particular importance when the code is adopted for the thermo-hydrodynamic analysis of plain journal bearings.

3.4.4 Numerical approach

Usually, finite difference or Finite Element Methods (FEM) are considered for the solution of the incompressible lubrication problem, which

consists in finding the solution of the Reynolds' equation with the prescribed boundary conditions. In the present work, the formulation proposed by Reddi [54] is implemented. In his work, a variational principle for the incompressible lubrication problem is presented and is proved to be a minimum principle. Hence, the solution of the Reynolds' equation is obtained finding the two-dimensional pressure distribution that minimizes the functional shown in Equation 3.20.

$$\Phi\{p\} = \int\int_D -[-\frac{h^3}{12\mu}\nabla p \cdot \nabla p + hU\frac{\partial p}{\partial x} + hW\frac{\partial p}{\partial z} - 2p\frac{\partial h}{\partial t}]dA + \int_{\Gamma_{flow}} qpds \tag{3.20}$$

Here, p represents the pressure field, h the film thickness distribution, D is the domain of the surface integration, s is the domain of the Γ_{flow} border integration, U is the tangential shaft speed, W is the axial shaft speed (if relative axial motion between shaft and bearing exists) and μ is the dynamic viscosity.

By means of FEM discretization, using linear shape functions on the triangular elements of the grid, the problem is reduced to a linear system of equations with nodal pressure values as unknowns, shown in Equation 3.21.

$$KP = \frac{1}{2}(V - H - Q) \tag{3.21}$$

Here, K is the volumetric fluidity matrix, defined in Equation 3.22, V is the element flow vector, defined in Equation 3.23, H is the squeeze film vector, defined in Equation 3.24, Q is the boundary flow vector, defined in Equation 3.25 and P is the vector of the nodal pressure unknowns.

$$K = \sum_{m=1}^{N} \int\int_{D^m} R_m^T C_m R_m dA_m \tag{3.22}$$

$$V = \sum_{m=1}^{N} \int\int_{D^m} h_m U_m R_m dA_m \tag{3.23}$$

$$H = \sum_{m=1}^{N} \int\int_{D^m} 2\dot{h}_m T_m dA_m \tag{3.24}$$

$$Q = \sum_{m=1}^{N} \int_{\Gamma_{flow}^{m}} qT_m ds_m \tag{3.25}$$

About the definitions given in the previous equations, the integrals are evaluated on the triangular element E_m, N is the number of all the triangular elements composing the numerical grid, R_m is the pressure gradient matrix for the element E_m, C_m is the property matrix for the element E_m, U_m is the vector of surface velocity in tangential and axial direction for the E_m element, h_m is the film thickness for element E_m, T_m is the matrix relating the continuous pressure distribution on E_m to the nodal pressure values (related to the interpolation functions), $\dot{h}_m$ is the squeeze velocity of the element E_m and q is the linear normal flow at boundaries. Matrices and vectors are evaluated by means of numerical integration following the table reproduced in the work of Reddi [54] and taken from the work of Felippa [55]. For more details see also the work of Martelli and Manfrida [43], where isoviscous solution of plain bearings is presented.

The numerical grid, which defines the nodal points for the pressure and temperature calculation, is automatically generated by the code once the geometry and the desired discretization parameters are provided. These latter are: the number of elements along the tangential direction (NX) and the number of elements along the axial direction (NZ).

A generic grid is shown in Figure 3.6. The code firstly generates a structured grid with rectangular elements following the imposed discretization parameters. Once generated, each rectangular element is subdivided in four triangular ones, where the pressure field is evaluated. The formulation to calculate the total number of rectangular and triangular elements is shown in Figure 3.6.

The linear system of Equation 3.21, generically written as $Ax = b$, is solved by means of the iterative Gauss-Seidel method, see Equation 3.26, where i and k are referred to the elements constituting the vector x, j is referred to the iteration number of the method and n is the total number

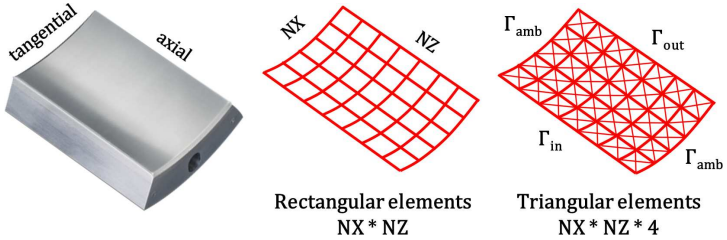

Figure 3.6: Example of grid generation: pad geometry, example of grid composed of rectangular elements and corresponding grid composed of triangular elements.

of nodes of the grid.

$$x_i^{(j)} = \frac{1}{a_{ii}}(b_i - \sum_{k=1}^{i-1} a_{ik}x_k^{(j)} + \sum_{k=i+1}^{n} a_{ik}x_k^{(j-1)}) \tag{3.26}$$

A relaxation factor (α_{ORC}) is adopted in order to obtain a faster convergence. In Equation 3.27, where the relaxation factor is shown, the term $x_i^{\star(j)}$ is the one effectively calculated.

$$x_i^{(j)} = x_i^{(j-1)} + \alpha_{ORC}(x_i^{\star(j)} - x_i^{(j-1)}) \tag{3.27}$$

Once the pressure field is obtained an integration is performed over the domain in order to calculate the resulting load in terms of module and angle.

3.5 Pads equilibrium positions

The pads' equilibrium problem allows for the evaluation of the tilt angles (θ_{i-th}) representative of the equilibrium configuration (i.e. when the torque C $[Nm]$ generated by the pressure field acting on the pad and evaluated with respect to its pivot axis is zero and the resulting load is not null). Such a problem can be numerically posed as finding the first zero of the torque, as a function of the tilt angle. A mixed procedure is used for the purpose starting from a converging film condition. Figure 3.7 shows

a typical trend of the moment as a function of the tilt angle, with positive values of moment obtained for converging pad-shaft configurations.

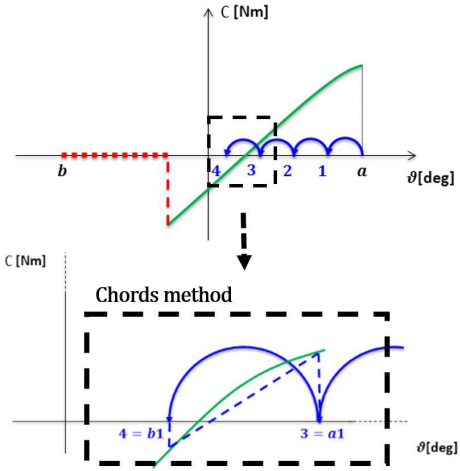

Figure 3.7: Representation of the mixed procedure for the evaluation of pads' equilibrium position.

In the first part of the procedure shown on the upper part of Figure 3.7, the code scans with prescribed tilt angle steps the whole available range in order to define an appropriate interval characterized by torque values at the extremes having opposite sign. Once the interval has been defined, the code uses the method of chords to solve the root finding problem, shown at the bottom of Figure 3.7.

When a zero is found during the preliminary scanning, the code tests, with a half of the previous scanning step, the tilt angle range starting from the last point which resulted in a value different from zero (see 3.8). This procedure allows to evaluate if the obtained zero is the expected solution or one of the configurations with zero load carrying capacity (red dashed line in the figure).

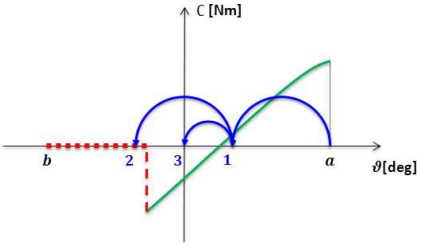

Figure 3.8: Procedure in case zero is found during the scanning of the tilting angle steps.

3.6 Energy Equations

Temperature calculation is of primary importance in order to account for dynamic viscosity variations. The problem has been soon considered and great effort has been dedicated over the years in order to overcome the isoviscous approach. One of the first proposed formulations is the adiabatic solution proposed in the work of Cope [56] in 1949. Since then, many works have followed and several approaches have been proposed: 1D formulations, as implemented in the first two equations of the present code, quasi-2D and quasi-3D formulations, as respectively described in the work of Lund and Hansen [57] and in the work of Stefani and Rebora [58], up to fully 3D approaches, as in the work of Taniguchi et al. [51], which also accounts for turbulent flow regimes.

The present section describe the three simplified steady-state energy equations implemented in the present code. The first two equations are one-dimensional equations based on the Petroff hypothesis, while the third is a quasi-two-dimensional equation inspired by the work of Knight [49].

3.6.1 Analysis of the orders of magnitude

Introducing in the energy equation the non-dimensional variables, defined in Appendix A, and by means of manipulation and simplification of the lower order terms, multiplied by a factor $(C_b/R_j)^n$ (with $n = 2, 3, 4$),

the non-dimensional form of the energy equation for the steady state incompressible lubrication problem (with constant specific heat capacity and conductivity) is obtained (Equation 3.28).

$$Pe(u^* \frac{\partial \tilde{T}^*}{\partial x^*} + v^* \frac{\partial \tilde{T}^*}{\partial y^*} + w^* \frac{\partial \tilde{T}^*}{\partial z^*}) = \frac{\partial^2 \tilde{T}^*}{\partial y^{*2}} + Br[\mu^* (\frac{\partial u^*}{\partial y^*})^2 + \mu^* (\frac{\partial w^*}{\partial y^*})^2] \tag{3.28}$$

Non-dimensional terms related to the energy equation are defined in Equations 3.29, 3.30, 3.31 and 3.32.

$$Pr = \frac{c\mu_{oil}}{k} \tag{3.29}$$

$$Pe = \frac{\rho c}{k} \frac{U C_b^2}{R_j} = PrRe^* \tag{3.30}$$

$$Ec = \frac{U^2}{c\Theta} \tag{3.31}$$

$$Br = \frac{\mu_{oil} U^2}{k\Theta} = PrEc \tag{3.32}$$

The Peclet number (Pe) is the ratio of advective transport rate and diffusive transport rate, while the Brinkman number (Br) is the ratio of viscous dissipation rate to thermal conduction.

Considering the non-dimensional values, shown in Table 3.2, referred to some works found in literature, some considerations cane be done. The

Reference work	Pr	Pe	Br	Ec
Ferron et al. [44]	430	116.5	9.45	0.022
Fitzgerald and Neal [45]	252	14.9	5.33	0.021
Lund and Tonnesen [46]	244	26.5	3.8	0.015
Daniel and Cavalca [47]	539	498	155	0.287
Fillon et al. [48]	426	34.6	3.73	0.009
Knight [49]	396	37.6	9.12	0.023
Monmousseau et al. [50]	426	34.6	6.23	0.015
Taniguchi et al. [51]	426	1557	48.3	0.113

Table 3.2: Main non-dimensional groups of the energy equation for some typical test cases found in literature.

variation of both non-dimensional numbers of Equation 3.28 is substantial: the Pe number varies from 14.9 of Fitzgerald and Neal [45] to 1557 of Taniguchi et al. [51] (for lower rotational speed not reported in the table, a value of 3.7 is found for the Fitzgerald and Neal [45] case), while the Br number varies from 3.8 of the Lund and Tonnesen [46] case up to 155 of the work of Daniel and Cavalca [47] (again, for lower rotational speed a unitary value of Br is obtained for the Fitzgerald and Neal [45] case). This highlights the opportunity for some cases to adopt the adiabatic solution, which has been practically used as a first approximation to solve the problem (as for example in the work of Cope [56]). More in general, the complete three dimensional steady state energy equation to be adopted is shown in Equation 3.33.

$$\rho c(u\frac{\partial T}{\partial x} + v\frac{\partial T}{\partial y} + w\frac{\partial T}{\partial z}) = k\frac{\partial^2 T}{\partial y^2} + [\mu(\frac{\partial u}{\partial y})^2 + \mu(\frac{\partial w}{\partial y})^2] \tag{3.33}$$

3.6.2 Petroff-type simplification

The Petroff-type simplification is based on the hypothesis that the shaft is perfectly concentric with the bearing. As a consequence, considering for simplicity a plain bearing, no pressure rise is possible and the bearing is unable to support any load. This hypothesis gains in reliability when applied to lightly loaded bearings, to fast running rotors or when high dynamic viscosity of the oil is considered (that is in all the configurations where a small eccentricity is obtained). Although quite restrictive, the hypothesis has proved to give reasonable accuracy [19].

Considering the velocity field for a fluid flowing within a plain bearing, the general solutions of the tangential and axial velocity distributions along the radial (y) direction are shown in Equations 3.34 and 3.35.

$$u(x,y) = \frac{1}{2\mu(x,z)}\frac{dp(x,z)}{dx}(y^2 - yh(x)) + U\frac{y}{h(x)} \tag{3.34}$$

$$w(y,z) = \frac{1}{2\mu(x,z)}\frac{dp(x,z)}{dz}(y^2 - yh(x)) + W\frac{y}{h(x)} \tag{3.35}$$

As it is possible to observe, a general velocity field is composed of two

terms: a Poiseuille term, driven by the pressure gradient and a Couette term, driven by the moving wall. Since usually there is no axial translation (W) between housing and shaft, the axial velocity of the oil inside the bearing is driven only by the Poiseuille term. See Figure 3.9 for the typical parabolic and linear velocity profiles representative of Poiseuille and Couette terms.

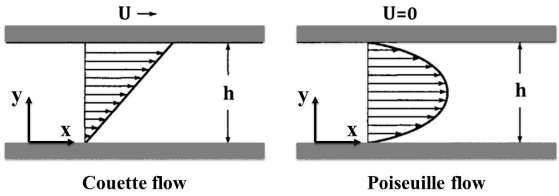

Figure 3.9: Velocity profiles along the radial direction fro a Poiseuille and a Couette flow.

The main consequence of the Petroff-type hypothesis is to simplify the velocity field. In fact, if no pressure rise is developed within the bearing, the Poiseuille terms of the tangential and axial velocity profiles vanish. Under such hypothesis, the axial velocity vanishes completely while the tangential velocity is composed only of its Couette term. A simplified shear stress, which drives the dissipation function, and a simplified volumetric oil circulation inside of the bearing are consequently found. The obtained formulations are shown in Equations 3.36,3.37.

$$\tau_{yx} = \mu(x)\frac{du(x,y)}{dy} = \mu(x)\frac{U}{h(x)} = \mu(x)\frac{\Omega R_j}{h(x)} \tag{3.36}$$

$$q(x) = B \cdot \int_0^{h(x)} u(x,y)dy = B \cdot \frac{Uh(x)}{2} = B \cdot \frac{\Omega R_j h(x)}{2} \tag{3.37}$$

3.6.3 1D energy equation

The first energy equation implemented in the code has been suggested by Balbahadur and Kirk [32] and is obtained by means of a steady-state energy balance executed on a control volume extended across the whole

film-thickness, including a thin layer of the metal of the bush/pad and of the shaft (shown in Figure 3.10). Since axial temperature variations are neglected, see Appendix A for more detailed considerations about axial simplifications, a one-dimensional mean temperature equation is provided.

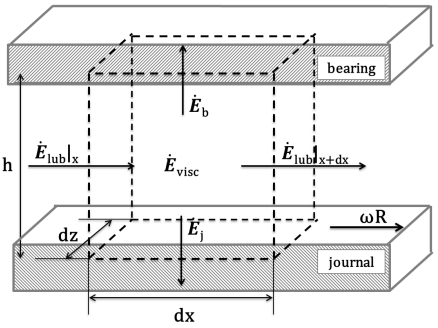

Figure 3.10: Scheme for the journal bearing energy balance.

The thermal balance under steady state condition means there is no accumulation rate of energy, hence, the energy dissipated inside of the control volume ($\dot{E}_{visc}$) is convected or conducted away by the convective ($\dot{E}_{lub}$) and conductive ($\dot{E}_j$,$\dot{E}_b$) terms. The complete thermal balance is presented in Equation 3.38.

$$\dot{E}_{visc} = \dot{E}_{lub}\big|_{x+dx} - \dot{E}_{lub}\big|_{x} + \dot{E}_j + \dot{E}_b \tag{3.38}$$

By means of substitution of the appropriate terms in the Equation 3.38, considering the Petroff-type simplification, Equation 3.39 is obtained. In the proposed formulation f represents the fraction of thermal power transferred to the journal and $(1-f)$ represents the remaining fraction of thermal power lost to the bearing housing and surroundings.

$$\begin{aligned}\Omega R_j \tau_{yx} dx =& \rho_{oil}\frac{\Omega R_j}{2} h c_{oil}(T + \frac{dT}{dx}dx) - \rho_{oil}\frac{\Omega R_j}{2} h c_{oil} T + \\ &+ f H dx (T - T_{amb}) + (1-f) H dx (T - T_{amb})\end{aligned} \tag{3.39}$$

The bearing heat transfer coefficient H is determined by the Equation 3.40, which is derived from a regression analysis of experimental data provided by Ettles [59].

$$H = 25.5 U_j^{0.7} \mu(T_0)_{oil}^{-0.2} (R_j \Delta\delta_{pad}) \tag{3.40}$$

Finally, considering the Petroff-type hypothesis for the shear stress evaluation, considering the geometrical relations characteristic of the problem (i.e., small clearance C_b respect to R_j) which enable to consider $R_j\delta \approx x$, simplifying the equal terms on both sides and rearranging gives the following one-dimensional energy equation, where $\tilde{T} = (T - T_0)$ is defined with respect to the feeding oil temperature T_0.

$$\frac{d\tilde{T}}{d\delta} + \frac{2H}{\rho_{oil} c_{oil} \Omega h(\delta)} \tilde{T} - \frac{2\mu_{ave}\Omega R_j^2}{\rho_{oil} c_{oil} h^2} \tag{3.41}$$

Effective viscosity evaluation

The dynamic viscosity (μ_{ave}) adopted in Equation 3.41 is an average (or effective) viscosity adopted to simplify the formulation. It is based on the temperature variation obtained across a geometrically equivalent plain journal bearing (ΔT_{ave}) with the same operating conditions of the analysed case.

For the evaluation of the effective viscosity value the Reynolds formulation, shown in Equation 3.42, is adopted.

$$\mu_{ave} = \mu(T_0) e^{-\beta \Delta T_{ave}} \tag{3.42}$$

The proposed formulation is widely considered for the thermo-hydrodynamic analysis of journal bearings. Among the various works some are cited as an example: the work of Knight [49], the work of Monmousseau et al. [60] and the work of Balbahadur [19]. Despite this, it has to be underlined that the proposed formulation is not extremely accurate, as reported in the work of Balbahadur [19] and also in the work of Williams [61].

Pads' inlet temperature evaluation

In order to evaluate the pads' inlet temperature, which constitutes the inlet boundary condition of the energy equation, the temperature raise (ΔT_{ave}) obtained on the equivalent plain journal bearing has also been adopted.

In particular, inlet temperature is considered to be the sum of lubricant supply temperature and the estimated temperature raise, this latter multiplied by a scaling ratio that is function of the minimum inlet film thickness h_{min-in} and of the inlet film-thickness h_{in} of the analysed pad (or sector if referred to a plain bearing calculation), as shown in Equation 3.43.

$$T_{in} = T_0 + \frac{h_{min-in}}{h_{in}} \cdot \Delta T_{ave} \tag{3.43}$$

Numerical solution

The numerical solution of the energy equation has been obtained by means of the finite difference method, obtaining Equation 3.44.

$$T_{i+1} = T_i + \Delta\delta \left[\frac{2\mu_{ave}\Omega R_j^2}{\rho_{oil} c_{oil} h(\delta)^2} \bigg|_i - \frac{2H(T - T_{amb})}{\rho_{oil} c_{oil} \Omega h(\delta)} \bigg|_i \right] \tag{3.44}$$

The grid adopted for the purpose is shown further, in Figure 3.13.

3.6.4 Improved 1D energy equation

The second equation represents an evolution of the already described one in the way that it is able to overcome some of its drawbacks. In particular, it has been decided to make the equation independent from the use of the effective temperature raise evaluated on an equivalent plain bearing. As a consequence, a local dynamic viscosity is considered in the energy equation instead of referring to an effective one, and an improved mixing model is adopted in order to calculate the inlet temperature at each pad of the bearing.

The obtained equation is formally similar to the previous one but an iterative cycle is now introduced since the dynamic viscosity, which is a

function of the temperature of the oil, has a role in the calculation of the temperature field (the obtained energy equation is shown in Equation 3.45).

$$\frac{d\tilde{T}}{d\delta} + \frac{2H}{\rho_{oil} c_{oil} \Omega h(\delta)} \tilde{T} - \frac{2\mu(\tilde{T}) \Omega R_j^2}{\rho_{oil} c_{oil} h^2} \tag{3.45}$$

At the beginning of the calculation the temperature field is evaluated considering a constant value of the dynamic viscosity correspondent to the feeding oil temperature μ_0 once the local temperature is evaluated by means of Equation 3.45, the local dynamic viscosity can be re-calculated closing the loop (shown in Figure 3.11). The process is iterated until convergence of the temperature field.

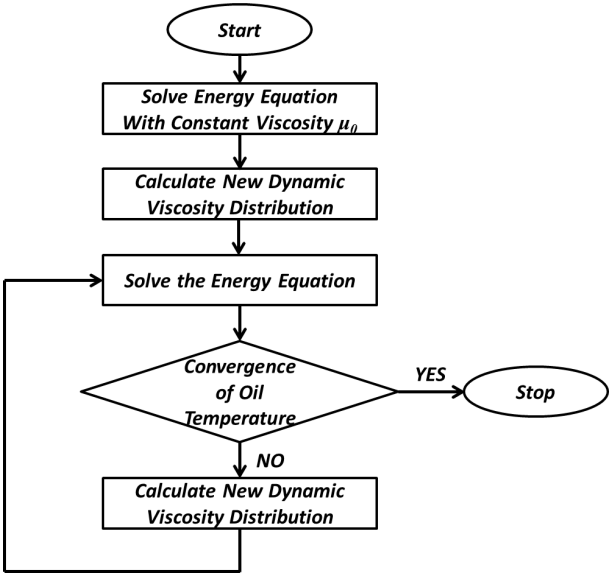

Figure 3.11: Flow chart of the iterative procedure for temperature calculation.

Local dynamic viscosity evaluation

The local dynamic viscosity ($\mu(T)$), here presented with respect to the absolute temperature T instead of the differential temperature $\tilde{T}$ adopted in Equation 3.45, is evaluated by means of the Reynolds formulation, shown in Equation 3.46.

$$\mu(T) = \mu(T_0)e^{-\beta(T-T_0)} \tag{3.46}$$

Mixing model to calculate the pads' inlet temperature

An improved mixing model, with respect to the original formulation proposed by Balbahadur [19], has been adopted for the novel energy equation.

The proposed mixing model is based on an energy and continuity balance for a control volume chosen between two consecutive pads as shown in Figure 3.12.

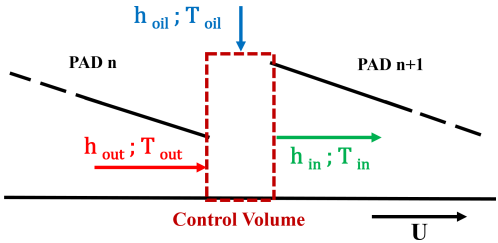

Figure 3.12: Flow chart of the iterative procedure for temperature calculation.

The Petroff's simplification, adopted for the energy equation, is also adopted for the mixing. By means of the continuity equation (see Equation 3.47) it is possible to calculate the feeding oil mass-flow. This latter is then used in the enthalpy balance (see Equation 3.48) in order to find the inlet temperature of the pad, shown in Equation 3.49. Where pedices are considered in accordance with Figure 3.12.

$$\rho_{oil}\frac{\Omega R_j}{2}h_{in}B = \rho_{oil}\frac{\Omega R_j}{2}h_{out}B + \dot{m}_{oil} \tag{3.47}$$

$$\rho_{oil}\frac{\Omega R_j}{2}h_{in}Bc_{oil}T_{in} = \rho_{oil}\frac{\Omega R_j}{2}h_{out}Bc_{oil}T_{out} + \dot{m}_{oil}c_{oil}T_{oil} \tag{3.48}$$

$$T_{in} = \frac{h_{out}}{h_{in}}T_{out} + \frac{h_{in} - h_{out}}{h_{in}}T_{oil} \tag{3.49}$$

Since pads' inlet temperatures are function of the outlet temperatures of the upwind pads, an iterative procedure raises. According to the procedure shown in Figure 3.11, each time the energy equation is solved the code recalculates the inlet temperatures.

Furthermore, if the configuration drives the model towards an increase in oil temperature across the feeding groove, the inlet temperature is limited to the outlet value of the upwind pad.

In case the code is used as a plain bearing solver (considering a constantly zero tilt angle for the pads), the mixing model is slightly modified. The loaded sector maintains the standard model using the sector's minimum film-thickness instead of the trailing edge one, while downstream of unloaded sectors a fixed percentage value of hot-oil carry over is considered at the inlet section. The adopted percentage value has been selected by means of model assessment in comparison with experimental data and has shown good results when adopted both for different test-cases and operating conditions. More details are proposed in Appendix B.

Numerical solution

The numerical solution of the proposed equation (Equation 3.45) has been approached by means of the finite difference method, obtaining the Equation 3.50. A first forward difference has been selected for the purpose.

$$T_{i+1} = T_i + \Delta\delta\left[\left.\frac{2\mu(T)\Omega R_j^2}{\rho_{oil}c_{oil}h(\delta)^2}\right|_i - \left.\frac{2H(T-T_{amb})}{\rho_{oil}c_{oil}\Omega h(\delta)}\right|_i\right] \tag{3.50}$$

A numerical one-dimensional grid is considered along the mid section of the pads (see Figure 3.13). Each pad, has the same number of grid elements along the tangential direction NX which was selected for the two-dimensional grid of the pressure calculation.

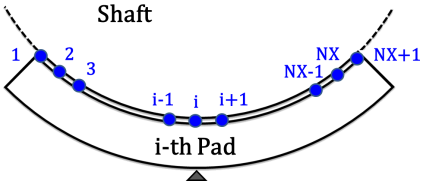

Figure 3.13: One dimensional numerical grid for the energy equation.

Frictional power losses

By means of the Petroff's simplification, the frictional power losses can be easily evaluated for each single pad, see Equation 3.51, once the film-thickness distribution $h(\delta)$, the oil viscosity μ_{oil}, the running speed Ω and the geometrical characteristics R_j and B are known.

$$P_{f-i} = \int_{A_i} \Omega R_j \tau dA = \int_{\delta_{in-i}}^{\delta_{out-i}} \Omega R_j \mu(T(\delta)) \frac{\Omega R_j}{h(\delta)} B R_j d\delta_i \tag{3.51}$$

The total frictional power loss is calculated adding the single pad terms (Equation 3.52):

$$P_{f-tot} = \sum_{i=1}^{NP} P_{f-i} \tag{3.52}$$

3.7 Conjugate Heat Transfer (CHT) approach

The last implemented energy equation is inserted in a wider context, hence, an introduction to the general problem is given before details are presented. In particular, a conjugate heat transfer approach has been considered, together with an improved energy equation. Once the procedure is implemented, the energy equation can be changed if an increase in accuracy is desired.

The adoption of the present equation is beyond the scope of the work. However, the model is presented since it represents an upgrade of the thermo-hydrodynamic code. Moreover, the opportunity to simulate the heat exchange during the precession motion would be more suited for the

aim of analysing the phenomenon and could be used to give an accurate initial condition for a perturbation approach, with consistent temperatures for both oil and solid parts.

Among the various approaches proposed in literature, two main branches are identified on the base of the way temperature and heat flux continuity are imposed at the solid-fluid interfaces, respectively referred to as conjugate and coupled methods. When the first approach is considered, the numerical domain includes the whole fluid and solid regions, hence, equations are solved simultaneously and the continuity of temperature and heat flux is implicitly imposed. For this kind of approach problems arise due to the need to simultaneously manage different physics with different physical characteristics (e.g., length and time scales). On the contrary, coupled methods individually solve fluid and solid regions, entailing the use of dedicated codes, but an iterative procedure raises in order to guarantee the thermal continuity at the interfaces, which is obtained by means of mutual exchange of thermal results, respectively imposed as boundary conditions. Some typical problems of the coupled methods are: the need of interpolation procedures if grids are not identical at the interfaces and the arise of instabilities which are usually controlled by means of relaxation coefficients.

The second approach is selected for the present work, due to the simplicity of managing a coupling procedure. In fact, as previously stated, these kind of approaches do not need to modify the existing codes but need to manage an iterative exchange of information.

3.7.1 Coupled procedure

Four main kind of coupling approaches exist in literature (see the work of Verstraete [62]), defined on the base of the information exchanged having as a reference the fluid:

1. TFFB: Temperature Forward Flux Back
2. FFTB: Flux Forward Temperature Back
3. hFTB: Heat transfer coefficient Forward Temperature Back

4. hFFB: Heat transfer coefficient Forward Flux Back

In the first, Neumann condition is adopted by the fluid solver while Dirichlet condition is set for the solid solver. In the second, inverted conditions are applied respectively to fluid and solid solvers with respect to the first introduced method. The last two methods adopt the convective heat transfer equation, shown in Equation 3.53, to give a mixed boundary condition to the solid solver while temperature and heat flux are imposed to the fluid solver respectively in the third and fourth case. The choice of H, which can be imposed with a value (H_{app}) different from the real one, do not affect the final result but strongly affects the stability of the system and the convergence rate.

$$\dot{q}_{wall} = H(T_{wall} - T_{oil}) \tag{3.53}$$

Among the various approaches, the FFTB method is selected since it has been fruitfully adopted in the work of Knight [49]. The resulting conjugate heat transfer procedure is iterated until the temperature of the pads, of the shaft and of the fluid film have reached convergence.

3.7.2 Quasi-2D energy equation

Following the results of the dimensional analysis proposed in Section 3.6.1, and further detailed in Appendix A, a two-dimensional approach has been considered. Temperature variations are expected in the tangential and radial directions, while axial ones are neglected.

The energy equation presented is a quasi-2D one, derived from the work of Knight [49], resulting from a further simplification of the complete two-dimensional energy equation shown in Equation 3.33. Such a simplification is due to the opportunity to efficiently solve the problem, but primarily, to the fact that the accuracy gained considering a more accurate equation is affected by strong uncertainties in terms of boundary conditions. In fact, while it is possible to roughly estimate the average temperature value at the inlet of the pad, the accuracy of a radial profile imposed at the inlet section is questionable if the model do not solve the

complex fluid flow between the pads.

Since a quasi-2D approach has been selected, a bulk flow temperature is considered for the purpose and its variation along the tangential direction is evaluated as a function of the viscous dissipation and of the conductive terms evaluated at the solid walls (shaft and bush/pads). Moreover, according to the work of Knight and Barrelt [63] the solution of the temperature field is obtained at the center plane of the bearing, neglecting also the contribution of the axial pressure gradient on the viscous term.

The adopted bulk flow temperature is defined as shown in Equation 3.54, where the temperature profile across the film is supposed to be of the second order ($T(x,y) = a(x)y^2 + b(x)y + c(x)$).

$$T_m(x) = \frac{\int_0^h T(x,y)dy}{h(x)} \tag{3.54}$$

The temperature gradients at the wall are derived from the definition of the cross-film temperature distribution, with the local coefficients evaluated imposing the average value $T_m(x)$ and the wall values at $y(x) = h(x)$ and $y(x) = 0$, which are respectively the bush/pads temperature $T_b(x)$ and the journal temperature $T_j(x)$. This latter is considered as constant and is evaluated as the average of the bulk temperature along the whole tangential extension of the bearing. The obtained gradients are shown in Equations 3.55 and 3.56.

$$\left.\frac{\partial T}{\partial y}\right|_h = \frac{4T_j + 2T_b - 6T_m}{h} \tag{3.55}$$

$$\left.\frac{\partial T}{\partial y}\right|_0 = \frac{6T_m - 4T_b - 2T_j}{h} \tag{3.56}$$

The quasi-2D energy equation, based on the bulk flow temperature previously defined, is shown in Equation 3.57.

$$\rho c(\frac{Uh}{2} - \frac{h^3}{12\mu}\frac{\partial p}{\partial x})\frac{dT_m}{dx} = 6\frac{k}{h}(T_j + T_b - 2T_m) + \frac{\mu U^2}{h} + \frac{h^3}{12\mu}(\frac{\partial p}{\partial x})^2 \tag{3.57}$$

Local dynamic viscosity evaluation

The local dynamic viscosity, dependent to the bulk-flow temperature T_m, is evaluated by means of the Reynolds formulation, shown in Equation 3.58.

$$\mu(T_m) = \mu(T_0)e^{-\beta(T_m - T_0)} \tag{3.58}$$

Mixing model to calculate the pads' inlet temperature

The proposed mixing model is based on an energy and continuity balance for a control volume chosen between two consecutive pads as shown in Figure 3.12.

Since the Petroff's type simplification is not adopted for the quasi-2D energy equation the mixing model previously presented in Section 3.6.4 has been further improved in order to include the effects of the pressure field in the calculation of the oil mass-flow rates: at the inlet section of the pads ($\dot{m}_{in}$) and laterally ($\dot{m}_{lat}$), where the oil leaves the pad due to the axial pressure gradient. The flow at the trailing edge ($\dot{m}_{out}$) of the pad is then calculated as shown in Equation 3.59.

$$\dot{m}_{out} = \dot{m}_{in} - \dot{m}_{lat} \tag{3.59}$$

Once the mass-flow at the trailing edge of the pad is found, a thermal balance is executed on the control volume previously defined in Section 3.6.4. Again, since pads' inlet temperatures are function of the outlet temperatures of the upwind pads, an iterative procedure raises.

Numerical solution

Equation 3.57 is solved by means of the finite difference method, adopting first forward difference for the first-order derivatives. The obtained formulation is shown in Equation 3.60, where the subscripts are

referred to Figure 3.13 and where $\delta = x/R_j$.

$$\frac{T_{m,i+1} - T_{m,i}}{\Delta\delta} = \frac{6\frac{k}{h_i}(T_j + T_{b,i} - 2T_{m,i}) + \frac{\mu_i \Omega^2 R_j^2}{h_i} + \frac{h_i^3}{12\mu_i R_j^2}(\frac{\partial p}{\partial \delta}|_i)^2}{\rho c(\frac{\Omega h_i}{2} - \frac{h_i^3}{12\mu_i R_j^2}\frac{\partial p}{\partial \delta}|_i)} \tag{3.60}$$

Iterations are performed until convergence of temperature is obtained, as previously shown for the improved one-dimensional energy equation.

3.7.3 Conduction equation

The conduction equation adopted for the purpose of the conjugate heat transfer analysis is applied only to the pads/bush of the bearing, since the shaft, due to the thermal time scales, can be considered at a constant temperature value. A steady state equation, expressed in polar coordinates, is adopted. Further simplification is obtained neglecting the axial variation of the temperature inside of the pads, as also done for the temperature of the oil within the film. The final formulation obtained is shown in Equation 3.61.

$$\frac{\partial^2 T}{\partial r^2} + \frac{1}{r}\frac{\partial T}{\partial r} + \frac{1}{r^2}\frac{\partial^2 T}{\partial \delta^2} = 0 \tag{3.61}$$

About the boundary conditions, each side of the pads are separately considered. In particular, since a FFTB approach is used, the temperature gradient inside of the pads, evaluated at the interface with the oil, is calculated by means of the requirement of heat flux continuity between the fluid and the metal, shown in Equation 3.62.

$$\frac{\partial T}{\partial r} = \frac{k_{oil}}{k_s}\frac{\partial T}{\partial y}\Big|_0 \tag{3.62}$$

At the leading and trailing edges of the pads, the heat convection boundary conditions are imposed (see Equation 3.63). The convection coefficient adopted is derived from the work of Knight [49]. Two more approaches are available: the one proposed in the work of Ettles [59] and the opportunity to tune the model by means of selection of the two pa-

rameters.

$$HTC(T - T_0) = \frac{k_s}{r}\frac{\partial T}{\partial \delta} \tag{3.63}$$

At the bottom surface of the pads an adiabatic condition is selected, as also considered in the work of Knight [49]. However, in order to have a well posed problem at least a temperature value has to be given to the solid domain. The feeding oil temperature is adopted for the purpose and it is imposed at both the corners of the bottom of the pads.

Numerical solution

The numerical grid adopted to solve the heat conduction equation inside of the pads is a structured one that has the same number of elements along the tangential direction adopted for the energy equation (NX), while in the radial direction, is composed of NR equally spaced elements. The finite difference method is considered in order to solve the conduction problem and in particular, central differences are used for the first and second order derivatives. The final formulation is shown in Equation 3.64, where indices i and j are respectively considered for the variations along the radial and tangential directions and where R_{pad} is the radius of the inner surface of the pad.

$$\begin{aligned}&\frac{T_{i-1,j} - 2T_{i,j} + T_{i+1,j}}{\Delta r^2} + \frac{1}{R_{pad} + (i-1)\Delta r}\frac{T_{i+1,j} - T_{i-1,j}}{2\Delta r} + \\ &+ \frac{1}{(R_{pad} + (i-1)\Delta r)^2}\frac{T_{i,j-1} - 2T_{i,j} + T_{i,j+1}}{\Delta \delta^2} = 0\end{aligned} \tag{3.64}$$

The initialization temperature of both shaft and pads is obtained by means of the effective temperature raise ΔT_{ave} presented in Section 3.6.3.

The Gauss-Seidel point by point method is adopted in order to solve the numerical problem. By means of this approach, the values of the temperature are evaluated by iteratively visiting each grid point following a prescribed order.

3.8 Superlaminar flow regimes

The classical theory of lubrication considers the inertia terms to be negligible in comparison with viscous and pressure ones, as highlighted in Appendix A. The parameter to be considered in order to evaluate the mutual weight between these terms, in the hydrodynamic bearings field, is the modified Reynolds number (see Equation 3.65).

$$Re^* = Re\frac{C_b}{R_j} = \frac{\rho\Omega R_j C_b}{\mu}\frac{C_b}{R_j} \tag{3.65}$$

When the modified Reynolds number approaches the order of one, the inertia forces are of the same order of magnitude of the viscous ones. The flow becomes then characterized by: irregularity, three-dimensionality, anisotropy, increased diffusivity and dissipation. The topic has been widely studied both in general and with focus on the hydrodynamic journal bearing field. An interesting excursus on flow stability, transition and turbulence applied to journal bearings, complete of flow modelling details, are given in the works of Szeri [52] and Frene et al. [53].

Modern machines, characterized by the need for increased rotational speed are more and more frequently subjected to work in the superlaminar/turbulent flow regime. Since the relative eccentricity value $\frac{C_b}{R_j}$ in bearings applications varies usually between a small range, the critical Reynolds number can be generally overtaken due to fast rotation, high density or low dynamic viscosity, which in turn is related to the high rotational speed by means of its temperature dependence.

Turbulence originates as a form of instability of the laminar flow for high Reynolds number values. Two different kind of instabilities arise in journal bearings during the transition from laminar to turbulent flow:

- Centrifugal instability: occurs in flows with curved streamlines, when centrifugal forces dominates the stabilizing viscous ones. The characteristic parameter is the Taylor number.

- Parallel flow instability: characterized by propagating waves (Tollmien-Schlichting waves), this is the classical kind of instabilities of bound-

ary layers and pipe flows where inertial and viscous forces compete. The parameter is the well known, previously introduced, Reynolds number.

As reported in the work of Szeri [52] for thin film bearings, the accepted critical Reynolds number for the parallel flow instability to drive the system directly to the fully turbulent regime is 2000. Furthermore, Frene et al. [53] reports about the results of the characteristic zones of a smooth loaded bearing presented in the work of Pan and Vohr [64], in analogy with turbulence occurrence in duct flows, a first critical Reynolds is identified at 1000 representing the first transition from the laminar behaviour.

About the centrifugal instability, the critical threshold is more complicated to be found due to the effects of the inner cylinder eccentricity and to the consequently induced pressure field. Above the critical value, yet to be presented, a first transition occurs driving the system to the onset of steady secondary vortices, known as Taylor vortices. These represent the first and most simple form of instability within an unexpectedly complex range of opportunities (see the works of Taylor [65] and Grossmann et al. [66] for an extensive overview). Two exemplifying flow features, respectively Taylor vortices and wavy vortex flow are represented in Figure 3.14 from the work of Lueptow [67].

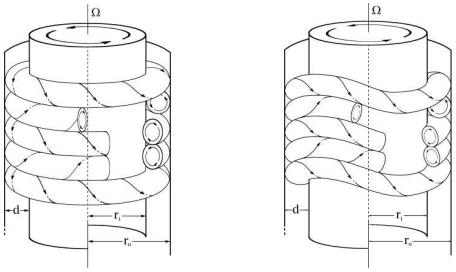

(a) Taylor vortex flow. **(b)** Wavy vortex flow.

Figure 3.14: Two out of several very distinctive flow features of a Taylor-Couette system, from the work of Lueptow [67].

In case coaxial cylinders are considered, the accepted value for the critical Taylor number is 41.2. The definition of the Taylor number relative to this threshold is given in Equation 3.66. When the proposed value of the critical Taylor number is doubled, the fully turbulent regime is obtained (both for eccentric and concentric cylinders).

$$Ta = Re\sqrt{\frac{C_b}{R_j}} \tag{3.66}$$

An interesting overview of the fluid instability in between eccentrically rotating cylinders is also reported in the work of Deng [68] and in the work of Frene et al. [53]. In these works, the results of the investigations of Di Prima [69] and Ritchie [70] on the crtical Taylor number for eccentric cylinders are reported. Moreover, in the work of Frene et al. [53], results of an experimental campaign carried out by Frene and Godet [71] on journal bearings are also given. For the bearing case, experimental data resulted to be bounded between the two cited instability theories of Di Prima and Ritchie. On the base of the cited experimental measurements a correlation is given (Equation 3.67), being an average between the curve of the two introduced theories. This latter, has been adopted in the code for the evaluation of the critical Taylor number.

$$Ta_c = 63.3\epsilon^2 - 38\epsilon + 41.2 \tag{3.67}$$

Considering the local Reynolds and Taylor numbers a fluid film bearing can experience transitional flow, Taylor vortex regime or fully turbulent state on the base of the parameter which first reach its critical value. By comparing the critical values of the non-dimensional numbers a threshold of the clearance ratio C_b/R_j has been identified at about 1/2500. For smaller values the turbulence will directly occur while for greater values Taylor vortices are expected before the fully turbulent regime is obtained.

Superlaminar effects are modelled in TILTPAD by means of a simplified approach proposed by Frene et al. [53]. The approach gives a reasonable accuracy for Taylor-Couette vortex flows and transitional regimes

until the fully turbulent condition is reached. By means of the proposed approach, pressure field seems to be slightly affected by Taylor vortices and transitional flows while, on the contrary, dissipative effects are enhanced. Therefore, the code has been modified to take into consideration super-laminar effects during the evaluation of the dissipation function. It has to be noted that the effects of the turbulence on the promotion of the heat transfer are also neglected by means of the followed approach.

In order to include the superlaminar effects, the local turbulent viscosity, referred to the grid of Figure 3.13 and shown in Equation 3.68, is evaluated as a function of the local Reynolds number (Equation 3.69) and of two constants C_1 and C_2.

$$\mu_{ti} = \mu_i(1 + C_1 Re_i^{C_2}) \tag{3.68}$$

$$Re_i = \frac{\rho \Omega R_j h_i}{\mu_i} \tag{3.69}$$

Three sets of constants have been tested among some of the several models proposed in literature, whose a comparison is furnished in by Bouard et al. [72] for fully turbulent state prediction. From the cited work, the Constantinescu's model, based on the Prandtl's mixing length, resulted to be the more attractive one. Hence, two sets of constants have been adopted from the works of Constantinescu [73], [74] and Constantinescu and Galetuse [75]. Furthermore another set of constants proposed in Deng [68] from the work of Hirs [76], based on the bulk flow theory, have been considered. This latter, characterized by $C_1 = 0.00818$ and $C_2 = 0.75$, has been selected for the superlaminar model due to the better agreement obtained. The obtained turbulence model is hereinafter referred to as MT3.

3.9 Coupling between Reynolds and energy equations

The coupling between the Reynolds' and energy equations is obtained by means of the iterative procedure whose flow chart is shown in Figure

3.15. As it is possible to observe the coupling procedure includes the research of the pads' equilibrium positions. This has been chosen for handling realistic pads configurations while solving the energy equation in order to prevent the instability that could arise in non-physical configurations.

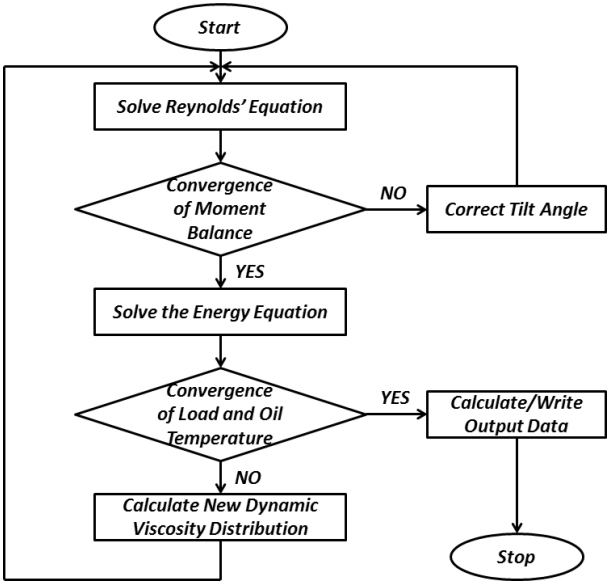

Figure 3.15: Flow chart of the iterative coupling procedure between Reynolds and energy equations.

An under relaxation coefficient has been used for the temperature variation in order to limit numerical oscillations during the coupling procedure. Different values have been tested on two different cases: a five pads tilting pad bearing with a diameter of 140 mm and the large four pads bearing presented in the work of Taniguchi et al. [51]. Results from direct problem calculations, normalized with respect to the case without relaxation (i.e., the case with $\alpha_{URC} = 1$), are shown in Figure 3.16.

As it is possible to observe, an increase in convergence rate is obtained

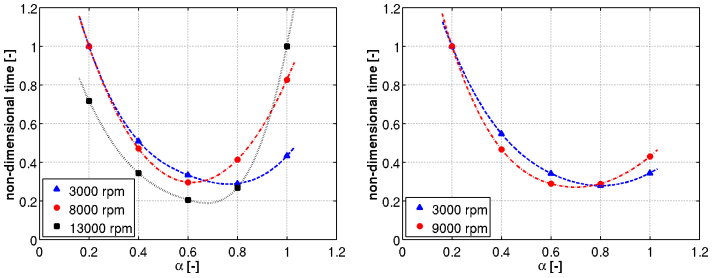

(a) Five pads bearing in LOP configuration with $D = 140mm$

(b) Four pads bearing in LBP configuration with $D = 479mm$

Figure 3.16: Under relaxation coefficient testing

if an under relaxation coefficient is adopted. Values of $0.6 \leq \alpha_{URC} \leq 0.8$ have shown the best results in terms of convergence rate, resulting in three to five times faster calculations.

The same values of α_{URC} have been tested on the five pads bearing for the inverse problem, which is the classical analysis approach.

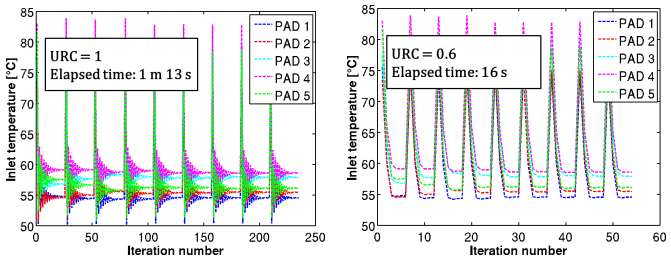

(a) Inverse problem without under relaxation coefficient

(b) Inverse problem with under relaxation coefficient $\alpha_{URC} = 0.6$

Figure 3.17: Under relaxation coefficient testing

Results, shown in Figure 4.6, highlight huge calculation time saving. The benefits of the relaxation coefficient are repeated for each position tested by the code during the shaft's equilibrium research procedure. The relaxed calculation resulted about five times faster.

3.10 Dynamic coefficients

Vibration and critical speed problems in rotating machines are growing more and more important with the increasing speed and performance to be obtained. Since the dynamic behaviour of a rotor is strongly influenced by the characteristics of its supports, the analysis of these problems require the knowledge of the response of the bearing lubricant film to journal displacements and velocities in terms of forces.

When the journal orbit size is relatively small with respect to the bearing clearance, it is possible to replace the fluid film forces with their gradients evaluated at the steady state equilibrium position X_0, Y_0, as presented in the work of Lund [77]. The dynamic forces are then directly proportional to the displacements (ΔX, ΔY) and velocity perturbations ($\Delta \dot{X}$, $\Delta \dot{Y}$) and can be calculated as reported in Equations 3.70 and 3.71, where K_{ij} and C_{ij} are respectively called the linearised stiffness and damping coefficients. This section is devoted to the calculation of these latter.

$$F_X = -(K_{xx}\Delta X + K_{xy}\Delta Y + C_{xx}\Delta \dot{X} + C_{xy}\Delta \dot{Y}) \tag{3.70}$$

$$F_Y = -(K_{yx}\Delta X + K_{yy}\Delta Y + C_{yx}\Delta \dot{X} + C_{yy}\Delta \dot{Y}) \tag{3.71}$$

A general overview to the calculation problem is given in the work of He et al. [78] where the effects of direct and cross-coupled coefficients are also examined in relation to the stability of the global system.

Several factors have been considered in literature to affect the problem: e.g., frequency of excitation as considered in the work of Parsell et al. [79], pads and pivot flexibility, pads preload and clearance thermal variations. Some of the main differences between calculated values and measured ones can be in fact be ascribed to these factors as reported in the work of Wilkes and Childs [80].

The classical approach with synchronously reduced coefficients, widely diffused in industry, is considered for the purpose of the present thesis due to its reasonable engineering approximation as also reported in the work of Parsell et al. [79].

Different strategies have to be adopted for different type of bearings and hence will be introduced separately for the fixed geometry and for the tilting pad bearings.

3.10.1 Plain bearings

In case a fixed geometry bearing is considered the procedure is straightforward. In fact, since the code is able to calculate the resulting force once a position is defined (that is a direct problem), with or without imposed shaft velocities, it is possible to directly evaluate the forces with respect to the shaft displacement or velocity perturbations. The resulting dynamical forces, derived from eight calculations (four perturbed displacements around the equilibrium position and four shaft velocity perturbations on the equilibrium position), can be then used to approximate the local gradients and calculate the terms of the dynamic matrices as shown in Equations 3.72, 3.73.

$$\begin{aligned} K_{xx} &= \frac{\partial F_X}{\partial X} = \frac{\Delta F_X}{\Delta X} & K_{xy} &= \frac{\partial F_X}{\partial Y} = \frac{\Delta F_X}{\Delta Y} \\ K_{yx} &= \frac{\partial F_Y}{\partial X} = \frac{\Delta F_Y}{\Delta X} & K_{yy} &= \frac{\partial F_Y}{\partial Y} = \frac{\Delta F_Y}{\Delta Y} \end{aligned} \tag{3.72}$$

$$\begin{aligned} C_{xx} &= \frac{\partial F_X}{\partial \dot{X}} = \frac{\Delta F_X}{\Delta \dot{X}} & C_{xy} &= \frac{\partial F_X}{\partial \dot{Y}} = \frac{\Delta F_X}{\Delta \dot{Y}} \\ C_{yx} &= \frac{\partial F_Y}{\partial \dot{X}} = \frac{\Delta F_Y}{\Delta \dot{X}} & C_{yy} &= \frac{\partial F_Y}{\partial \dot{Y}} = \frac{\Delta F_Y}{\Delta \dot{Y}} \end{aligned} \tag{3.73}$$

3.10.2 Tilting pad journal bearings

The use of tilting pad bearings, with their better dynamic characteristics (see the work of He et al. [78]), has allowed average rotor speed to increase up to more than 10000 *rpm* in many turbomachinery applications, as reported in the work of Allaire et al. [81].

The analysis of these components is complicated by the additional degrees of freedom associated with the tilting motion of the pads, respectively θ_i and $\dot{\theta_i}$, which need to be considered together with the journal degrees of freedom proper of conventional bearings. As a consequence, in

addition to the dynamical coefficients associated to the shaft's perturbations, the degrees of freedom of the pads produce stiffness and damping coefficients associated with pads' perturbations.

Two main approaches have been found in literature:

- Calculating the complete set of dynamic coefficients

- Adopting synchronously or non-synchronously reduced coefficients.

The first approach is considered in the pad perturbation methods, as the one proposed in the work of Allaire et al. [81]. In this method the complete bearing coefficients are calculated considering pads degrees of freedom. Then the bearing characteristics can be used directly for the rotor analysis or can be reduced by assuming either synchronous or non-synchronous pads motion. The main problem is the need to evaluate $8 + 10 \cdot n$ dynamical coefficients (where n is the number of pads).

The synchronously reduced approaches, considered in the present thesis, is taken from the widely adopted pad assembly method (PAM) of Lund [77]. The main objective of this works is to reduce the dynamical coefficients associated with the pads and the shaft to equivalent coefficients associated only with the shaft motion. This is done by assuming synchronous motion of the pads with respect to the shaft. Since the work is referenced, only some information on the method is given here.

The Pad Assembly Method (PAM) of Lund uses available or directly calculated partial arc bearing coefficients for all of the shaft perturbations. Here, local coefficients are calculated by the code considering fixed pads. Then, synchronous pad motion is adopted in order to reduce the system to the shaft motion only (i.e., in order to eliminate the pads perturbation terms). The local coefficients obtained are then transported in the global (X, Y) reference system and then assembled in order to give the complete dynamical matrices of the bearing.

3.11 Grid sensitivity analysis

A grid sensitivity analysis has been performed for TPJBs cases. The aim is to evaluate the effects of the discretization on the obtained results and enable to define a good trade off between accuracy and computational cost in terms of number of elements along the axial and tangential directions.

Two test case have been adopted for the purpose: the five pads TPJB, with a diameter of 140 mm (referred to as K-5) and the large four pads TPJB from the work of Taniguchi et al. [51] (referred to as T-4). Both direct and inverse problem have been tested for the K-5 case while only direct problem has been analysed on the T-4 one. The test cases and their operating conditions are shown respectively on Sections 3.12.8 and 3.12.6.

Four grids have been tested for each case and their main characteristics are reported in Table 3.3. The coarsest grid (GRID-01) has been defined with its $NX = 5$ and $NZ = 5$, then, the refinement has been performed by means of doubling both the number of rectangular elements along the tangential and axial directions.

GRID ID	NX	NZ	rectangular elem.	triangular elem.
GRID-01	5	5	25	100
GRID-02	10	10	100	400
GRID-03	20	20	400	1600
GRID-04	40	40	1600	6400

Table 3.3: Grid sensitivity analysis: characteristics of the tested grids.

Figure 3.18 shows the obtained grids in terms of rectangular elements and the related pressure fields.

Results are analysed in terms of global working parameters both for the direct and inverse problem. In particular, when a direct problem is solved, the results are shown in terms of bearing load carrying capacity (load module) and frictional power losses. Instead, when inverse problem are solved the load module is substituted by the eccentricity ratio (in

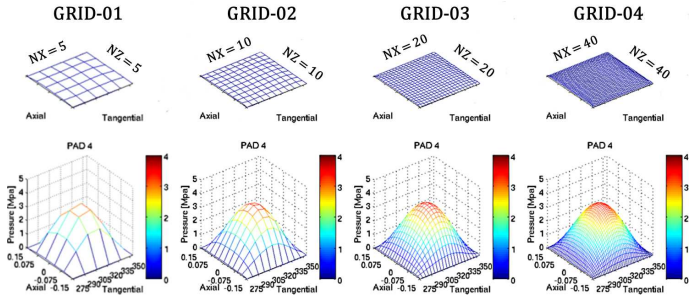

Figure 3.18: Grid sensitivity analysis: effects of the grid refinement on the pressure field of the fourth pad of the Taniguchi et al. [51] test case.

this case in fact the load module is an input of the problem). The shown results are normalized with respect to the values obtained by means of the finest grid (GRID-04).

Figure 3.19 shows the results of both the test cases in the direct problem approach. The K-5 test case results to be less sensitive to the grid discretization with differences between GRID-01 and GRID-04 about 5% while the T-4 case has shown difference of about 8%. Furthermore, between the two analysed data type, the load module (or eccentricity) results to be more sensitive to the discretization.

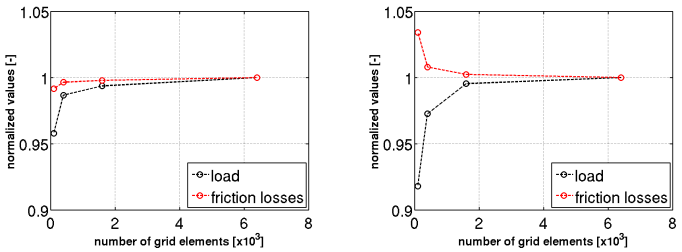

(a) Direct problem Kingsbury TPJB **(b)** Direct problem Taniguchi et al.

Figure 3.19: Grid sensitivity analysis for direct problem: normalized frictional power P_f losses and load module L.

For both the test cases, in order to have an effect of the grid on the results below the imposed calculation accuracy, which is usually of a few percent (e.g., the load module accuracy usually imposed is about $1\% \div 2\%$), the number of elements to be considered is about $NX = 20$ and $NZ = 20$.

Similar conclusions can be obtained considering the inverse problem results (Figure 3.20). It is interesting to note that the eccentricity ratio is overestimated when a coarse grid is adopted while coherently the load module is underestimated. This can be explained looking at Figure 3.18. In fact, the coarsest grid (GRID-01) shows a very sharp pressure field distribution with segments connecting two points usually below the physical pressure distribution (better represented by GRID-04).

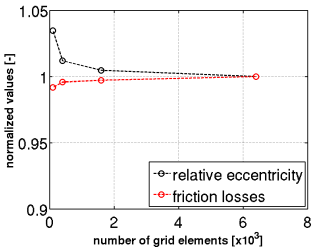

Figure 3.20: Grid sensitivity analysis for inverse problem: normalized frictional power P_f losses and load module L (Kingsbury TPJB).

Once the analysis has been performed on the TPJBs similar levels of discretization have been adopted for PJBs. The discretization adopted for the PJB in the tangential and axial directions are respectively shown in equations 3.74 and 3.75.

$$NX_{pjb} \simeq \frac{R_{j-tpjb} \cdot \Delta\delta_{pad}}{NX_{tpjb}} R_{j-pjb} \Delta\delta_{pjb} \tag{3.74}$$

$$NZ_{pjb} \simeq \frac{B_{tpjb}}{NZ_{tpjb}} B_{pjb} \tag{3.75}$$

3.12 Validation results

The code for the thermo-hydrodynamic analysis (TILTPAD) has been validated by means of comparison with experimental data, where available, or with numerical data obtained by means of commercial codes. Results have been analysed in terms of global performance parameters, both static and dynamic, although some local variables have been also considered. More in detail, global parameters are generally: equilibrium position, minimum film thickness, frictional power losses and dynamic coefficients, while the local parameters considered are pressure and temperature fields.

Four different test cases have been considered for the purpose of the validation of the plain journal bearing version of the code and other four cases for the tilting pad journal bearing configuration. All of the obtained results, based on the discretization studied in Section 3.11, are presented in the following subsections.

3.12.1 PJB: Ferron et al. test case

The first test case adopted is the one proposed by Ferron et al. [44]. It is a cylindrical bearing with one feeding groove studied at the University of Poitiers. In their work, results from a numerical code, developed at INSA of Lyon, are also presented and will be hereinafter referred to as "Theory". Their code solves the Reynolds' equation including the effects of viscosity variations, which are accounted by means of a three-dimensional energy equation. A conjugate heat transfer analysis if adopted to solve the temperature field both within the fluid film, the shaft and the bush.

The main operating conditions of the test case are reported in Table 3.4. Same conditions have been adopted for the numerical simulations.

Figure 3.21 shows comparison of the numerical and experimental data in terms of eccentricity ratio ϵ with respect to the Sommerferld number

Bearing operating characteristics	
Journal radius $[mm]$	50
Bearing length $[mm]$	80
Radial clearance (20 $^\circ C$) $[\mu m]$	145
Groove angle $[deg]$	18
Rotational speed range $[rpm]$	1000 $\div$ 4500
Load range $[kN]$	1 $\div$ 10
Lubricant viscosity (40 $^\circ C$) $[Pas]$	0.0277
Lubricant density $[kg/m^3]$	860
Lubricant specific heat $[J/kgK]$	2000
Inlet lubricant temperature $[^\circ C]$	40
Ambient temperature $[^\circ C]$	40
Inlet lubricant pressure $[kPa]$	70

Table 3.4: Operating conditions adopted for the numerical simulations of the test case of Ferron et al. [44].

(So). Definition of both the variables are shown in Equations 3.76, 3.77:

$$\epsilon = \frac{e}{C_b} \tag{3.76}$$

$$So = \frac{\mu N B D}{L}(\frac{R_j}{C_b})^2 \tag{3.77}$$

where e is the eccentricity, L is the load, B and R_j are respectively the axial length and the radius, N is the rotational speed and μ is the dynamic viscosity of the oil.

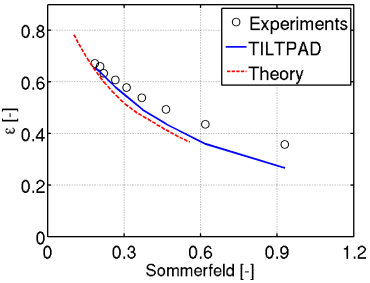

Figure 3.21: Comparison between experimental results and numerical calculations: eccentricity ratio.

A good trend prediction is obtained with respect to the experimental data, although, at high Sommerfeld numbers, the discrepancy is quite significant (a peak of about 25% is reached with respect to the experiments for the highest Sommerfeld number tested). According to the work of Ferron et al. [44] the effects of the thermal deformation, and hence of the increase in the bearing clearance, results to be the cause for such a difference. Better agreement is obtained, in fact, if results are compared with Ferron "Theory".

In terms of local bearing behaviour, results of pressure and temperature peaks are shown respectively in Figures 3.22(a) and 3.22(b).

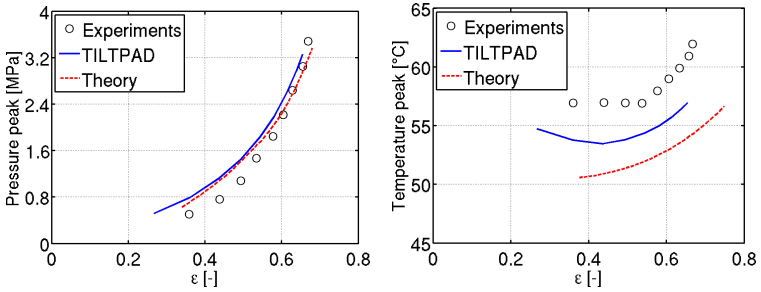

(a) Pressure peak with respect to the shaft eccentricity ratio.

(b) Temperature peak with respect to the shaft eccentricity ratio.

Figure 3.22: Comparison between experimental results and numerical calculations: pressure and temperature peaks.

About the pressure, good results are obtained in terms of trend prediction, with a better agreement for high eccentricity ratios with respect to lower ones. Discrepancies raise up to 37% with respect to the experimental data for low ϵ values, which are related to high Sommerfeld numbers. The effects of the thermal deformation can be again considered in order to explain such an high difference. In fact, if results are compared with the numerical code of the authors of the experimental work better agreement is obtained.

In terms of temperature peaks, trends are again well predicted, while a general underestimation is obtained. Such a misprediction is also high-

lighted for the numerical code adopted as a further validation.

It has to be specified that for all of the test case considered when TILTPAD temperatures are compared with experimental data, different kind of variables are compared. In fact, while the experimental temperature is measured a few millimeters below the metallic surface of the bush or of the pads, the temperature calculated by the code with its one-dimensional equation is substantially an average temperature value.

What has been discussed referring to Figure 3.22 can be explained looking at Figures 3.23(a) and 3.23(b), where pressure and temperature fields are shown for the case at 4000 *rpm* and 6000 *N*.

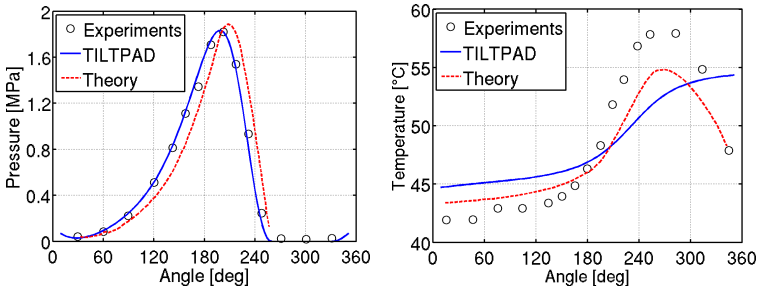

(a) Local pressure distribution. **(b)** Local temperature distribution.

Figure 3.23: Comparison between experimental results and numerical calculations: local pressure and local temperature.

Pressure distribution is well represented by the code with very slight differences with respect to the theoretical results. This could be expected since an inverse problem is solved and hence the pressure distribution needs to generate a load carrying capacity of 6000 *N*. Hence, for this kind of analysis, thermal deformations are expected to affect the equilibrium position more than the pressure distribution.

In terms of temperature good orders of magnitude and trends are obtained, except for tangential angles above 270 *deg*, where experimental and Theory values decrease while TILTPAD slightly increases. This misprediction is related to the bush conductivity effects which are strongly af-

fected by the proximity to the oil feeding groove. About the temperature peak, both the codes show lower values with respect to the experimental ones. The authors of the experimental campaign are able to justify the difference of 4 $^{\circ}C$ by means of the uncertainty of the bush conductivity, thanks to their accurate model. TILTPAD discrepancies, which has a maximum value of about 5 $^{\circ}C$, are both affected by the simplification of the model and by the different variables compared (local versus averaged values).

3.12.2 PJB: Glienicke test case

The second test case adopted for the purpose of validation is the cylindrical single grooved bearing proposed in the work of Glienicke [82] and studied at the Institute for Mechanical Design and Automobile Construction, Technical Institute, Karlsruhe.

Some of its main operating characteristics, which have been adopted for the simulations, are shown in Table 3.5.

Bearing operating characteristics	
Journal radius $[mm]$	60
Bearing length $[mm]$	60
Radial clearance $[\mu m]$	114
Rotational speed range $[rpm]$	$0 \div 10000$
Load range $[kN]$	$1 \div 35$
Lubricant viscosity (40 $^{\circ}C$) $[Pas]$	0.0563
Lubricant density $[kg/m^3]$	860
Lubricant specific heat $[J/kgK]$	2000
Inlet lubricant temperature $[^{\circ}C]$	40
Inlet lubricant pressure $[Pa]$	98675

Table 3.5: Operating conditions adopted for the numerical simulations of the test case from the work of Glienicke [82].

Results are shown in Figure 3.24 in terms of eccentricity ratio and non-dimensional minimum film-thickness (h_{min}/C_b) with respect to the Sommerfeld number. This latter is here calculated as shown in Equation

3.78.

$$So = \frac{L}{\mu \Omega B D} (\frac{C_b}{R_j})^2 \tag{3.78}$$

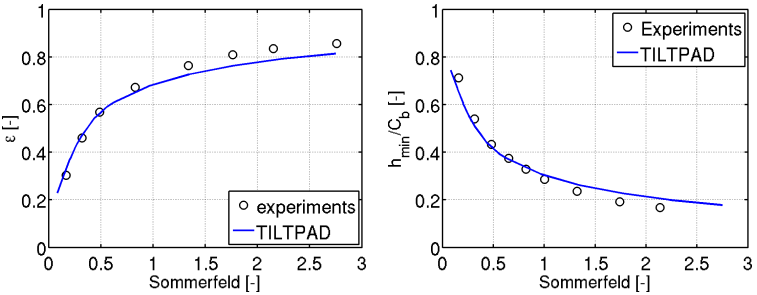

(a) Eccentricity ratio with respect to the Sommerfeld number

(b) Non-dimensional minimum film-thickness with respect to the Sommerfeld number

Figure 3.24: Comparison between experimental results and numerical calculations (TILTPAD).

Good agreement is obtained for both the analysed variables. It has to be noted that the eccentricity ratio and the minimum film-thickness are strongly related by geometrical characteristics which include the attitude angle. Since one is well predicted the other comes as a consequence. A maximum difference in terms of eccentricity ratio of about -5% with respect to experimental data is obtained at the highest Sommerfeld number.

3.12.3 PJB: Lund and Tonnesen test case

Another test case, proposed in the work of Lund and Tonnesen [46], shows results of a cylindrical journal bearing with two feeding grooves. The main operating parameters are shown in Table 3.6.

A very good agreement with experiments is obtained in terms of eccentricity ratio (Figure 3.25(a)) and frictional power losses (Figure 3.25(b)) both for 3500 *rpm* and for 5000 *rpm* along the whole range of tested

Bearing operating characteristics	
Journal radius $[mm]$	50
Bearing length $[mm]$	55
Radial clearances $[\mu m]$	66.8 and 68.6
Rotational speed tested $[rpm]$	3500 and 5000
Load range $[kN]$	$1 \div 10$
Lubricant viscosity (50 $^\circ C$) $[Pas]$	0.0183
Lubricant density $[kg/m^3]$	850
Lubricant specific heat $[J/kgK]$	2000
Inlet lubricant temperature $[^\circ C]$	50
Ambient temperature $[^\circ C]$	20
Inlet lubricant pressure $[kPa]$	120 and 150

Table 3.6: Operating conditions adopted for the numerical simulations of the test case from the work of Lund and Tonnesen [46].

loads, with maximum differences always below 2.5% with respect to the experimental values. It has to be underlined that the assessment of the modified mixing model, shown in Appendix B, has been performed on the present test case for a rotational speed of 3500 rpm and with a load of 5600 N.

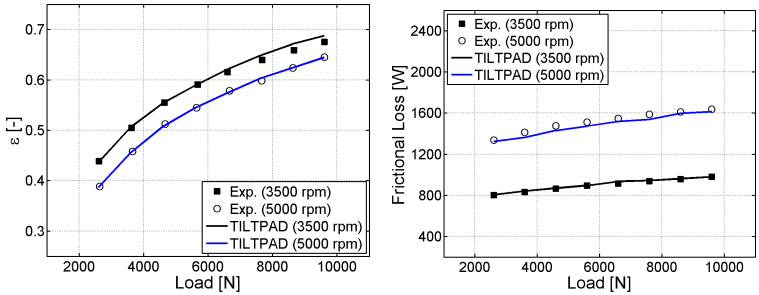

(a) Eccentricity ratio. **(b)** Friction losses.

Figure 3.25: Comparison between numerical and experimental results.

In terms of pressure field, shown in Figure 3.26 for 3500 rpm and 8600 N, a difference of about 12 % is highlighted in terms of maximum pressure peak. Non considering the pressure measurements tolerance, which is of

about ±4%, the source for the discrepancy can be ascribed at the sub-ambient pressure obtained in the cavitating regions both on the loaded sector of the bearing and on the unloaded region. Better agreement is in fact obtained with the numerical calculations, also presented in the work of Lund and Tonnesen [46], where ambient temperature is set in the cavitated region according to the Reynolds condition. The tolerance on the experimental data is highlighted by the authors of the experimental campaign, due to different pressure measurements obtained along several shaft rotations. In fact, due to the cavitated region, where striae are present, measurements result different if the probe is in a striae, giving ambient pressure, or between two striae, giving sub-ambient pressure.

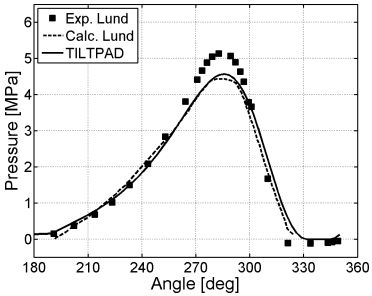

Figure 3.26: Comparison between numerical and experimental results: pressure field (MPa) at 3500 rpm and 8600 N.

About local temperature distributions, shown in Figure 3.27 for the 3500 rpm and 5000 rpm, orders of magnitude and trends are quite well predicted, particularly considering that local experimental temperatures are measured at the bearing bush while TILTPAD data are mean film values. More in detail, in the unloaded section of the bearing, where the ruptured film zone is located, the trend is not well predicted. This has to be ascribed to a backflow recirculation from the groove into the unfilled space, where the film is striated, as described in Lund and Tonnesen [46]. Comparing the obtained results with the mean temperature presented in the referenced paper, both trends and values are in better agreement.

Considering the loaded sector, the maximum temperature differences are obtained for the 5000 *rpm* case at its inlet, with values of about $+9.2\ ^{\circ}C$ and $+4.9\ ^{\circ}C$ with respect to the experiments and to the Lund's calculated mean values respectively.

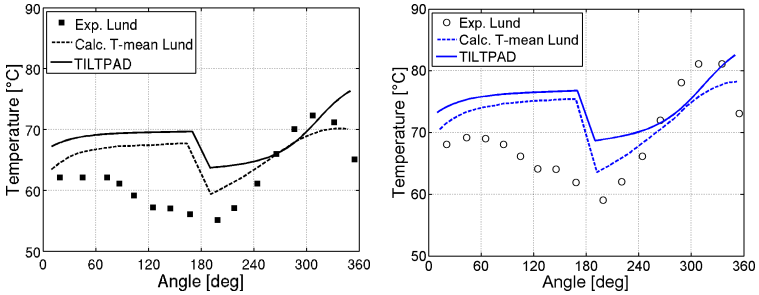

(a) Temperature at 3500 rpm. **(b)** Temperature at 5000 rpm.

Figure 3.27: Comparison between numerical and experimental results: temperature field ($^{\circ}C$).

3.12.4 PJB: Someya test case

The last test case considered for the validation of the plain journal bearing version of the code is one of the cases proposed in the work of Someya et al. [83]. This test case has been selected in order to compare calculated and measured dynamic coefficients. A cylindrical bearing with two feeding grooves is considered for the purpose and some of its main characteristics are resumed in Table 3.10.

Results are shown in terms of eccentricity ratio and dynamic coefficients, both direct and cross coupled, with respect to the Sommerfeld number (defined as in Equation 3.77).

In terms of eccentricity ratio, shown in Figure 3.28, results are quite good in terms of trend and order of magnitude, although a 23% is obtained for the maximum Sommerfeld number tested. Similar results were obtained for the Ferron et al. [44] test case, shown in Figure 3.21, where thermal effects were the main reason for the misprediction. Although

Bearing operating characteristics	
Journal radius $[mm]$	50
Bearing length $[mm]$	50
Radial clearances $[\mu m]$	140
Rotational speed tested $[rps]$	$26 \div 100$
Load range $[kN]$	$0.367 \div 4.5$
Lubricant viscosity (50 $^\circ C$) $[Pas]$	0.0192
Lubricant density $[kg/m^3]$	860
Lubricant specific heat $[J/kgK]$	2000
Inlet lubricant temperature $[^\circ C]$	50
Ambient temperature $[^\circ C]$	20
Inlet lubricant pressure $[kPa]$	100

Table 3.7: Operating conditions adopted for the numerical simulations of the test case from the work of Someya et al. [83].

similar considerations could be reasonably done for the present case, not enough informations are provided in the bearing databook from which the present test case is extracted. Furthermore, with the formulation adopted for the Sommerfeld number in the present case, the higher the Sommerfeld, the higher the rotational speed or the lower the load. Hence, since the bearing is expected to work with a reduced eccentricity at higher Sommerfeld number values, the Petroff's type hypothesis should give more reliable results supporting the hypothesis of thermal deformation effects with respect to lack of accuracy in the numerical model.

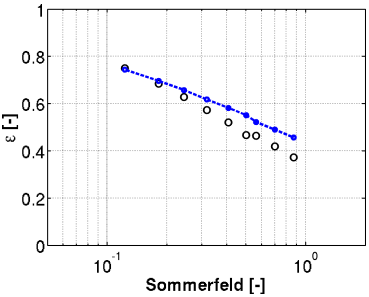

Figure 3.28: Comparison between numerical and experimental results from the work of Someya et al. [83]:eccentricity ratio [−].

The dynamic coefficients presented in Figure 3.29 are expressed in their non-dimensional form according to the formulations proposed in Equations 3.79 and 3.80, where C_b is the radial bearing clearance, L is the static load and Ω is the rotational speed.

$$K_{ij}^{*} = K_{ij}\frac{C_b}{L} \tag{3.79}$$

$$C_{ij}^{*} = C_{ij}\frac{C_b\Omega}{L} \tag{3.80}$$

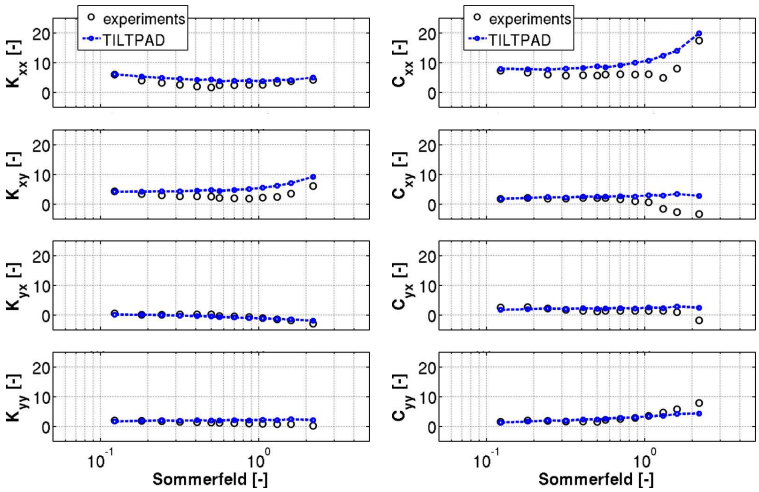

(a) Non-dimensional spring coefficient. **(b)** Non-dimensional damping coefficient coefficient.

Figure 3.29: Comparison between numerical and experimental results from the work of Someya et al. [83].

A good trend and orders of magnitude prediction is obtained for both direct and cross-coupled stiffness coefficients as well as for direct and cross coupled damping coefficients. Yet again the maximum differences between experimental data and numerical predictions are obtained at higher Sommerfeld number, where the maximum misprediction of eccen-

tricity was obtained. Since the calculation of the dynamic coefficient is strictly related to the position of the shaft, it is possible to imagine an influence of this latter on the misprediction of the dynamic coefficients obtained at high Sommerfeld number.

3.12.5 TPJB: Brockwell and Kleinbub test case

Considering tilting pad applications, a five pads journal bearing in a load between pads configuration is considered from the work of Brockwell and Kleinbub [84]. Data are presented in terms of differential eccentricity ratio, friction coefficient and temperature field.

Differential eccentricity is here evaluated as the vertical distance (non-dimensional with respect to C_b) between the obtained results and the result of a reference case, characterized by 83 Hz and 450 N. The friction coefficient, shown in Equation 3.81, is evaluated dividing the obtained friction force L_f by the applied load L. Sommerfeld number is evaluated by means of Equation 3.78.

$$f_f = \frac{L_f}{L} = \frac{P_f}{R_j \Omega L} \tag{3.81}$$

The operating conditions characteristic of the test case as summarized in Table 3.8.

Bearing operating characteristics	
Journal radius $[mm]$	38
B/D $[-]$	0.75
Assembled bearing clearance $[\mu m]$	60
Pads' preload (m) $[-]$	0
Number of pads (NP) $[-]$	5
Bearing-load configuration $[-]$	LBP
Rotational speed tested $[rpm]$	1000 ÷ 10000
Load range $[kN]$	2.225, ÷ 8.90
Lubricant oil $[-]$	$ISOVG32$
Inlet lubricant temperature $[°C]$	50

Table 3.8: Operating conditions adopted for the numerical simulations of the test case from the work of Brockwell and Kleinbub [84].

A good prediction of the equilibrium position (Figure 3.30(a)) is obtained for both the tested configurations (i.e. 2225 and 4450 N at various shaft rotations) although with a general underestimation. The maximum difference between the calculated data and the experiments is a -14% obtained for the case at 3600 rpm and 4450 N. It is necessary to observe also a comparable scatter of the reported experimental data.

Same considerations can be done for the friction coefficient, shown in Figure 3.30(b), where a good agreement is globally obtained, yet again, numerical discrepancies are comparable with the scatter of the experimental data.

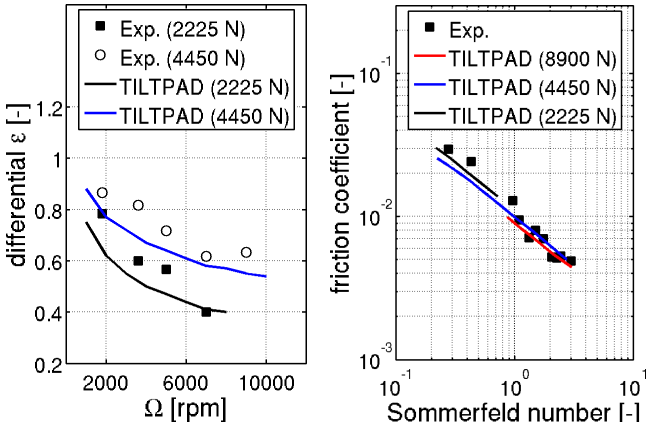

(a) Differential eccentricity ratio.

(b) Friction coefficient.

Figure 3.30: Comparison between numerical and experimental results from the work of Brockwell and Kleinbub [84].

Two configurations have been tested in terms of temperature distribution (i.e., 1800 and 5000 rpm, with 8900 N) and are shown in Figure 3.31. Trends and orders of magnitude are quite well predicted considering what previously reported about mean values calculated from the code and locally measured temperatures. A misprediction of the trend is highlighted for the three unloaded pads of the 1800 rpm configuration. Each time a

mixing is performed the code obtains a lower mean temperature value of the "mixed" oil at the leading edge of the pad while, particularly for pad number three, experiments show an increase of temperature after mixing. The maximum differences on the loaded pads is obtained at the inlet of the fourth pad and at the outlet of the fifth one with respectively a -6.2 $^{\circ}C$ and $+9.6$ $^{\circ}C$ with respect to the experimental data for the 1800 rpm case.

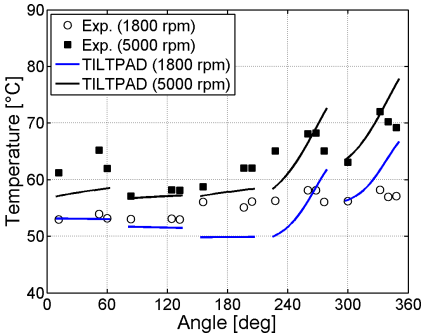

Figure 3.31: Comparison between numerical and experimental results from the work of Brockwell and Kleinbub [84]: temperature field [$^{\circ}C$].

3.12.6 TPJB: Taniguchi et al. test case

The proposed test case is a large four pads TPJB in a load between pads configuration. Taken from the work of Taniguchi et al. [51] this test case case has been previously referred to as T-4 when the grid sensitivity analysis has been presented. Such a large bearing operates in the transitional and fully turbulent regime and hence is adopted in order to evaluate the potential of the code in handling superlaminar regimes. Results are compared also with the FEM code presented by the authors, which is quite complete (i.e., both pressure and energy equations consider the effect of turbulence) and very well predicts all of the presented data. The operating conditions are shown in Table 3.9.

In terms of eccentricity ratio, shown in Figure 3.32(a) for a global

Bearing operating characteristics	
Journal radius $[mm]$	239.5
B/D $[-]$	0.626
Assembled bearing clearance $[\mu m]$	612
Pads' preload (m) $[-]$	0
Number of pads (NP) $[-]$	4
Bearing-load configuration $[-]$	LBP
Rotational speed tested $[rpm]$	$500 \div 5000$
Load range $[kN]$	$20, \div 320$
Lubricant oil $[-]$	$ISOVG32$
Inlet lubricant temperature $[^{\circ}C]$	40

Table 3.9: Operating conditions adopted for the numerical simulations of the test case from the work of Taniguchi et al. [51].

Re of about 1500, an improvement of TILTPAD's prediction is obtained when modeling the superlaminar flow effects (referred to as $MT3$) with respect to the laminar calculation. A slight overestimation is obtained along the whole tested range of loads and could be mainly ascribed to the fact that TILTPAD neglects the effects of turbulence on the pressure calculation, hence reducing the load carrying capacity of the bearing for high Reynolds numbers. It has to be noticed that above 210 kN the code is not able to follow the trend because it has an imposed numerical limit for the maximum allowable eccentricity ratio. Both the highlighted critical zones in Figure 3.32 are related to the exceed of the eccentricity limit. In fact, these results are related to very low rotational speed or very high loads, resulting in high eccentricity values.

In terms of friction power losses, better trends are again obtained for the $MT3$ calculation instead of the laminar one, although the overestimation is here high and increases with increasing rotational speed, so with increasing Reynolds number. The maximum difference is about +40% at 4000 rpm when the Re is about 2000. It is not easy to identify the reason for such a result due to the number of simplification considered in the code, e.g., Poiseuille terms are neglected, turbulent viscosity effects on the pressure field are neglected, unloaded pads are set in a prescribed position. Moreover, the selection of different constants and critical values

from different turbulence models proposed in literature drives to different results. However, some considerations can be done: the more the Reynolds number increases the less neglecting turbulence effects on the pressure field is acceptable, driving the code towards overestimations of the equilibrium eccentricity, and hence, towards the overestimation of the shear stress on the loaded side, that is here evaluated only considering the Couette term. Such an increase in shear stress could directly drive an overestimation of the frictional power loss. Moreover, the overprediction of the equilibrium position increases the local Reynolds number on the unloaded pads and hence their dissipation due to the increase in turbulent viscosity. Unloaded pads contribution to the total frictional power loss raises up to about 50% for high rotational speed.

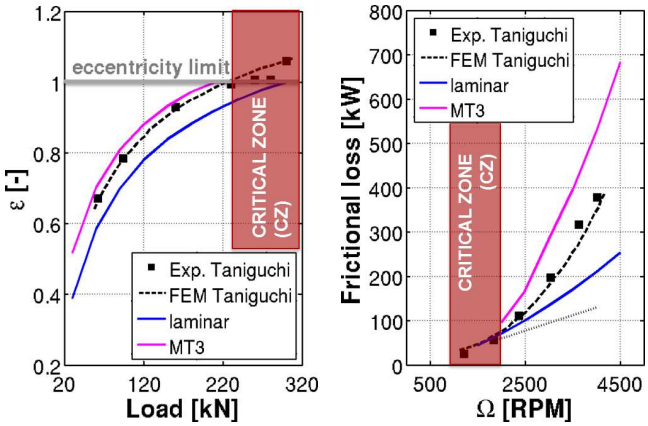

(a) Eccentricity ratio. **(b)** Frictional power losses.

Figure 3.32: Comparison betweeon numerical and experimental results from the work of Taniguchi et al. [51].

Local bearing behaviour is presented in terms of film-thickness, pressure and temperature distributions for 3000 $[rpm]$ and 180 $[kN]$ and are shown in Figure 3.33.

About the film thickness distribution, shown in Figure 3.33(a), better agreement is obtained by the MT3 model with respect to the laminar case

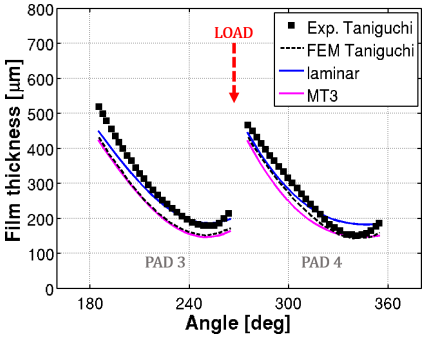

(a) Film-thickness.

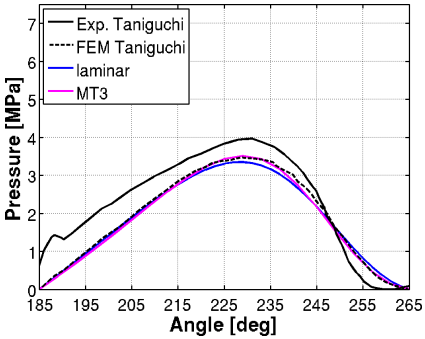

(b) Pressure field on pad 3.

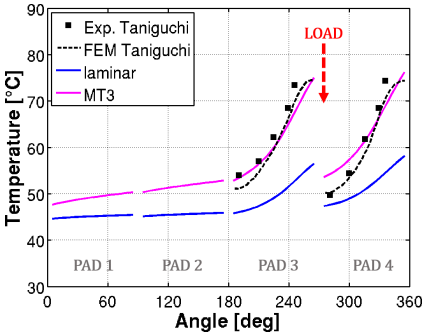

(c) Temperature field.

Figure 3.33: Comparison between numerical and experimental results from the work of Taniguchi et al. [51]: evaluated at 3000 $[rpm]$ and 180 $[kN]$.

due to the better equilibrium position prediction. In particular, better agreement is obtained in the way the superlaminar model represents the variations of the film-thickness along the tangential direction. It has to be noted that the results in this case are very similar to the complete model presented by the authors of the experimental campaign and here referred to as "FEM Taniguchi".

In terms of pressure values (Figure 3.33(b)), all of the models show slight differences with each other. A better reproduction of the trend obtained by the FEM model of Taniguchi et al. [51] is again performed by the MT3 model. This behaviour was expected since an inverse problem is solved. Instead, unexpectedly, all of the models result to be unable to accurately predict the experimental pressure distribution.

In terms of temperature, shown in Figure 3.33(c), a good agreement is obtained with the experimental data, where instead, laminar calculation showed remarkable discrepancies in particular at the outlet of pad number three, with an underestimation of $-18.4\ ^{\circ}C$. Here, mean temperature values result to be quite similar to the experimental local temperature values. This, could probably be ascribed to the mixing promoted by the superlaminar regimes.

3.12.7 TPJB: Someya et al. test case

A test case from the work of Someya et al. [83] has been also considered in order to asses the ability of the code in predicting dynamic coefficients for tilting pad bearing applications. Among the tilting pad presented in the data-book a five pads bearing has been selected for the purpose. Some of its main characteristic are summarized in Table 3.10.

The results obtained by TILTPAD using the pad assembly method of Lund [77] are compared with experimental results and theoretical curves, these latter also found in the work of Someya et al. [83]. Furthermore, eccentricity ratio is also compared with experimental data from the proposed case.

A very good prediction is obtained in terms of eccentricity ratio, shown in Figure 3.34, for the whole tested range of rotational speed.

Bearing operating characteristics	
Journal radius $[mm]$	50
Axial bearing length $[mm]$	50
Pad machined clearance $[\mu m]$	216
Pads' preload (m) $[-]$	0.51
Number of pads (NP) $[-]$	5
Bearing-load configuration $[-]$	LOP
Rotational speed tested $[rpm]$	8000 ÷ 16000
Load $[kN]$	9.8
Lubricant oil viscosity $[Pas]$	0.016
Inlet lubricant temperature $[°C]$	40

Table 3.10: Operating conditions adopted for the numerical simulations of the test case from the work of Someya et al. [83].

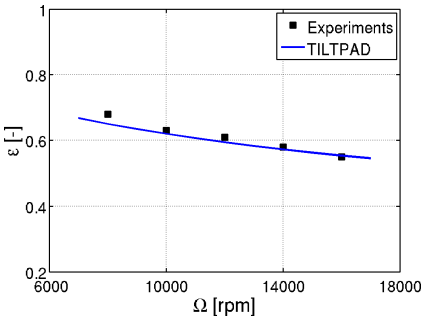

Figure 3.34: Comparison between experiments from the work of Someya et al. [83] and TILTPAD calculations: Eccentricity ratio.

In terms of dynamic coefficient, shown in Figure 3.35, a good prediction is observed for both direct non-dimensional spring coefficients, while an overprediction of the non-dimensional damping coefficient in the x-direction is obtained. Such an overprediction has been also obtained in literature: in the work of Balbahadur [19], where results of the same case at 10000 rpm and 9800 N are presented, and in the work of Someya et al. [83], where results of numerical codes, here referred to as "Theory", are

presented.

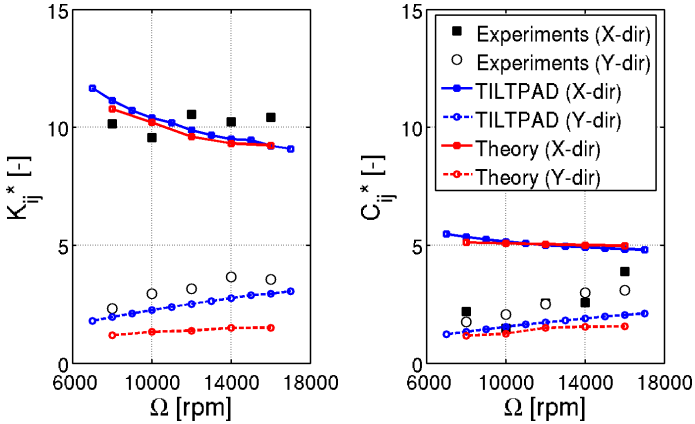

(a) Direct spring coefficients. **(b)** Direct damping coefficients.

Figure 3.35: Comparison between experiments/numerical results from the work of Someya et al. [83] and TILTPAD calculations: Dynamic coefficients.

3.12.8 TPJB: Kingsbury D-140

The last test case here presented, is the one adopted for the Morton effect dedicated experimental campaign presented in Panara et al. [10]. The bearing has been also adopted for the grid sensitivity analysis, where was referred to as K-5. Results are validated by means of comparison with experimental data, where available, and by means of comparison with results obtained from the widely validated commercial code THPAD [85]. Some of the main operating conditions are summarized in Table 3.11.

Three different rotational speeds, 3000 *rpm*, 8000 *rpm* and 13000 [*rpm*], have been selected for the purpose of the validation since they are representative of the range of operating conditions.

The non-dimensional pressure fields, shown in 3.36(a), have been normalized using the bearing unit load as a reference pressure. A very good

Bearing operating characteristics	
Number of pads (NP) [−]	5
Bearing-load configuration [−]	LOP
Rotational speed range [rpm]	$1000 \div 20000$
Lubricant oil [−]	$ISOVG\ 32-46$

Table 3.11: Operating conditions for the numerical simulations of the test case from the Morton effect dedicated campaign.

agreement has been found with the numerical results of THPAD at the lowest rotational speed (3000 rpm), while at 13000 rpm discrepancies up to 33% can be individuated for the "unloaded" pads. Since pressure and temperature fields are coupled, the reason for these variations can be searched in the temperature fields shown in 3.36(b). Temperature values are non-dimensional with respect to the feeding oil temperature (temperature values have been considered in degree Celsius). It can be observed that the pad inlet temperatures are quite different (-12.5% for the higher rotational speed) and then non-negligible changes in the viscosity field are expected. Such a difference can be ascribed to the THPAD mixing model (90% of hot oil carry over and a 10% of cold oil injection) that is different from the one implemented in TILTPAD.

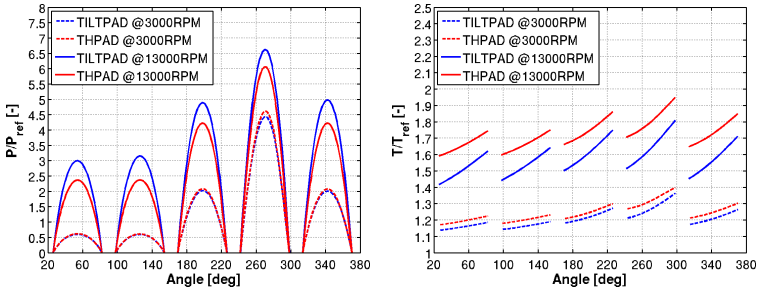

(a) Pressure field. **(b)** Temperature field.

Figure 3.36: Comparison between numerical results from the present work and THPAD of Allaire et al. [81]: pressure and temperature distributions.

CHT results: Kingsbury D-140

In order to estimate the accuracy of TILTPAD in its conjugate heat transfer version, which has been implemented with the purpose introduced in Section 3.7, the code has been compared with available data resulting from the experimental campaign reported in the work of Panara et al. [10]. Non-dimensional temperature on pads, shown in Figure 3.37, have been compared for the most loaded pad of the non-drive end bearing. Results are normalized with respect to the experimental value at 25% of the pad. Since conjugate heat transfer analysis has been performed coherent data of local temperature values are compared. In particular, results are obtained at about 5 *mm* below the pads surface. For the conjugate

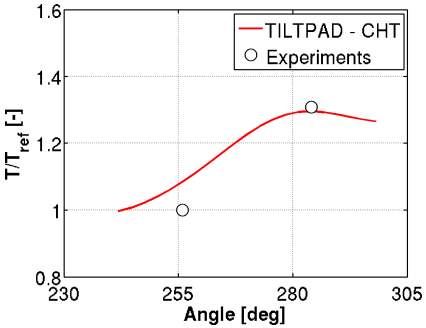

Figure 3.37: Comparison between experiments from the Morton effect dedicated campaign and TILTPAD: pads temperature (CHT approach).

heat transfer simulation the grid of the pads has been obtained imposing 20 elements along the tangential direction, as imposed also for the fluid film grid, while for the radial direction 8 elements have been considered.

Good agreement is obtained. In particular, the characteristic trend of pads temperature is highlighted, with a maximum peak of temperature at about 75% of the tangential pad extension. A slight overestimation is obtained for the temperature at 25% of the pad, with about a +7% with respect to the temperature value adopted as a reference.

Chapter 4

Shaft differential temperature calculation

Contents

This chapter is devoted to the description, testing and validation of the numerical code for the calculation of the differential temperature developed across the shaft during its synchronous precession motion. The objective is to evaluate the temperature coefficient vector, presented in Chapter 1 as B term.

4.1 Quasi-unsteady code development

Among all of the influence coefficients, the determination of B appears to be the most challenging task because predicting such an influential coefficient involves solving a multi-physic problem where fluid lubrication, heat transfer phenomena and rotor dynamics combine in a very complex fashion. Aiming at simplifying such a task, along with a reasonable computational cost, Murphy and Lorenz [16] suggested a calculation method for the amplitude of the B term based on the use of a steady-state TPJB code. Their calculation method is considered here with some modifications, as pointed out in the following sequence:

1. The TPJB code (TILTPAD) is used for all of the given couples of rotational speed and load to be analysed. The corresponding shaft and pads' equilibrium positions (i.e., eccentricities, attitude angles and tilt angles of the pads) are stored together with matrices of stiffness and damping coefficients.

   This step is performed only one time before the real procedure is started. Eccentricities, attitude angles and pads' tilt angles constitute the input data to be used by the quasi-unsteady code (SNAPSHOT), together with geometrical and operating conditions.

2. Once the shaft vibration is given from either experimental testing or unbalance response analysis, orbits are discretized with a prescribed number of points (N_{pso}). Each point is then converted in couples of eccentricities and attitude angles to be used for the film-thickness and temperature calculations.

   The first point along the orbit, from which the discretization process and the subsequent calculations begin, is selected in order to be correspondent to the shaft position on the orbit when time is set as zero.

3. The calculation of the film thickness seen by the journal during its motion (that is for each point along the orbit) is performed without considering the pads dynamics.

In the original method of Murphy and Lorenz a steady state code is used for each point along the orbit. Hence, the tilt angles adopted are step by step the pads' equilibrium configurations. Here, pads motion is neglected during the shaft precession and tilt angles are set as those of the original equilibrium configuration, i.e., assuming the shaft at the centre of the given orbit.

This simplification enables the direct calculation of the film-thickness once the point along the orbit are given. At the same time a faster calculation, in particular for heavily discretized orbits, is obtained because solving the pressure field at each point, for the evaluation of pads equilibrium positions, is avoided. Such an approximation results to be more accurate the more is high the frequency of shaft fluctuations and the more is small the orbit amplitude.

4. A simplified energy equation is then adopted in order to calculate the temperature field seen by the shaft for each position on the orbit. The equation is the same of the one implemented in the steady state code for the analysis of plain and tilting pad bearings, except for the dynamic viscosity, here treated as an equivalent viscosity based on the average temperature rise along the pads.

   Since the equation is based on a Petroff-type hypothesis, there is no need to solve the pressure field, neither for the dissipation function nor for the oil flow rate calculation. As a consequence, the temperature distributions obtained are directly dependent on the evaluated film-thickness, which in turn is a direct consequence of the prescribed shaft position.

5. All of the temperature fields and film-thicknesses calculated by SNAPSHOT are then shifted of prescribed angle steps $\Delta\delta$. In fact, since the output of the code is referred to the fixed external reference system and since the shaft rotates during its motion along the orbit, the fields have to be clocked in order to correctly associate the points standing on the shaft with the film-thickness and temperature field referred to the fixed system.

A precession motion along the orbit is shown in Figure 4.1. The reference point (highlighted in red), stands on the X' axis when the shaft is in the position referred to as 0. Once the shaft has moved to point 1, the reference point has rigidly moved with the rotating reference frame (x,y). Hence, in the fixed frame (X',Y') the reference point has now an higher tangential angle $+\Delta\delta$. In

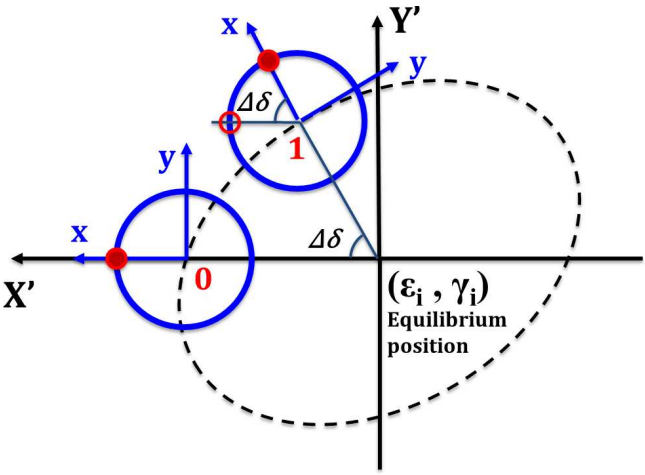

Figure 4.1: Precession motion around the equilibrium position of the $i-th$ running speed.

order to refer to the points on the shaft the temperature fields are all tangentially shifted, with the exception of the first one calculated (see Figure 4.2) which is used as a reference state. Before the signal (i.e, the temperature field) is shifted, a periodic reconstruction is performed both downwind and upwind of the $0 \div 360$ deg range. This is done in order not to loose information when the field to be clocked is shifted, i.e., when a part of the signal is moved outside of the reference domain.

Finally, once shifted, the temperature is interpolated on a grid equal to the one of the reference state (i.e.,the first calculated configura-

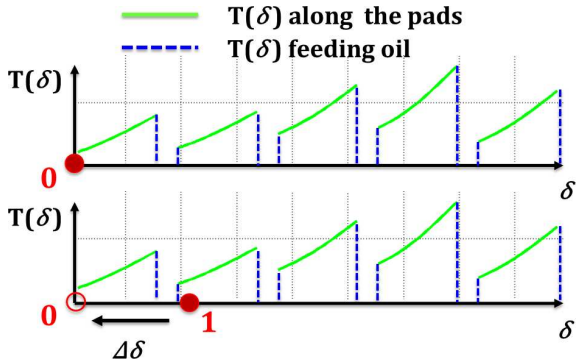

Figure 4.2: Clocking of the thermal fields seen by the shaft along its motion.

tion). This interpolation is needed since the shifting $\Delta\delta$ is strictly dependent on the number of points around the orbit and usually differs from the tangential grid step $\Delta\delta_{pad}/NX$.

6. Temperature fields and film thicknesses clocked to the shaft are finally averaged to find the corresponding mean field temperature and mean film thickness representative of the orbital motion.

7. Mean differential temperature across the shaft and hot-spot position are then evaluated from the averaged field and both phase and amplitude of the differential temperature evaluated. This, enable the calculation of the B term and of the phase shift between high and hot spot.

The algorithm demonstrated to be very efficient even when considering a high number of rotor positions along the orbit and journal surface points. A resume of the input and output of the code is presented in Table 4.1 where the i stands for the $i-th$ running speed and j for the $j-th$ pad of the bearing.

SNAPSHOT data	input	output
Geometry of the bearing	R_j,C_b,m,B,$\Delta\delta_{pad}$	–
Configuration	LOP or LBP	–
Feeding oil	T_{oil},μ_{oil},	–
Running speed	Ω_{max},Ω_{min},$\Delta\Omega$	–
Equilibrium positions	ϵ_i,γ_i	–
Pads tilt angles	θ_{ij}	–
Orbits amplitude	A_{xi},A_{yi}	–
Orbits phase	Φ_{xi},Φ_{yi}	–
Differential temperature	–	ΔT_i
Hot spot position	–	ϕ_i

Table 4.1: Input - Output data of the SNAPSHOT code.

4.1.1 Energy equation

As previously stated, the energy equation adopted is the one implemented in the code for the thermo-hydrodynamic lubrication problem, with the improved mixing model but with an effective viscosity and hence with a general formulation (Equation 4.1) that is equal to the one proposed by Balbahadur [19].

$$\frac{d\tilde{T}}{d\delta} + \frac{2H}{\rho_{oil} c_{oil} \Omega h(\delta)} \tilde{T} - \frac{2\mu_{ave} \Omega R_j^2}{\rho_{oil} c_{oil} h(\delta)^2} \tag{4.1}$$

The choice of adopting such a simplified approach for the solution of the present task has been done on the base of the promising results obtained in the previously cited work [19].

4.1.2 Effective viscosity

Mineral base oils usually show a dynamic viscosity, which tends to decrease with increasing temperature with an approximately exponential trend. The Reynolds exponential law of viscosity is often used for such lubricants. However practical, the exponential law has been reported to yield lower accuracy results when the two reference temperatures upon which the curve is built, are more than 20 K apart and for temperatures outside of the reference temperature interval.

The McCoull and Walther [86] expression is another popular formu-

lation for the modelling of lubricant viscosity-temperature law (reported in Equation 4.2). Explicitly mentioned in the work of Frene et al. [53] for mineral oils it has been adopted in various works in order to perform the thermo-hydrodynamic analysis of journal bearings (e.g., the works of Bouyer [87] and Pierre et al. [88]).

$$log[log(\nu + 0.6)] = c_1 - c_2 log(T) \tag{4.2}$$

In the proposed equation, c_1 and c_2 are coefficients which can be determined from the viscosity measured at two different reference temperatures T_{ref1} and T_{ref2}, while ν is the kinematic viscosity.

With the McCoull-Walther expression the viscosity values obtained for temperatures higher than the reference temperatures do not fall as steeply as with the Reynolds curve. This expression was therefore adopted to calculate the effective viscosity in the present task where, due to the orbital motion around the equilibrium position, some critical configurations in terms of temperature increase are expected especially for high-amplitude displacements.

4.1.3 Feeding oil temperature treatment

The numerical code do not include into the domain the space between the pads where feeding oil is released and where the mixing between hot and cold oil is obtained. Therefore, the thermal field is available only on top of the pads.

Since the 360 *deg* of the shaft see the whole bearing system the space between the pads has been filled with artificial temperatures. For the purpose, the available numerical grid has been expanded trying, where possible, to maintain a similar discretization level. Two temperature trend have been tested in order to model feeding oil effects.

A constant temperature value equal to the feeding oil temperature has been considered at first. The choice was driven by the aim to find a trend representative of the expected cooler zone, which results to be far from a realistic trend if, for example, an hot oil carry over is considered.

This approach is shown on top of Figure 4.3.

A linear trend has been then considered in order to be more representative of a mixing process. The temperature is linearly varied from the outlet temperature of the upwind pad to the inlet temperature of the downwind one as shown on the bottom of Figure 4.3. The two ap-

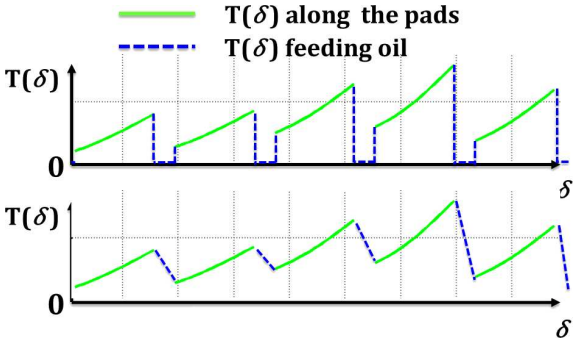

Figure 4.3: Tested solutions for the feeding oil treatment. Flat trend (top) and linear trend (bottom).

proaches showed similar behaviour. Therefore, the flat trend solution has been adopted.

4.1.4 Superlaminar effects

Superlaminar effects are also modeled in SNAPSHOT. The same simplified approach proposed by Frene et al. [53] and described when presenting TILTPAD has been considered for the purpose. A dedicated section has been given to the topic in the previous chapter (see Section 3.8).

4.2 Description of the test case

Due to the lack of experimental data in terms of shaft differential temperature, the present code is compared with calculated values from other works found in literature.

The test case adopted for the validation and testing is the double overhung turbo-expander supported on a five pads TPJB presented in the work of Schmied et al. [17] and shown in Figure 4.4. The same machine has been studied by Murphy and Lorenz [16] at 18600 rpm and a value of 0.13 $^{\circ}C/\mu m$ for the B term has been found. About the phase lag between the hot and high spots Murphy and Lorenz did not used their procedure but selected a value of 20 deg as measured during the experimental campaign of De Jongh and Morton [1]. The tilting pad

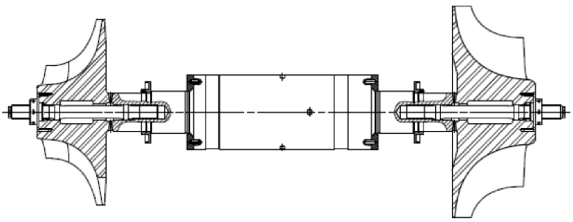

Figure 4.4: Turboexpander presented in the work of Schmied et al. [17].

bearing parameters referred to the test case are reported in Table 4.2. These, have been adopted for the validation of SNAPSHOT.

Bearing characteristics	
Shaft diameter $[mm]$	90
Axial length $[mm]$	117
Pad arc $[deg]$	52
Pivot offset $[-]$	0.5
Preload $[-]$	0.35
Configuration	LOP
Assembled diametral clearance $[mm]$	0.185
Oil type	$ISO-VG46$
Oil temperature $[\circ C]$	43

Table 4.2: Summary of the bearing characteristics for the turboexpander of Schmied et al. [17].

4.3 Discretization sensitivity analysis and validation

A discretization sensitivity has been performed to both the number of points around the orbit N_{pso} and the tangential discretization of each pad NX. The N_{pso} value has been tested ranging from zero up to 2000 while NX has been doubled each time starting from a value of 50 points along the pad's tangential direction up to 200 points.

4.3.1 B term module

Figure 4.5 shows the B term module ($[^{\circ}C/\mu m]$) as a function of the number of points along the orbit for the three different pads' discretizations. As it is possible to observe, similar results are obtained for each of

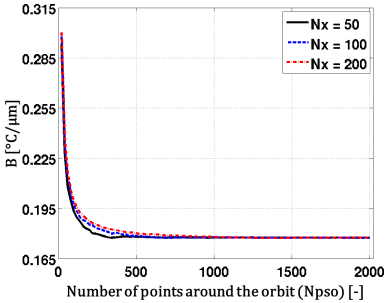

Figure 4.5: Discretization sensitivity analysis: B term module.

the discretizations tested when referring to the number of points along the pads' tangential development (i.e., NX).

On the contrary, the number of points along the orbit (i.e., N_{pso}) has major effects on the obtained results. In fact, Figure 4.5 shows an asymptotic behaviour of the B term module to a value of $0.175^{\circ}C/\mu m$. This value is obtained only when a $N_{pso} \geq 1000$ is adopted. This is quite unexpected, since in the work of Murphy and Lorenz [16], from which the proposed tool has been inspired, a number of 24 points around the orbit is suggested.

The obtained value of B term module of about $0.175°C/\mu m$ is in line, in terms of orders of magnitude, with the one calculated by Murphy and Lorenz [16] which was about $0.13°C/\mu m$.

4.3.2 Phase shift between hot and high spots

In terms of phase shift, shown in Figure 4.6(a) it is possible to observe strong fluctuations for all of the three tested pads discretizations (NX). These fluctuations show a reduction when the number of points along the orbit is increased. Furthermore, as it is possible to observe in Figure 4.6(b), where Gaussian distributions of the phase shift are reported, some differences are highlighted among the pads discretizations in terms of mean value and standard deviation of the phase for low values of N_{pso}. Increasing the number of points along the orbit increases the code inde-

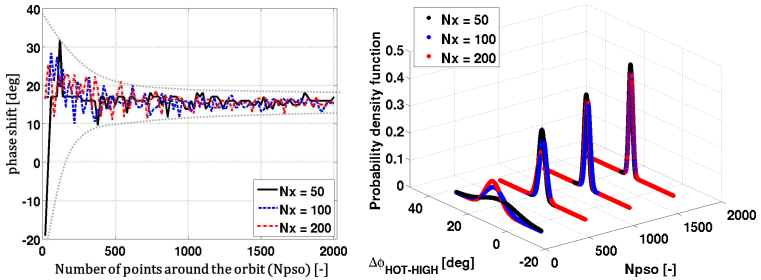

(a) Discretization sensitivity analysis: hot-high spot phase lag.

(b) Probability density function of the hot-high spot phase lag, varyng NX and N_{pso}

Figure 4.6: Effects of the number of points around the orbit N_{pso} on the hot and high spots phase lag.

pendence from the number of elements NX also in case of phase shift calculations. Table 4.3 shows the mean value and standard deviations of a Gaussian distribution based on the number of points along the orbit. The overall population has been considered together with the analysis of four reduced packages of phase data considered every $\Delta N_{pso} = 500$ from 0 to 2000, from which Figure 4.6(b) is obtained. The average phase

shift values evaluated on the overall populations are respectively about $15.5 \leq \mu_\phi \leq 16.3$ $[deg]$. Similar results are obtained also for the proposed subdivisions where maximum and minimum values of the μ_ϕ are respectively 18.5 $[deg]$ and 14.5 $[deg]$. Although the average values are

$N_{pso}/10^3$	overall	$0-0.5$	$0.5-1$	$1-1.5$	$1.5-2$
μ_ϕ $[deg]$ $(NX=50)$	15.547	14.697	15.971	15.802	15.717
σ_ϕ $[deg]$ $(NX=50)$	4.4174	8.6472	1.5475	1.1601	0.96947
μ_ϕ $[deg]$ $(NX=100)$	15.826	17.6	15.305	14.968	15.432
σ_ϕ $[deg]$ $(NX=100)$	2.8409	4.8024	1.7648	1.2534	1.0274
μ_ϕ $[deg]$ $(NX=200)$	16.305	18.509	15.972	15.322	15.417
σ_ϕ $[deg]$ $(NX=200)$	2.6703	3.8804	2.1917	1.2226	1.0282

Table 4.3: Discretization sensitivity analysis: average values and standard deviations of phase shift hot-high spot considering a Gaussian distribution.

close each other, the standard deviations has shown a strong reduction increasing the N_{pso} value. For the range $0-500$ the standard deviation reduces from $\sigma_\phi = 8.6$ $[deg]$ to $\sigma_\phi = 3.9$ $[deg]$ by means of increase in the pads discretization NX. Instead, for the range $1500-2000$ the standard deviation ranges between $\sigma_\phi = 0.97$ $[deg]$ and $\sigma_\phi = 1.03$ $[deg]$ confirming the independence from NX at higher N_{pso} values.

In order to reduce the maximum value of $\sigma_\phi = 8.6$ $[deg]$, which can drive the code towards $\phi = \mu_\phi \pm 3\sigma_{phi}$ $[deg]$, a higher number of points is selected. For the applications of the code in terms of Morton effect prediction a value of $NX = 50$ and $N_{pso} = 1800$ has been adopted. The same values have been also considered for the present validation.

The obtained average phase shift is about 15.7$[deg]$, with high spot lagging the hot spot. This results are in line with literature values, as analysed in Chapter 1.

Figures 4.7(a) and 4.7(b) show the film-thickness and temperature effectiveness (defined in equations 4.3 and 4.4) for respectively $N_{pso} = 36$ and $N_{pso} = 720$. Results, show the source of the phase shift oscillating distribution. In fact, low value of N_{pso} gives a signal which is affected by higher frequency fluctuations. As a consequence, it is not easy to clearly

locate maximum and minimum points.

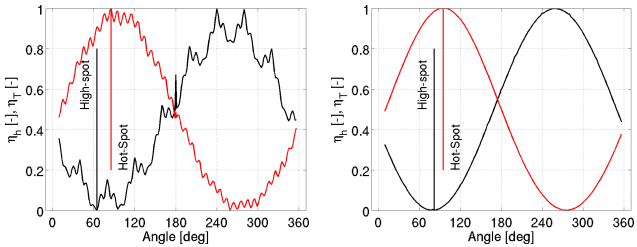

(a) Results of a case with 36 points around the orbit

(b) Results of case with 720 points around the orbit

Figure 4.7: Effects of the number of points around the orbit N_{pso} on the shape of temperature and film thickness effectiveness.

$$\eta_h = \frac{h - h_{min}}{h_{max} - h_{min}} \tag{4.3}$$

$$\eta_T = \frac{T - T_{min}}{T_{max} - T_{min}} \tag{4.4}$$

It is necessary to underline that the hot spot position along the shaft, due to the proposed approach (i.e., obtained by means of averaging the results coming from steady calculations), is more related to geometrical features of both bearing and orbit than to the unsteady flow effects related to the precession motion. However, since results are plausible, the code has been adopted for the phase calculation of the B term and a high number of points along the orbit has been selected in order to reduce the variability of the results.

4.3.3 Calculation time comparison

The discretization sensitivity analysis has proved that is not necessary to increase the number of points along the pads, which has a minor effect, while instead it is necessary to increase the number of points along the orbit.

This solution can have an impact on the calculation time, which is

proposed in Figure 4.8 as a function of N_{pso} for the three NX cases. The non-dimensional time is evaluated with respect to a reference time t_{ref}.

Since the code has been developed with the final objective of predicting the Morton effect, its final application will be coupled to other solvers (necessary to solve the other terms of the physics referred to as A and C). The reference time has been considered from the ANSYS apdl code which has been adopted in Chapter 6 to solve both the rotordynamic problem and the thermo-structural one.

Although the increased number of points, SNAPSHOT remains efficient due to its high calculation speed. In fact, as it is possible to observe in Figure 4.8, for the discretization values selected ($NX = 50$ and $N_{pso} = 1800$), the time for a SNAPSHOT iteration is 1/4 of the time of reference. In particular, one single differential temperature calculation for and imposed orbit at a specific rotational speed, takes about 13 seconds with the selected level of discretization.

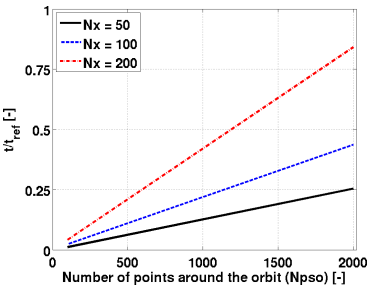

Figure 4.8: Discretization effects on the calculation time.

In order to compare the obtained results with the calculation time of more accurate models, the work of Childs and Saha [34] is considered. In their work, the time needed for the calculation of the differential temperature across the shaft for an orbit is presented. Their accurate numerical models, presented in the work of Gadangi et al. [89], need six to eight hours for a differential temperature calculation with respect to a specific orbit at a specific rotor running speed.

Chapter 5

Uncertainty quantification in hydrodynamic bearings

Contents

The objective of the present chapter is to focus on the uncertainties affecting the system. A methodology is developed in order to study the propagation of the uncertainties within the numerical analysis of hydrodynamic bearings with the aim to quantify the effects of the "lack of knowledge" at the input of the numerical code on some key parameter related to the Morton effect (e.g., the equilibrium position and the dynamic

coefficients).

5.1 Introduction to uncertainty quantification

According to the work of Oberkampf et al. [90], where a framework for identifying the errors and uncertainties in modelling and computational simulations is presented, the general phases related to the process of modelling and simulation can be summarized as follows:

1. conceptual modelling of the physical system
2. mathematical modelling of the conceptual model
3. discretization and algorithm selection for the mathematical model
4. computer programming of the discrete model
5. numerical solution of the computer program
6. representation of the numerical solution

Each one of the presented phases can be source of errors or uncertainties, as also suggested in the work of Roy and Oberkampf [91], and hence, if a reliable simulation is needed, it is necessary to identify the various sources and to include the non-deterministic features related to the system and to the environment.

In the previously cited works [90] [91] a clear distinction between errors and uncertainties is presented. An error is defined as "a recognizable deficiency in any phase or activity of the modelling and simulation that is not due to lack of knowledge". It means errors can be identified upon examination. Moreover, errors can be further classified as:

- Aknowledged: errors that can be identified, reduced or removed and that are known and controlled by the operator (e.g., round-off errors and discretization errors);
- Unaknowledged: errors that cannot be found and removed from the code (e.g., improper use of the code or computer programming bugs)

Uncertainty instead is defined as "a potential deficiency in any phase or activity of the modelling process that is due to the lack of knowledge". Once again it is possible to further classify the uncertainties in two subcategories:

- Aleatory: such an uncertainty is irreducible since it is directly related to the variability within the system or its environment (e.g., manufacturing tolerances, material properties, initial and boundary conditions and so on);

- Epistemic: such an uncertainty is reducible and is connected to the lack of knowledge of the physical problem (e.g., turbulence models, correlations or assumptions such as steady state condition or periodic behaviour of the system)

The introduction of the uncertainty in the simulations does not alter the steps of the process of modelling and simulation of a physical problem but adds some difficulty in each phase and raise the need for some choices and operations to be done in parallel with the steps of the deterministic approach.

In particular three steps are needed in the uncertainty study: the definition, the propagation and the certification of the uncertainty. The first step consists in the identification and choice of the inputs affected by uncertainty and, consequently, the definition of their probability density functions. Various stochastic inputs can be considered, from operating conditions, as adopted in the work of D'Ammaro and Montomoli [92], to geometrical features, as considered in the work of Montomoli et al. [93]. The second step consists in the propagation of the defined uncertainty within the numerical solver in order to identify the probability distribution of some dependent variables of interest at its outlet. Once the quantities have been statistically evaluated it is possible to use them in reliability assessment or in a validation procedure.

5.2 Uncertainty quantification methods

Various methods are proposed in literature in order to approach the uncertainty quantification (UQ). An aware selection of the best suited method can be obtained only after a study of their main characteristics and implications. A well organized review, to be adopted for the purpose, is presented in the work of Montomoli et al. [94].

There are mainly three categories of UQ techniques: sampling based methods, quadrature techniques and intrusive techniques. The first methods are computationally expensive but easy to be implemented and non intrusive, in the sense that it is not necessary to modify the numerical solver. Moreover, by means of improved sampling strategies (e.g., lattice based or latin hypercube samplings) it is possible to sensibly cut the computational cost. The second methods are mainly based on polynomial chaos representation of the stochastic output. By means of quadrature formulas with orthogonal polynomials it is possible to obtain fast and accurate UQ analysis. Finally, intrusive techniques results to be accurate and fast to convergence but require a lot of work to modify the numerical models.

5.2.1 Monte Carlo with response surface

Due to the characteristics of the numerical code considered for the UQ analysis (TILTPAD), the Monte Carlo method has been selected among the presented approaches. Inspired by the work of Montomoli et al. [95], response surfaces have been considered for having a less computationally expensive methodology. Figure 5.1 shows the schematic of the classic Monte Carlo method and of the Monte Carlo with response surface. In the first case, shown on top of Figure 5.1, the random generation of the input conditions is obtained with the defined probability density function. Then, a simulation is performed for each of the generated points in order to find the statistical distribution at the outlet of the system for the dependent variables of interest. The second method instead rely on a two phases approach: simulations are previously performed, covering the

whole design space and defining the response surface, then, the Monte Carlo method is used over this metamodel.

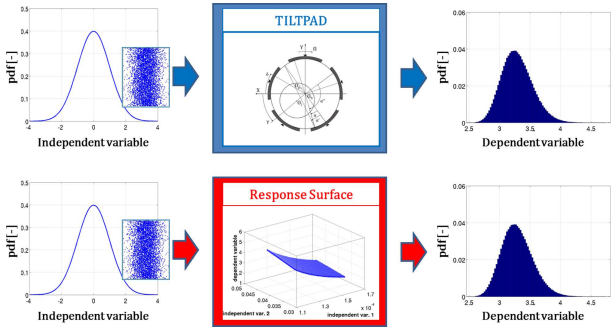

Figure 5.1: Schematic of the Monte Carlo approach with the response surface.

5.3 Uncertainty definition

When hydrodynamic bearings are considered it is immediately possible to imagine a strong sensitivity of the problem to the uncertainties due to the very small length scales of the system. However, although such an expectation is highlighted, no works have been found in literature about the uncertainty quantification applied to the numerical modelling of these components. Usually, in fact, uncertainties are only related to the evaluation of the accuracy of the experimental measurements, at least in author knowledge. For example, a comprehensive and chronological survey about the identification of dynamic parameters in bearings is proposed in the work of Tiwari et al. [96] where is underlined that nowadays many authors recognize the relevance of including accuracy estimations on the measured dynamic coefficients.

Among the various parameters having a role in the numerical modelling of the thermo-hydrodynamic problem two are considered for the purpose of the work and are summarized in the following:

- the radial clearance of the bearing: this parameter results to be highly affected by manufacturing tolerances and respectively by thermal, elastic and wear effects;
- the dynamic viscosity of the oil: this parameter results to be affected by the tolerances of the viscosity grade adopted to classify the oil, by the temperature and weakly by the pressure.

It has to be noted that the dependence of both the variables on the temperature has to be considered in a wider sense with respect to what is usually done. In fact, the temperature uncertainty can be related to the operating conditions of the oil, to the average ambient temperature of the field where the machine is installed and, as highlighted in the work of De Jongh and Van Der Hoeven [18], to the temperature of the fluid processed by the machine.

A preliminary analysis is here presented considering the effects of the manufacturing tolerances on the radial bearing clearance (assembled bearing clearance) and of the tolerances adopted for the characterization of the viscosity grade of the oil. The test case adopted for the analysis is the one presented in Chapter 3, Section 3.12.8.

5.3.1 Clearance manufacturing tolerances

The ISO tolerance system is considered for the purpose. Considering the nominal diameter of the hole, the nominal bearing clearance and the tolerances for shaft and holes, which are respectively adopted as $h6$ and $H6/7$ (data are referred to the catalogues available online of the main bearing producers), the tolerance range can be calculated. According to the tested bearing data the radial clearance range is as follows:

$$C_b = 125^{+32.5}_{-0}[\mu m] \tag{5.1}$$

This result is obtained considering the $H7$ tolerance for the hole in order to test the worst case scenario.

It has to be noted that the nominal clearance results to be the lower bound of the available range of assembled bearing clearance. This is

usually overcome since the industrial practice rely on some adjustment of the clearance when the system is assembled. Anyway, this practice has a cost and in certain cases it is not applied. Hence, for the present work the adjustment is not considered and results will be remarkably affected by the choice of having a nominal clearance at the extreme of the tolerance range. Again, the choice is motivated by the aim to reproduce the worst case scenario.

The probability density function of the tolerances is the main assumption of the work since there are no direct information about its realistic distribution. In particular, a normal distribution centred within the tolerance range is adopted resulting in a mean value of 141.25 μm. For the standard deviation a value of 5.4 μm (i.e., a 3.8% of the mean value) is selected in order to obtain the extremes of the tolerance range respectively at $\pm 3\sigma$. By means of such a choice, some of the tested values (the 0.3% of the tested points) result to be slightly outside of the tolerance domain.

5.3.2 Feeding oil viscosity grade

The mineral oil adopted for the lubrication process is usually selected on the base of the viscosity grade (ISOVG). The proposed classification is based on the mean value of the kinematic viscosity (e.g., ISOVG-32 has a mean kinematic viscosity value at 40 $^{\circ}C$ of 32 mm^2/s).

The oil adopted for the present analysis is an ISOVG-46 with a value of density of about 870 kg/m^3. According to the oil classification, the selected oil can have a kinematic viscosity between the range $41.4 \div 50.6$ mm^2/s and hence its dynamic viscosity range (used by the code) is within the range of $0.036 \div 0.044$ Pas.

Again, as done for the radial clearance, a normal distribution is considered with the mean value centred (0.040 Pas) and with a standard deviation of $\sigma = 0.0013$ Pas (i.e., a 3.3% of the mean value) . The selection of the standard deviation imply again that the extremes of the tolerance range result exactly positioned at $\pm 3\sigma$.

5.4 Generation of the response surface

Figure 5.2 reports the response surfaces adopted for the present analysis. A test matrix has been performed in order to cover the entire surface determined by the two parameters variation. The field of simulation has been extended up to $\pm 4\sigma$ for each one of the parameters and has been covered by means of 41 testing points, resulting in 1681 simulations (accomplished in about 16 hours). The obtained surfaces gives the

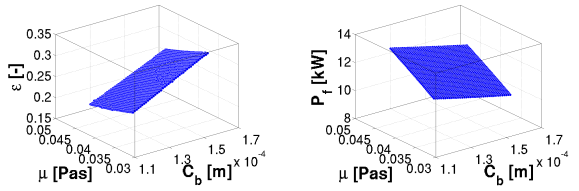

(a) Eccentricity ratio

(b) Frictional power losses

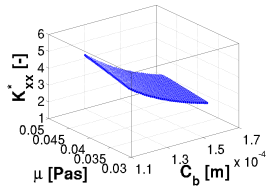

(c) Spring coefficient (x-direction)

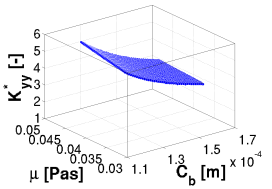

(d) Spring coefficient (y-direction)

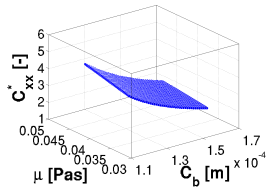

(e) Damping coefficient (x-direction)

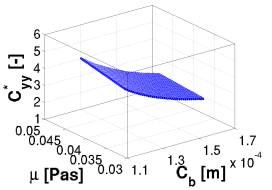

(f) Damping coefficient (y-direction)

Figure 5.2: Response surface from TILTPAD, adopted for the Monte Carlo approach.

response of the code in terms of eccentricity ratio, frictional power losses and non-dimensional dynamic coefficients with respect to the clearance and dynamic viscosity variations.

5.5 Application of the Monte Carlo method

Once the response surfaces are given for the parameters of interest, the Monte Carlo method is applied. This has been accomplished generating one million of random pairs of clearance and dynamic viscosity values, each one following its own normal distribution (hypothesized in the previous section), and then adopting the response surface to obtain the dependent results, which are statistically analysed in the following.

The effects of the uncertainty of the two parameters of interest have been evaluated for the selected dependent variables considering a simultaneous variation of the two parameters. Then, each single parameter is individually studied by means of the same approach with the objective, in this case, to evaluate their own weight.

Referring to the synchronous thermal instability, this kind of analysis should be of great interest since it quantifies the effects of the uncertainties, which necessarily affect the system, on some of the driving parameter of the Morton effects (e.g., the dynamic coefficients). Particular attention has to be given to such a topic for all of the machines which lie between the marginally stable (borderline) condition. In fact, for this particular condition the smallest change can result in an unstable rotor system.

5.5.1 Simultaneous variation

In terms of eccentricity ratio and frictional power losses, shown in Figure 5.3, a normal distribution is obtained with mean values respectively of about 0.250 and 11.6 kW and with standard deviations of about 4.7% and 2.7%. Such a behaviour (normal distribution) could be expected since the response surface of relative eccentricity and frictional power losses resulted to be characterized by almost linear relations with respect to the independent variables (as shown in Figures 5.2(a) and 5.2(b)).

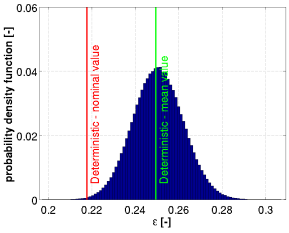

(a) Eccentricity ratio

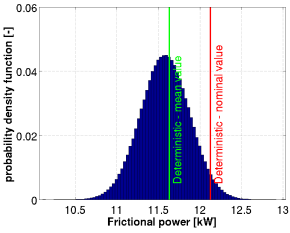

(b) Frictional power losses

Figure 5.3: Results of the Monte Carlo approach with response surface.

About the non-dimensional dynamic coefficient, whose distributions are shown in Figure 5.4, a kind of normal distribution is again obtained, although in this case a slight non-symmetry is highlighted. The observed

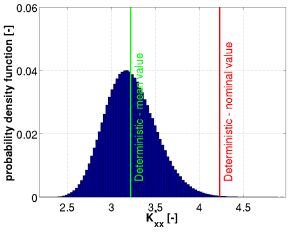

(a) Spring coefficient (x-direction)

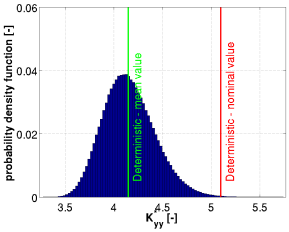

(b) Spring coefficient (y-direction)

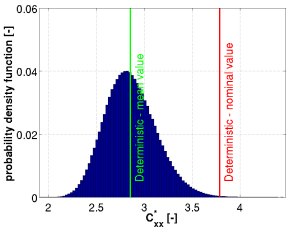

(c) Damping coefficient (x-direction)

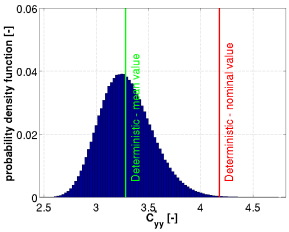

(d) Damping coefficient (y-direction)

Figure 5.4: Results of the Monte Carlo approach with response surface.

asymmetry has been confirmed evaluating the probability to obtain a result within a reference range, respectively positioned below and above the maximum probability value. The selected reference range has an extension of a 10% of the maximum probability value. Results, summarized in Table 5.1, confirm the slight non-symmetrical behaviour of the outlet distributions. The maximum difference between the two tested ranges below and above the maximum probability value is obtained for the non-dimensional direct spring coefficient (evaluated with respect to the y-axis), where a 6% difference is highlighted.

output	Range -10%	Range $+10\%$
K^*_{xx}	36.6%	38%
K^*_{yy}	41.1%	47.2%
C^*_{xx}	36.7%	38%
C^*_{yy}	39%	42%

Table 5.1: Probability distribution analysis: probability to obtain a value within the range of -10% and $+10\%$ with respect to the maximum probability value.

For all of the analysed variables, shown in Figures 5.3 and 5.4, the values of the deterministic calculations performed with the nominal and with the mean values of the clearance have been reported by means of respectively a red and a green line. The choice not to consider the adjustment of the clearance and hence consider the nominal clearance as a lower bound, drives a substantial difference between the results of the deterministic calculation obtained with the nominal value and the maximum probability value obtained with the uncertainty quantification analysis. The maximum difference is found for the non-dimensional damping coefficient in the x-axis direction where an over-prediction of about 25.5% of the deterministic value with respect to the most probable one is highlighted.

For sake of clarity, Table 5.2 summarizes the values related to the two deterministic calculations (nominal and mean) and to the maximum probability value of the obtained distributions. In case the mean value is

adopted for the deterministic calculation discrepancies are drastically reduced and a maximum difference of about 1.2%, evaluated with respect to the deterministic mean value, is obtained for the non-dimensional spring coefficient.

output	deter. mean	deter. nominal	max. probability
ϵ [−]	0.250	0.219	0.249
K^*_{xx} [−]	3.22	4.21	3.18
K^*_{yy} [−]	4.15	5.10	4.10
C^*_{xx} [−]	2.85	3.79	2.82
C^*_{yy} [−]	3.28	4.18	3.24
P_f [kW]	11.6	12.1	11.6

Table 5.2: Calculation results: deterministic calculation with mean clearance value, deterministic calculation with nominal clearance value and maximum probability value obtained with the uncertainty analysis.

If results of the dynamic coefficients are considered as normal distributions, it is possible to evaluate both the mean value and the standard deviation for each coefficient, shown in Table 5.3. Due to the imposed approximation, the values obtained as a mean value are slightly different from the maximum probability values obtained. The maximum value of the standard deviation is obtained for the damping coefficient with respect to the x-direction with a value of 9.4%.

	mean value μ [−]	standard deviation σ [%]
K^*_{xx}	3.23	9.0%
K^*_{yy}	4.17	6.4%
C^*_{xx}	2.87	9.4%
C^*_{yy}	3.30	7.7%

Table 5.3: Probability distribution analysis: mean value and standard deviation of the non-dimensional dynamic coefficients.

5.5.2 Individual variation

Considering first the case with uncertainty affecting the viscosity of the oil and with a constant value of the assembled bearing clearance (i.e.,

125 μm) a normal distribution, at least in a first approximation, has been obtained for all of the evaluated variables. Hence, results, expressed in terms of mean value and standard deviation, are proposed in Table 5.4.

	mean value μ	standard deviation σ [%]
ϵ [−]	0.218	1.8%
K^*_{xx} [−]	4.22	2.1%
K^*_{yy} [−]	5.10	1.2%
C^*_{xx} [−]	3.79	2.1%
C^*_{yy} [−]	4.18	1.6%
P_f [kW]	12.1	2.2%

Table 5.4: Probability distribution analysis: mean value and standard deviation (viscosity variation).

According to the proposed results it is possible to notice a decrease in the sensitivity of the dependent variables to the viscosity variations with respect to the results shown in the previous paragraph. A strong reduction of the standard deviation, of about 2% in this case, is in fact highlighted with respect to the results of the combined action of both viscosity and clearance which resulted in a maximum standard deviation of about 9.4%. Moreover, it is possible to highlight that the uncertainty related to the dynamic viscosity mainly affects the frictional power losses with a 2.2% of standard deviation.

When the case with uncertainty affecting the bearing clearance only is considered, distributions similar to the ones shown in Figures 5.3, 5.4 are obtained. Considering as a first approximation kind of normal distributions, as done in the case of simultaneous variations, the corresponding mean values and standard deviations are evaluated. Results of this latter analysis are reported in Table 5.5.

As it is possible to observe the obtained mean values and standard deviations are similar to the ones related to the simultaneous effect of viscosity and clearance, with a maximum of standard deviation obtained for the damping coefficient in the x-direction of about 9.1%. A reduction of the standard deviation of the frictional power losses is obtained (from a 2.7% to 1.4%) since this variable is more sensitive to the viscosity with

	mean value μ	standard deviation σ [%]
ϵ [−]	0.249	4.3%
K^*_{xx} [−]	3.23	8.8%
K^*_{yy} [−]	4.16	6.3%
C^*_{xx} [−]	2.87	9.1%
C^*_{yy} [−]	3.30	7.6%
P_f [kW]	11.6	1.4%

Table 5.5: Probability distribution analysis: mean value and standard deviation (clearance variation).

respect than the clearance.

According to the proposed analysis the dynamic coefficients result to be particularly affected by the uncertainty of the system. In particular a strong sensitivity to the clearance is highlighted.

Although it is possible to adjust the clearance and hence reduce the main source of uncertainty with respect to the manufacturing tolerances it has to be reminded that some other phenomena can drive to clearance variations, e.g., the thermal behaviour of the system and elastic deformations. In particular, the thermal behaviour may have a major role. In fact, as introduced in the work of De Jongh and Van Der Hoeven [18] a variation in the bearing clearance can be obtained due to the temperature of the gas evolving inside of the machine. For example in the cited case a strong reduction was obtained due to the particular field of operation (cryogenic applications) and due to some specific geometrical features.

Some other cases can be found in literature showing the effects of the thermal behaviour of the system. For example, in the work of Ferron et al. [44] two clearance values are reported: the first one is related to a temperature of 20 $^\circ C$ and is of about 145 μm, the second one is related to a temperature of 45 $^\circ C$ and is of about 152 μm with a variation of about 4.8% with respect to the "cold" value. Hence, since the adjustment is done while the system is assembled (cold condition), when operated (hot condition), the clearance can assume sensibly different values.

Part II

Synchronous Thermal Instability: Prediction and Analysis

Chapter 6

Morton effect prediction and control

Contents

The models developed for the thermo-hydrodynamic analysis of PJBs and TPJBs, presented in the previous chapters, have been finally considered in order to predict the onset of the Morton effect. This has been accomplished following the two strategies presented in Chapter 2: the

linear stability analysis and the iterative approach. Results from both the selected strategies are compared with data obtained by means of a dedicated experimental campaign reported in the work of Panara et al. [10].

6.1 Experimental Campaign

The dedicated experimental test campaign, which is adopted as a validation reference for the prediction of the onset of the Morton effect, has been carried out at the GE Oil & Gas facility in Florence on a real scale between bearing dummy rotor. Since the campaign is not part of the thesis work, and since details of the experimental apparatus have been given in the work of Panara et al. [10], only some of its main characteristics are here reported.

The dummy rotor, driven by an electric motor and shown in Figure 6.1, is representative of a full scale compressor shaft and is supported by two direct lubricated tilting pad journal bearings. The five pads bearings adopted for the purpose are mounted in a load on pad (LOP) configuration. In order to allow differential temperature measurements at the

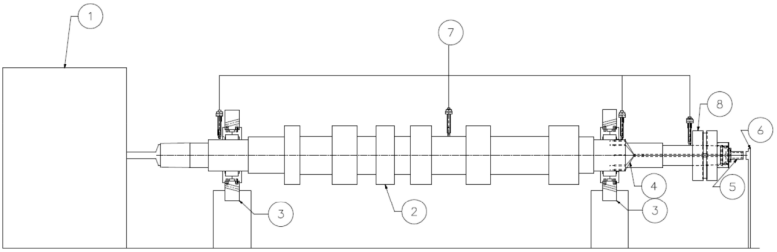

Figure 6.1: Sketch of the experimental apparatus, from the work of Panara et al. [10].

non-drive end bearing section of the shaft, a set of eight K thermocouples equally spaced among the 360 degrees were installed a few millimeters below the shaft surface by means of axially drilled holes.

Bearing temperatures has also been monitored through $Pt100$ thermo-resistances both on drive and non-drive end bearings. In particular the most loaded pad (it is a LOP configuration) is equipped with two temperature probes respectively at 25% and 75% of the pad arc. Another temperature probe is mounted on the downstream pad at 75% of the pad arc.

Shaft vibrations are monitored in four different position along the shaft by means of Bently Nevada non-contact probes attached to the *ADRE* system. The monitored sections are: the bearing sections, both drive and non-drive ends, rotor mid span and shaft end at the non-drive side.

The rotor is designed in order to have a predominant overhung at the non-drive end side with respect to the drive end one. The objective is to enhance the effects of the thermal bow coming from the instrumented bearing section. Three configurations have been tested varying the overhung non-drive end weight which are respectively referred to as $W1$, $W2$ and $W3$. $W1$ is the maximum overhung configuration while moving through configuration $W3$ the overhung is reduced. Values are presented in terms of equivalent overhung and rotor weight ratio with respectively 12.4%, 8.40% and 7.30% for the $W1$, $W2$ and $W3$ configurations.

Results are shown in Figures 6.2, 6.3, 6.4 for the three tested cases. For each configuration the tested rotational speed have been highlighted in red. Different thresholds of instability have been found depending on the idling weight. Results are analysed hereinafter starting from the $W3$ configuration which is the minimum overhung weight (no idling) up to the $W1$ which has the heaviest idling adaptor.

The $W3$ configuration, shown in Figure 6.2, has been held in rotation at the following speed: 8200, 9200, 10200, 12600 and 13600 rpm for 5 minutes each. The rotor has shown instability at 13600 rpm. The vibrations level grew from 10 μm to 50 μm within five minutes, forcing a quick decrease in rotational speed. The typical Morton effect hysteresis loop is highlighted. The vibration levels for the other tested velocities

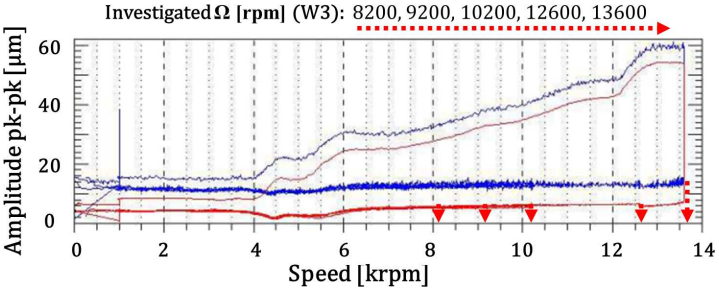

Figure 6.2: Results of the experimental campaign, taken from the work of Panara et al. [10]: W3 case.

resulted to be stable.

The rotor with intermediate overhung weight (small idling), i.e., $W2$ configuration shown in Figure 6.3, has been held in rotation at four different rotational speed: 8200, 10200, 11200 and 11400 rpm. The experimen-

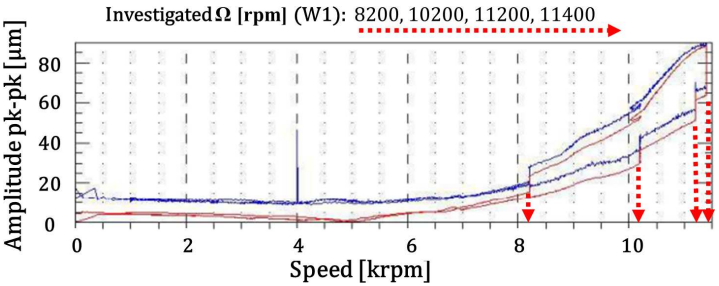

Figure 6.3: Results of the experimental campaign, taken from the work of Panara et al. [10]: W2 case.

tal tests show a stable dynamic behaviour at 8200, 10200 and 11200 rpm. While very weak thermal effects have been shown for the 8200 rpm test, for the two faster speed the vibration increased of about 10 μm $pk-pk$ however resulting in a stable behaviour. Finally, at 11400 rpm the vibration amplitude grew up to 85 μm highlighting the sensitivity of the system to the thermal rotor instability. Yet again hysteretical behaviour

is highlighted.

In Figure 6.4 the amplitude of the displacements for the $W1$ configuration is showed. The investigated velocities, which the rotor is hold in rotation at, are respectively 10600, 11200, 12200 and 13200 *rpm*. The

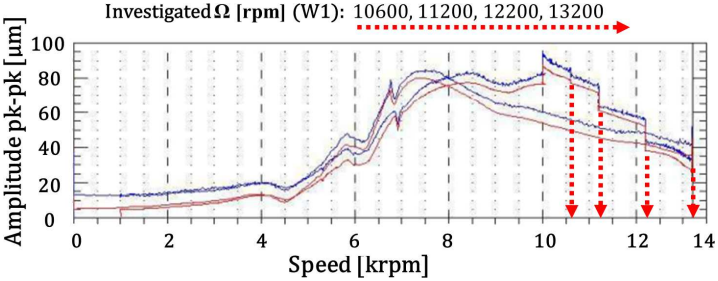

Figure 6.4: Results of the experimental campaign, taken from the work of Panara et al. [10]: W1 case.

vibration levels for this case resulted to be higher then the other showed configurations but no unstable conditions have been detected during the experimental tests.

6.2 Morton effect prediction: linear stability analysis

A commonly used strategy to approach stability problems is to assume that linear relationships could be derived among the fundamental physical quantities governing the phenomena. As described by Murphy and Lorenz [16], complex linear influence matrices can be derived in order to link with each other the rotor vibration ($\overline{V}$), the imbalance ($\overline{U}$) and the rotor thermal gradient ($\overline{T}$) as described in Equations 6.1, 6.2, 6.3.

$$\overline{V} = A\overline{U} \tag{6.1}$$

$$\overline{T}_{ss} = B\overline{V} \tag{6.2}$$

$$\overline{U} = \overline{U}_0 + C\overline{T} \tag{6.3}$$

$\overline{U}_0$, defined in Equation 6.3, is the initial residual imbalance vector while A, B and C are the complex influence matrices that define the system sensitivity to bearing vibration, rotor thermal gradient and thermal imbalance. During the shaft motion, the rotor thermal gradient dynamics can be also expressed in terms of thermal damping and stiffening as in the Equation 6.4, taken from the work of Murphy and Lorenz [16], where D and E are the thermal damping and stiffness complex matrices.

$$D\dot{\overline{T}} + E(\overline{T} - \overline{T}_{ss}) = 0 \tag{6.4}$$

Substituting the vector relations of the influence matrices into Equation 6.4 it is possible to obtain the final form of the system.

$$\tau\dot{\overline{T}} + (1 - BAC)\overline{T} = BA\overline{U}_0 \tag{6.5}$$

where $\tau = E^{-1}D$ is the real non-negative matrix of the thermal time constants of the problem. Equation 6.5 admits solutions in the form reported in the following equation:

$$\overline{T}(t) = \overline{T}e^{st} \tag{6.6}$$

where $s = (\overline{BAC} - 1)/\tau$ is the complex eigenvalue of the system.

In order to have a stable solution, a negative value of the real part of s is required (i.e., $Re(\overline{BAC}) \leq 1$).

The linear stability approach is formulated in the time domain but in order to compute stability just an accurate knowledge of the sensitivity matrices in terms of both amplitudes and phases is needed.

6.2.1 Adopted strategies for the A, B and C terms evaluation

For the purpose of the linear stability method, the complex influence coefficients have to be calculated. The B coefficient is evaluated by means of SNAPSHOT, which has been presented in Chapter 4.

The A term has be numerically estimated from the rotor response to

an overhung imbalance evaluated at the bearing mid-line section. This kind of simulations have been performed by GE Oil & Gas with a standard rotordynamic code.

The C term has been instead calculated by means of an analytical relation presented in Equation 6.7, where R_j, B, λ are respectively the journal radius, the axial length of the bearing and the rotor thermal expansion coefficient and where L_{oh}, l_{oh} are respectively the equivalent overhung weight and the equivalent overhung length.

$$C = L_{oh} \frac{\lambda B l_{oh}}{R_j} \tag{6.7}$$

The phase of C is always considered to be 180 deg with respect to the direction of the rotor thermal gradient.

The Equation 6.7 has been derived starting from the classical theory of the thermal expansion of a shaft subjected to differential temperature. The shaft thermal bending has been evaluated enabling the calculation of the thermal imbalance. This is evaluated by means of the overhung mass and the thermal deflection at the overhung location. The same approach for the C term evaluation has been also considered in the work of Balbahadur [19].

6.2.2 Experimental correlation

Further validation of the methodology has been done using the available experimental data. In order to link the shaft vibration to the rotor differential temperature distribution an experimental correlation has been derived from the results of the dedicated experimental campaign. The obtained relation has been adopted to evaluate the B term enabling the comparison between the experimentally fitted correlation (representative of the experimental data) and the results obtained by means of the present code for the differential temperature estimation.

The relations proposed in Equations 6.8, 6.9 allow to obtain information on the amplitude of the temperature variation ΔT and on its phase ϕ. As a consequence, it is possible to locate the minimum and the max-

imum of the temperature distribution in function of the shaft vibration δ_0 and of the bearing operating conditions (i.e. lubricant minimum film thickness of each pad, spinning frequency of the shaft, inlet viscosity of each pad, density and the specific heat capacity of the lubricant). As it is possible to observe the proposed correlation is based upon two coefficients which need to be tuned. The values adopted in the present work, in fact, have been found by means of the experimental fitting, which has been performed for each of the analysed cases (W3, W2 and W1). The adopted correlation has been implemented by GE Oil & Gas and has been here only fitted on the experimental data, by means of changing K_1 and K_2.

$$\Delta T = f_1(h_{min}, \Omega, R_j, \mu_{in}, \rho, c, B, K_1, K_2) \tag{6.8}$$

$$\phi = f_2(h_{min}, \delta_0, \Omega, R_j, \mu_{in}, \rho, c, B, K_1, K_2) \tag{6.9}$$

In Figure 6.5 the measured values of rotor differential temperature variation in time have been compared with the experimentally fitted data. These latter, have been calculated by means of the measured amplitude vibration trend which are also reported in the presented figures. A very good agreement in all tested configurations (W3, W2 and W1) has been obtained. The proposed time dependent temperature data have been non-dimentionalized with respect to the maximum measured rotor temperature gradient during the acquisition time. During the recorded time the rotor speed was hold at a fixed value.

The operating conditions adopted for the tuning of the experimental correlation are different for each case. In Figure 6.5(a) the data are referring to an unstable condition detected during a dwell at a constant speed of 13600 *rpm* in configuration *W*3 (see Figure 6.2 for detailed information). In Figure 6.5(b) a similar condition is reported for the W2 configuration. In this case the threshold of instability reduces from 13600 to 11400 *rpm*. In Figure 6.5(c) the W1 rotor configuration (higher overhung weight) is reported at 13400 *rpm*. Despite the high rotor speed, the configuration was stable.

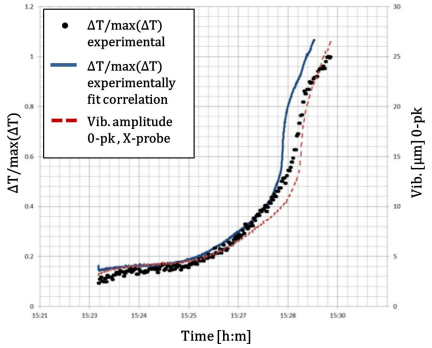

(a) W3-case.

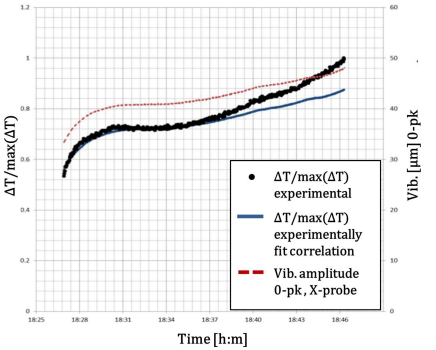

(b) W2-case.

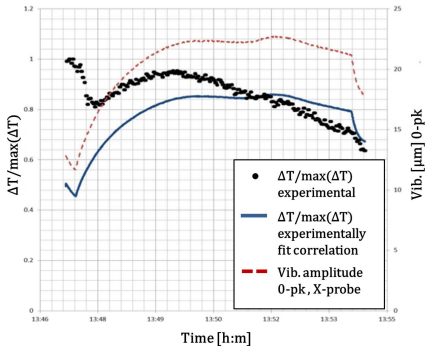

(c) W1-case.

Figure 6.5: Comparison between experimentally fit correlation and experimental data for W3, W2 and W1 cases (from the work of Panara et al. [10]).

6.2.3 Results

The BAC term is calculated as reported in Section 6.2.1 for all of the cases tested in the experimental campaign. The only difference between the proposed results is the evaluation strategy adopted for the B term: "experimentally fitted" data are obtained by means of the fitted correlation, presented in Section 6.2.2, while "present work" data are evaluated by means of the code SNAPSHOT proposed in Chapter 4. This latter, in turn, rely on the journal bearing equilibrium data calculated by the code for the thermo-hydrodynamic analysis of PJBs and TPJBs presented in Chapter 3 (TILTPAD).

Both results of the real component of the BAC term ($Re(BAC)$) and of the module of the BAC term are shown in the following. While $Re(BAC) \leq 1$ is the condition directly derived from the linear stability theory the $|BAC| \leq 1$ can also be adopted due to its conservative nature.

In Figure 6.6(a) the BAC analysis results are shown referring to the W3 configuration. The experimental instability threshold speed, detected at 13600 rpm, is reported as a vertical dashed line. Considering the "present work data", an underestimation of the instability threshold, predicted at around 12400 rpm, is obtained.

The main difference between the "experimentally fit" BAC prediction and the computed one is represented by the estimation of the B phase (ϕ_B), which affects the computation of the $Re(BAC)$ particularly above the instability threshold. In fact, it is important to notice that in both cases the same threshold of instability is predicted.

The phase difference of B can be evaluated looking at Figure 6.6(b) where the ratio of computed and experimentally fit amplitude and phase of B are reported with respect to the rotor speed. As can be seen, for the B amplitude ratio, a convergence towards unity appears at high regimes of rotation, which is in agreement with the Petroff's type hypothesys adopted for the energy equation. Unfortunately, not a similar behaviour is shown for the B ratio whose estimation is far from the experimentally fitted values.

Due to the highlighted difference the experimental fit correlation shows

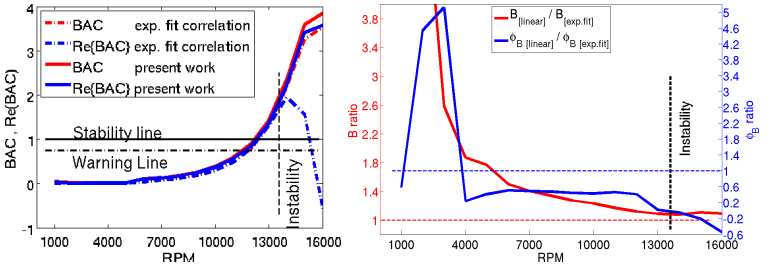

(a) W3-BAC analysis.

(b) W3-comparison snapshot/experimentally fit correlation.

Figure 6.6: Comparison between experimentally fit correlation and SNAPSHOT for W3 case.

a stability recovery at higher rotational speed, at about 15000 *rpm*, due to the phase of the B term. Such a recovery prediction is not instead shown by the model when B is evaluated by means of SNAPSHOT. Unfortunately, speed higher than 13600 *rpm* have not been tested during the experimental campaign and hence it is not possible to draw conclusions about the accuracy of the models.

However, in the work of Panara et al. [10], an iterative model, based on the same experimentally fitted correlation, has been adopted for the evaluation of the present cases. Results agree with the "present work" in the way that the stability recovery is not predicted.

For the overhung configuration W2 the results are shown in Figure 6.7(a). Experimentally it is found a shift of the instability threshold towards reduced speed (from 13600 to 11400 *rpm*). A similar trend is obtained from the linear stability evaluation, with a good prediction of the instability onset obtained by both the models. Again, experimentally fitted model predicts a recover of stability where the model objective of the present work do not. Unfortunately neither for the previous case nor this time speeds above the threshold were tested during the experimental campaign. However, as considered for the W3 case, the iterative model presented in the work of Panara et al. [10], which has also been previously

cited, do not show any recovery.

The differences in the evaluation of the B term for the two models are depicted in Figure 6.7(b). Here, a similar trend to the W3 configuration is shown. The prediction of the module of the B term became closer to the experimentally based correlation at higher rotor speeds. The phase of B, instead, appears to be again the most difficult parameter to be evaluated.

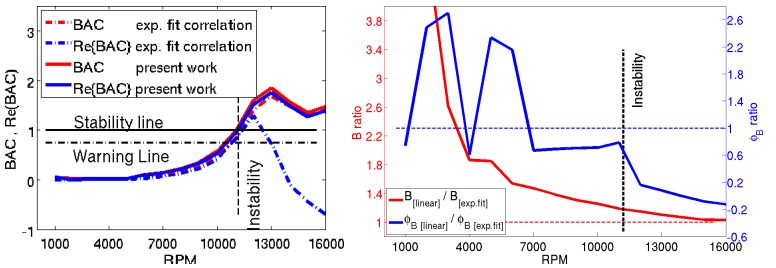

(a) W2-BAC analysis.

(b) W2-comparison snapshot/experimentally fit correlation.

Figure 6.7: Comparison between experimentally fit correlation and SNAPSHOT for W2 case.

For the W1 configuration (see results in Figure 6.8) the stability analysis predicts a marginal instability in the range between 8000 and 10000 rpm and this is the region where a synchronous vibration increase has been experimentally detected (see the experimental bode plots in Figure 6.4). Where both the curves of the BAC module show similar behaviours, a comparison between the $Re(BAC)$ curves gives evidence of discrepancies in the evaluation of B term, particularly of its phase. In this case, as depicted in Figure 6.8(b), the B amplitude ratio show some oscillations around unity at higher rotational speed and the phase ratio results to be far to approach unity in the whole speed range.

Finally, in Figure 6.9 the A term adopted for the presented stability analysis, normalized with respect to the maximum value among the tested cases ($A_{max} \simeq 0.21\ \mu m/g \cdot mm$), is compared for the W1, W2 and W3

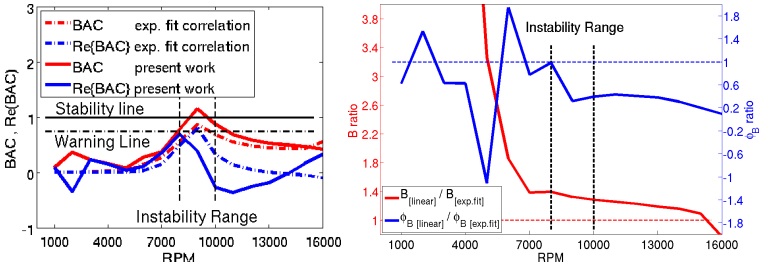

(a) W1-BAC analysis.

(b) W1-comparison snapshot/experimentally fit correlation.

Figure 6.8: Comparison between experimentally fit correlation and SNAPSHOT for W1 case.

rotor configurations. A reduction of the A term is shown from the W3 to the W1 case, with a shift towards lower rotational speed of its maximum values.

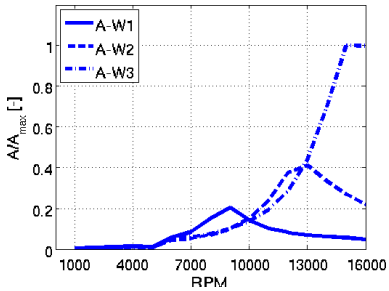

Figure 6.9: Normalized values of the A term for the three tested cases W3, W2 and W1.

The C term was instead respectively computed as 335, 193 and 144 $g \cdot mm/°C$.

Based on the shown results, it can be concluded that the linear stability approach can provide quite accurate prediction of the development of the thermal instability although some discrepancies are highlighted (e.g., the instability threshold of the W3 case is mispredicted of about 1200

rpm). However, the implemented methodology results to be fast and quite reliable in predicting if the Morton effect is expected or not for the analysed system. Furthermore, although SNAPSHOT provides different values for the phase of B term with respect to the experimentally fitted data, results in terms of global stability of the system are similar for both cases. As a consequence, since SNAPSHOT do not rely on a tuning of the parameters based on an experimental campaign, the proposed tool can be reasonably considered for the forecast of the Morton effect.

6.3 Morton effect prediction: iterative method

The iterative model is developed in collaboration with the MDMlab of the Department of Industrial Engineering of the University of Florence, which developed the rotordynamic models. These, have been adopted for the harmonic analysis (both uncoupled and thermally affected) and the thermo-structural analysis for the evaluation of the shaft bending.

6.3.1 Description of the general architecture

The general architecture of the iterative method, proposed to capture the thermal instability onset, is shown in Figure 6.10. The procedure shown is related to a single shaft rotational speed and hence the whole scheme has to be repeated for each condition tested in terms of static load, residual mechanical unbalance and rotor spinning speed. In particular, before the iterative loop begins the code for the thermo-hydrodynamic analysis TILTPAD, presented in Chapter 3, is used to find static and dynamic characteristics of the journal bearings. The dynamic coefficient are then given to what is called "dynamics module" in order to perform the preliminary harmonic analysis and find the "uncoupled" orbit motion related to the residual mechanical unbalance. Instead, the equilibrium position of the shaft (ϵ,γ) and the tilt angle of each pad (θ_i) are given to SNAPSHOT.

The iterative loop is highlighted in red in Figure 6.10. It is based on two calculations. The first one is performed by the code for the evalu-

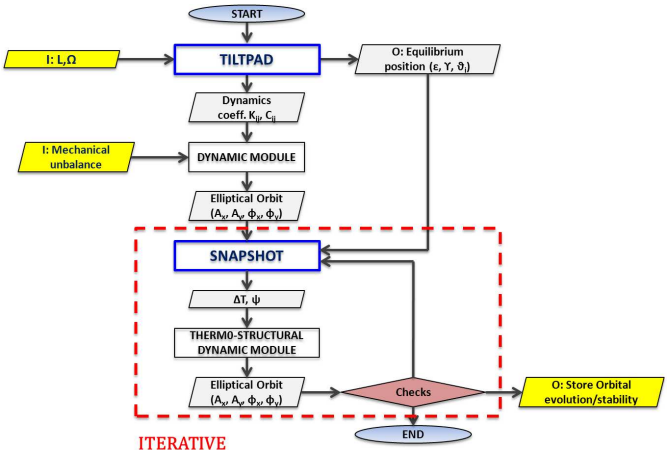

Figure 6.10: Scheme of the iterative architecture (TILTPAD and SNAPSHOT contributions are highlighted in blue).

ation of the differential temperature developed across the shaft (SNAPSHOT) on the base of the previously cited equilibrium positions and on the amplitude (A_x,A_y) and phase (Φ_x,Φ_y) of the vibration displacements (both in X and Y directions). The result of SNAPSHOT, composed of module and phase of the differential temperature, is given to the thermo-structural dynamic module which evaluate the thermal deflection of the shaft and perform a novel harmonic analysis. Results of this latter are again adopted as input condition of the SNAPSHOT code. The procedure is iterated until the loop drives the system towards a steady state condition, in terms of vibration orbit and differential temperature, or until divergence is obtained.

In the dynamics module the rotordynamic behaviour of the system is analysed. In particular, the rotor, spinning around its revolution axis with angular velocity Ω, is subjected to synchronous known unbalance $\overline{U}_0$. The resulting movement, due to the centrifugal effects and calculated through the first harmonic analysis, here referred to as "uncoupled", is generally an elliptical orbit around the rotor stable equilibrium position,

which can be decomposed in two harmonic displacements along the vertical and transversal directions, each one characterized by an amplitude and a phase angle. The results of the analysis are the displacements of the node located at the Non Drive-End side (NDE).

Another analysis dedicated to the rotor is the thermo-structural analysis. By means of this latter, it is possible to calculate the equivalent unbalance, representing the centrifugal effects due to the shaft displacements from its initial position caused by the thermal bending. The equivalent unbalance is added to the initial one (residual mechanical unbalance) in order to calculate the new rotor orbit and then the new displacements at the NDE bearing.

The rotor model, whose details and validation results are presented in the work of Panara et al. [10], includes both the shaft FEM model and the bearing, represented as lumped parameters. The shaft FEM model is discretized through BEAM elements, composed of two nodes with six degree of freedom per node, and a 3D solid element, which is used to mesh the part of the rotor where the NDE bearing is located (i.e., where the thermal gradient apply). The bearing elements act as spring and damper elements whose damping and stiffness matrices, depending on the analysed angular velocity Ω, are calculated through TILTPAD.

6.3.2 Results

The results of the iterative model for all of the tested cases (W3,W2 and W1) are presented as maps of vibration amplitude and differential temperature evolutions. The tested rotational speed, increasing along the y-axis of the plots, range from 8000 *rpm* to 20000 *rpm* with a step change of 200 *rpm* for the W3 and W2 cases, while the W1 case starts from a value of 6000 *rpm* due to its critical behaviour at lower rotational speed. The number of iterations of the model compose the the x-axis of the plot and represents the "evolution in time" of the system according to the pseudo-unsteady approach. Both temperature and vibration amplitudes are shown through a color map (the calculated displacement amplitudes are limited to the assembled bearing clearance as a maximum value).

W3 case

Figure 6.11 shows the results of the W3 case with its experimental instability threshold highlighted by means of a white dashed line at 13600 *rpm*. The model is able to predict the instability onset with quite good

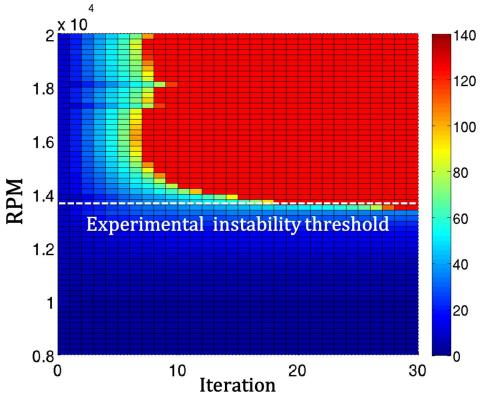

Figure 6.11: Results of the iterative model for the W3 case: vibration amplitude map.

agreement, in fact, only a slight under-prediction is obtained, with divergence detected at 13400 *rpm*. For all of the lower rotational speed tested, a stable condition is obtained although with increased amplitude with respect to the uncoupled case. Finally, no recovery of stability is shown for rotational speed values higher than the threshold.

A detail of the orbits evolution during the iterative process is presented in Figure 6.12. Orbits are reported for each iteration starting from the uncoupled condition, that is the first harmonic analysis without thermal effects, to the stable or diverged conditions, this latter highlighted in red. As it is possible to observe, the 13200 *rpm* case results in a stable orbit motion with an amplitude $0-pk$ of about 35.5 μm while the 13400 *rpm* one diverges until the contact with the pads occurs, defining the instability threshold.

Figure 6.13 show differential temperature results in terms of color

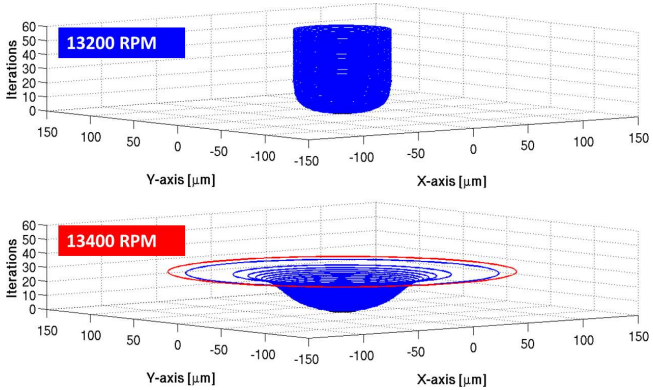

Figure 6.12: Details of the quasi-unsteady orbits evolution obtained from the iterative model: 13200 and 13400 *rpm*.

map as done for the amplitude in Figure 6.11, and in terms of differential temperature with respect to the vibration amplitude. This latter is shown in Figure 6.13(b) for a rotational speed below the instability threshold, at 13000 *rpm*, and above the threshold, at 13800 *rpm*.

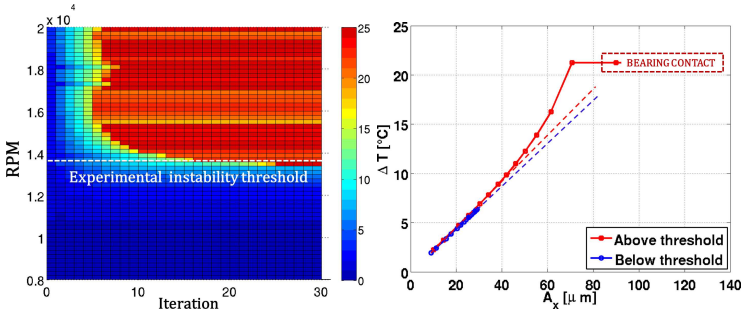

(a) W3-module of the shaft differential temperature.

(b) W3-differential temperature evolution: above and below instability threshold.

Figure 6.13: Results of the iterative model for the W3 case: differential temperature.

Temperature plot of Figure 6.13(a) results to be very similar to the vibration amplitude plot due to the direct relation between the two variables, highlighted also in Figure 6.13(b). Differential temperature peaks with values ranging from about 18 to 25 $^{\circ}C$ are shown for vibration amplitudes ranging from 70 to 125 μm $0-pk$. The maximum differential temperature related to a stable orbit condition is of about 7.8 $^{\circ}C$ obtained at 13200 rpm.

A linear trend is highlighted for all of the rotational speed when low amplitude vibrations are executed (see Figure 6.13(b)). If the vibration further increase a higher order polynomial is needed for representing the relation between vibration and predicted temperature. In particular, the stable orbit condition (below threshold case) is completely linear up to its stable configuration, while above the threshold the temperature rise is non-linear up to about 70 μm $0-pk$, the flat trend highlighted above is non-physical and it's due to the bearing contact. In fact, when SNAPSHOT is requested to run with an orbit amplitude which induces the contact with the pads, as for example at 90 μm $0-pk$, temperature given to the structural code for the simulation is the last available one. The simulation is performed until the assembled bearing clearance is overtaken by the orbit amplitude (for divergent cases).

It has to be noted that the highlighted trends of the relation between differential temperature and orbit amplitudes, shown in Figure 6.13(b), supports the results of the modelling choices. In fact, a linear trend is reported in the work of De Jongh [3] about an experimental campaign performed by Morton. Moreover, a similar behaviour is reported in the numerical work of Saha [26], where, after an initial linear trend for low-amplitude orbits, a non-linear relation is obtained for high-amplitude orbits.

W2 case

Similar considerations can be done for the W2 case, whose results are shown in Figure 6.14. In this case, the iterative model is able to predict the instability threshold with a good agreement. In fact, the

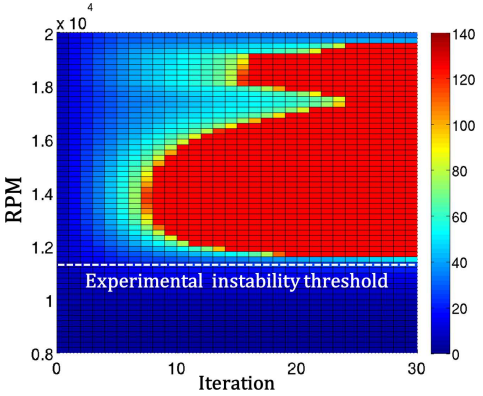

Figure 6.14: Results of the iterative model for the W2 case: vibration amplitude map.

experimental value has highlighted the instability onset at 11400 *rpm* and the same value is obtained by the iterative model for its first diverging rotational speed. A recover in stability is obtained for very high running speed values, of about 19600 to 20000 *rpm*. Unfortunately, this behaviour cannot be experimentally proved or denied since rotational speed above the first threshold have not been tested.

In Figure 6.15 the orbits obtained for each iteration of the procedure are shown for 11200 and 11400 *rpm*. A stable condition and divergence are respectively found, with the stable condition characterized by a vibration amplitude of about 28 μm $0-pk$. In terms of shaft differential temperature (Figure 6.16) a similar behaviour with respect to the one highlighted in the W3 case is obtained. The temperature map of Figure 6.16(a) results in fact similar to the amplitude map. The maximum differential temperature value obtained for a stable orbit is 5.6 $^{\circ}C$ for the 11200 *rpm* case. After the stability recovery at high speed a value of about 12 $^{\circ}C$ is found at 19600 *rpm*. Again, differential temperature peaks of about 18.5 to 25 $^{\circ}C$ are shown for vibration amplitudes near the range where bearing contact is expected and above (that is from 70 to 125 μm $0-pk$).

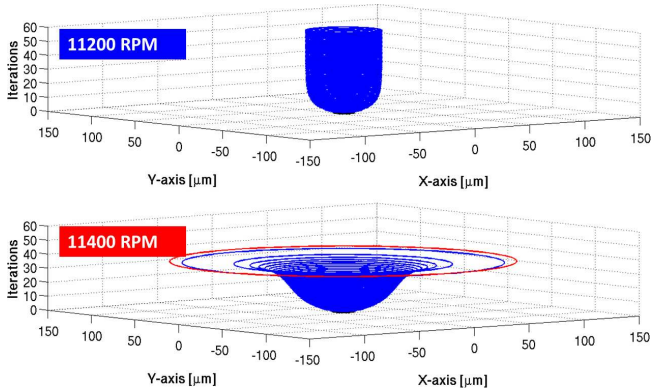

Figure 6.15: Details of the quasi-unsteady orbits evolution obtained from the iterative model: 11200 and 11400 *rpm* .

Furthermore, a linear trend is highlighted also for this case up to vibration amplitudes of about 40 μm $0-pk$ for the case above the threshold, which is referred to the 11800 *rpm* case. While completely linear behaviour is obtained for the stable case, which is referred to 11000 *rpm*.

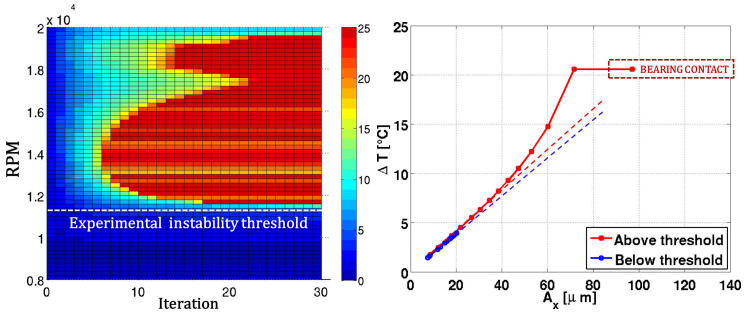

(a) W2-module of the shaft differential temperature.

(b) W2-differential temperature evolution: above and below instability threshold.

Figure 6.16: Results of the iterative model for the W2 case: differential temperature.

W1 case

In Figure 6.17 the results of the W1 case are presented in terms of vibration amplitude. For this analysed configuration, the model seems to

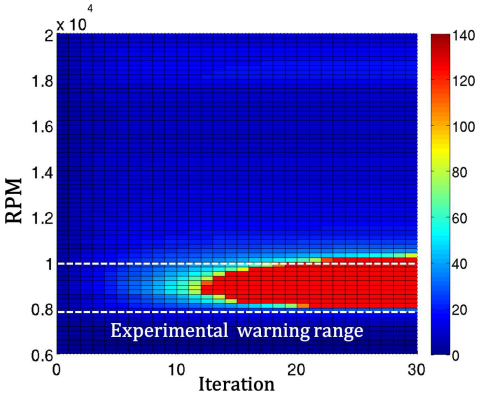

Figure 6.17: Results of the iterative model for the W1 case: vibration amplitude map.

over-predict the amplitude of the shaft displacements. In fact, although the experimental case showed an increase in vibrations up to a maximum of about 95 μm $pk-pk$ in the region between 8000 and 10000 rpm (defined as "warning range"), no unstable behaviour was detected. Instead, the model forecast the instability onset at 7800 rpm and a stability recovery at 10400 rpm. Such a misprediction results to be conservative in terms of rotor safety.

Figures 6.18 and 6.19 shows the orbits for both the instability onset and recovery. Stable behaviour is highlighted at 7600 and 10600 rpm with respectively 15.6 and 31.3 μm $0-pk$. Instead, unstable behaviour is obtained between the case at 7800 rpm and the case at 10400 rpm.

Finally, in terms of temperature, similar considerations can be done with respect to both the previous cases when analysing Figure 6.20. In terms of differential temperature map, again, a similar behaviour is obtained with respect to the amplitude maps. This time, values of about

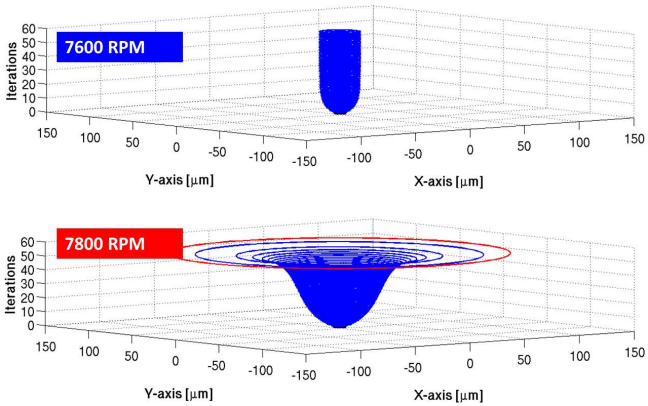

Figure 6.18: Details of the quasi-unsteady orbits evolution obtained from the iterative model: 7600 and 7800 *rpm*.

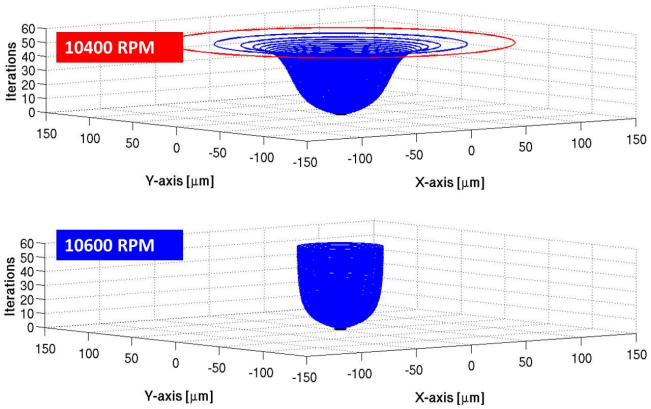

Figure 6.19: Details of the quasi-unsteady orbits evolution obtained from the iterative model: 10400 and 10600 *rpm*.

15 to 25 $^{\circ}C$ are obtained for the diverged region in the plot.

Four cases are presented this time in order to show the thermal development, with respect to the vibration orbit, below and above the two highlighted thresholds. The first one, is the instability threshold onset (threshold 1), while the second one is the stability recovery condition (threshold 2). Figure 6.20(b) shows the 7400 and 8200 *rpm* cases, which are respectively below and above threshold 1, and the 10000 and 10800 *rpm* cases, which are respectively below and above threshold 2. Linear trend is obtained for the stable tested conditions, while non-linear relations are obtained for the diverging ones, as in the previous cases. The

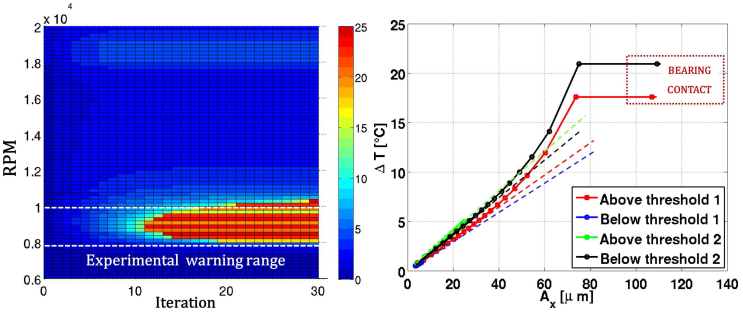

(a) W1-module of the shaft differential temperature.

(b) W1-differential temperature evolution: above and below instability thresholds.

Figure 6.20: Results of the iterative model for the W1 case: differential temperature.

increase in the slope representing the linear behaviour with the increase in rotational speed is here particularly clear due to the range of speed showed (minimum 7400 *rpm* and maximum at 10800 *rpm*).

Hot spot position

Figure 6.21 shows the predicted positions of the hot and high spots on the shaft for the three tested cases when the rotational speed is varied. Considering the position of the spots on the shaft, where zero is the

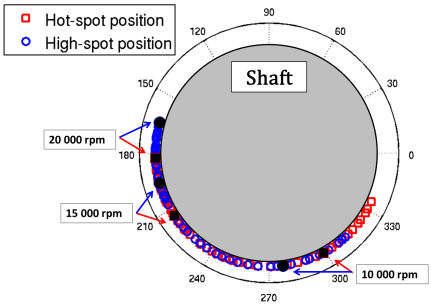

(a) W3-hot and high spots positions on the shaft.

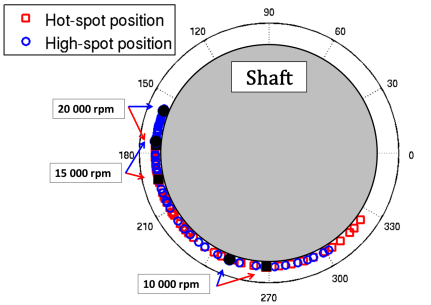

(b) W2-hot and high spots positions on the shaft.

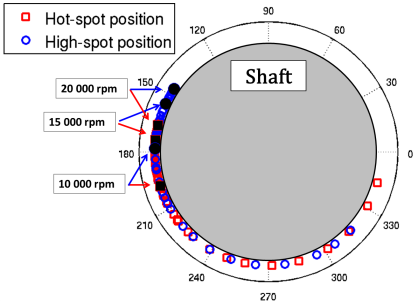

(c) W1-hot and high spots positions on the shaft.

Figure 6.21: Results of the iterative model: hot and high spots positions on the shaft varying the rotational speed.

direction of the mechanical unbalance force, two main considerations can be done.

The first one is about the behaviour of the code for the prediction of the differential temperature (SNAPSHOT), which gives an hot spot position always shifted of a value of about 20 *deg* with respect to the high spot position, where the latter is substantially given by the rotordynamic code. Although SNAPSHOT, due to its simplified nature, is not able to evaluate the hot spot position on the base of unsteady fluid dynamics effects, results are in line with literature, as discussed in Section 1.2, where the characteristics of the phenomenon are introduced.

The second consideration can be done about the general behaviour of the system moving from case $W3$ to case $W1$. The threshold of instability is obtained for all of the three tested case when the hot spot positions is approaching the 180 *deg*, and this is obtained at lower rotational speed values for the W1 case with respect to the W3 one.

6.4 Morton effect analysis and control

After the model has been proved to give quite reliable results, in terms of ability to forecast the instability onset, it has been considered for the analysis of the effects of some key parameters. The corrective actions presented in Chapter 1 have been considered for the purpose.

The majority of the proposed parameters have been studied numerically or experimentally in literature. Here, the effects of the shaft steel composition, which have not been yet referenced, are considered.

6.4.1 Sensitivity to the shaft material

The study of the effects of the elements which compose an alloy on its mechanical and thermal properties has increasing complexity with the increase in number of the components. However, although the components interaction affects the final results (in terms of alloy properties), some interesting information can be obtained by means of studying the effects of each single component.

For the purpose of the work, alloy steel is considered. In particular, the thermal characteristics of the steel should be varied in the way to suppress the shaft bending without modification of the mechanical characteristics needed for its application. Among the various components, Nickel has been individuated as a possible choice for this kind of solution due to its properties.

According to the work of Nicodemi [97], which introduces the main characteristics of steel and alloys, increasing the Nickel of a binary alloy $Fe-Ni$ results in a strong reduction of the thermal expansion coefficient (λ) and in a decrease of the thermal conductivity. For example, values of the thermal expansion coefficient of a $Fe-Ni$ binary alloy can range from a value of $20 \cdot 10^{-6}$ m/mK with a 20 % of Ni to a value of $2 \cdot 10^{-6}$ m/mK with a 36 % of Ni. A reduction of one order of magnitude can be thus obtained. Further increase in Ni drives the material towards an increase of λ and finally to a plateau at about $13 \cdot 10^{-6}$ m/mK.

The main consequence of a reduction of the thermal expansion coefficient λ is a reduction in the shaft thermal bend. Equation 6.10 reports the differential angle of the shaft due to the thermal deflection as calculated in the work of Balbahadur [19]. Hence, since the induced thermal unbalance should be less effective, Nickel should be considered for the purpose to reduce the undesirable effect.

$$\beta_{th} = \frac{\lambda \Delta T}{R_j} B \tag{6.10}$$

In terms of conductivity, a reduction is obtained increasing the Ni percentage. Starting from a value of approximatively 40 W/mK for low Ni percentage, a minimum of about 10 W/mK for a Ni quantity between 30 % $\div$ 40 % is obtained. Again, an increase up tp 40 W/mK is obtained above the percentage of Ni of the minimum point.

The effect of Nickel on alloy steel properties is complex to be examined due to the interaction among all of the components, typically: Fe, C, which constitute the steel, and Mn, Si, Ni, Cr, Mo, V, Al, B, Co, and so on. However, the main effect shown for the binary alloy $Fe-Ni$ can be considered as a general rule to qualitatively drive designers towards

the selection of the proper material. Furthermore, generally speaking, Nickel has beneficial effect both on the mechanical properties and thermal treatments of the alloy steel and hence no drawbacks are highlighted.

It has to be underlined that every time a material change is considered, all of the characteristics has to be carefully checked for the novel application.

A typical material for heavy duty shafts, gears and couplings is the $40NiCrMo6$ (equivalent to the $AISI4340$), characterized by a $1.65\% \div 2\%$ of Nickel. Its thermal characteristics are: an expansion coefficient λ of about $12.3 \cdot 10^{-6}\ m/mK$ and a conductivity of about $42\ W/mK$.

As previously stated, in accordance with the book of Nicodemi [97], the behaviour that has been highlighted for the binary $Fe - Ni$ alloy can also be generally considered for the construction alloy steel. Hence, a research of alloy steel with increased Nickel percentage has been done. Unfortunately, construction steel alloy have typically a maximum value of Nickel of about 5%. A further increase in Nickel is possible if high-alloy are considered, but these latter are characterized by a general increase of all of the components of the alloy. Approaching instead to the limit of the low-alloy steel it is possible to find, for example, the $34NiCrMo16$ with its $3.7\% \div 4\%$ of Nickel. This, has similar mechanical properties with respect to the $40NiCrMo6$ but has an expansion coefficient of about $11.3 \cdot 10^{-6}\ m/mK$.

A test is performed by means of the iterative model in order to evaluate the response of the system to such a modification. Four materials have been considered for the purpose: the first one is the $AISI4340$ which has been adopted as a reference case, referred to as $\lambda - 12$, the second one is the $34NiCrMo16$ with its reduced thermal expansion coefficient, referred to as $\lambda - 11$, the third and the fourth materials have been instead chosen with respectively $10.3 \cdot 10^{-6}$ and $6 \cdot 10^{-6}\ m/mK$ in order to evaluate the effects of an hypothesized increased of Nickel percentage (neglecting the effects of such an increase on other steel properties). These latter materials are respectively referred to as $\lambda - 10$ and $\lambda - 06$.

The novel simulations have been performed with an increased number

of model iterations, up to 80 iterations. The increase has been necessary in order to enable the model to reach convergence or diverge in unstable cases. Particularly, as expected, the case with the lowest thermal expansion coefficient has almost reached the maximum number of iterations before giving the desired results.

Results of the simulations are shown in Figure 6.22 for the three tested cases W1, W2 and W3.

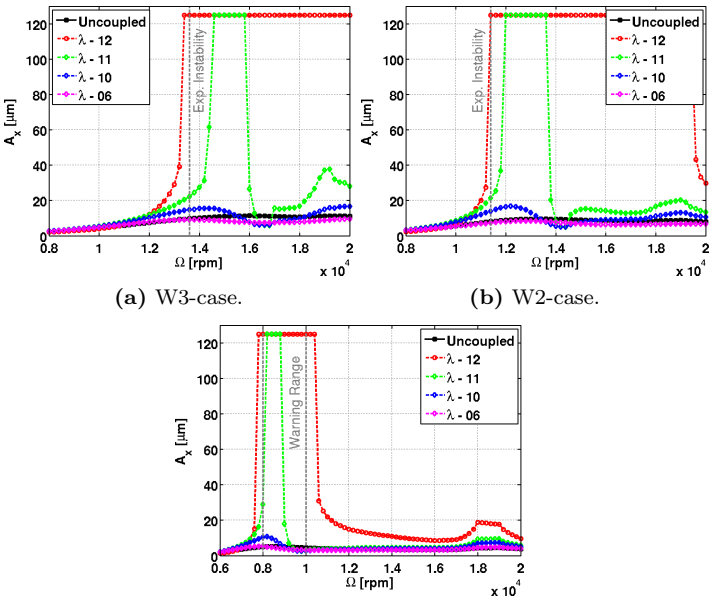

(a) W3-case.

(b) W2-case.

(c) W1-case.

Figure 6.22: Results of the iterative model: effects of the variation of the thermal expansion coefficient.

The model results to be highly sensitive to the thermal expansion coefficients, in fact, as it is possible to observe for all of the cases tested, a reduction of such a parameter (below 10%), moving from $\lambda - 12$ to $\lambda - 11$, results in a sensible reduction of the unstable range and in a reduction of the orbits amplitude when stable behaviour is highlighted.

A further reduction, considering the $\lambda - 10$ case, drives the system towards the complete stability for all of the three cases. A comparison with the amplitude of the uncoupled case has shown a maximum difference of about 7.7 μm $0 - pk$ for the $W2$ case at 12200 rpm.

If the thermal expansion coefficient is reduced down to the half of the value adopted as a reference, as for the $\lambda - 06$ case, negligible thermal effects are obtained.

The analysed parameter play a role in the thermal bending, as shown in Equation 6.10, that is comparable to the role of the differential temperature, hence, it is supposed that a similar reduction of the differential temperature can drive the system towards a stable behaviour. Such a reduction, as shown in the work of De Jongh and Van Der Hoeven [18], where a thermal barrier sleigh is presented, could be also obtained by means of thermal barrier coatings. This solution would be more easily applied at a problematic machine with respect to the sleeve and should have a lower impact on the global system behaviour due to its thin film nature. The main drawback lies in the fact that the reliability of such a solution, along the whole service life of the machine, has yet to be proved.

The proposed code for the differential temperature evaluation (SNAPSHOT) could be used also in presence of thermal barriers. In fact, this could be simply done considering a reduction of the module of the calculated differential temperature on the base of the barrier conductivity and thickness.

Conclusions

The field of the synchronous thermal instability, better known as Morton effect, is very complex and scarcely covered by the scientific literature. In fact, although in recent years the phenomenon is attracting attention from both the academic and industrial communities, as underlined by an increasing number of publications on the topic, a lack of knowledge is clearly highlighted in literature and the strategy to be adopted for its prediction and analysis is yet debated.

The main objective of the present work, realized in collaboration with GE Oil & Gas, is to develop predictive models for the Morton effect with particular focus on the thermo-hydrodynamic analysis of thin-film bearings. These components in fact, when operated on high performance machines, are prone to the development of complex thermal phenomena, which constitute the source for the whole process.

After a careful literature survey has been done, in order to better understand the physics of the problem and its state of the art, an analysis of the time scales involved in the process and of the orders of magnitude of the equations has been considered. By means of these kind of analysis an aware selection of the modelling strategies has been performed both in terms of the physical genesis of the phenomenon (thermo-hydrodynamic problem) and in terms of the global stability behaviour of the bearing-rotor system. The main outcome of this part of the work is the conceptual modelling of the complex physical system and the clear overview of the needed models and of the modelling strategy.

Two numerical codes have been developed and presented in the thesis

following the results of the previously cited analysis. The first one is an in-house code for the thermo-hydrodynamic analysis of PJBs and TPJBs, named TILTPAD. The second one is an in-house code for the evaluation of the differential temperature developed across the shaft during its synchronous precession motion, named SNAPSHOT.

In particular, TILTPAD is a steady state FEM code with a 2D thin film approach. It considers the effects of the local temperature on the dynamic viscosity and accounts for super-laminar effects by means of a simplified approach. The dynamic coefficients are also calculated following the well-known pad assembly method. The objective of the code is to give steady state equilibrium conditions in terms of relative eccentricity, attitude angles and tilt angles of the pads, which are needed by SNAPSHOT, and dynamic coefficients, which are needed by the rotordynamic models. These latter have been developed by the MDMlab of the Department of Industrial Engineering of the University of Florence. The code has been validated by means of comparison with available experimental and numerical data showing good results both in terms of global bearing parameters, such as equilibrium position of the shaft, frictional power losses and dynamic coefficients, and in terms of local parameters, such as pressure and temperature distributions inside of the oil film, resulting in a good trade-off between accuracy and computational costs. An improvement of the potential of the code has been obtained with the previously cited super-laminar modelling, which enabled to extend the analysis range towards more extreme operating conditions and gave quite accurate results with an almost negligible rise of the computational cost. Furthermore, a methodology for the uncertainty quantification analysis has been implemented, by means of a Monte Carlo method with response surfaces, and a preliminary evaluation of the effects of the uncertainty of the clearance and of the dynamic viscosity has been performed. This analysis is innovative in the field of fluid film bearings, at least in author's knowledge, and has given an interesting starting point to consider these effects, which could have a return also on the comprehension of the Morton effect.

The second code (SNAPSHOT), on the base of the equilibrium conditions received by TILTPAD evaluates, by means of a quasi-unsteady approach, the differential temperature developed across the shaft during its synchronous precession motion. The code has been validated by means of comparison with numerical data found in literature showing its ability to model the orders of magnitude of the problem.

Once the models for the thermo-hydrodynamic problem have been developed and validated the stability of the system has been studied. The two codes has been considered both for a linear stability analysis and for an iterative approach. The linear stability analysis showed potential for the prediction of the onset of the Morton effect, but more accurate results have been obtained with the iterative model. In order to adopt such a solution strategy the two numerical codes have been introduced inside of a complex architecture developed in collaboration with the MDMlab of the Department of Industrial Engineering of the University of Florence.

The validation of the iterative method has been obtained by means of comparison with experimental data derived from a dedicated experimental campaign carried out by GE Oil & Gas. Good results have been obtained in terms of prediction of the Morton effect onset for all of the three tested cases, allowing to obtain the prefixed results. The complete system of analysis, characterized by a low computational cost, makes the model interesting also to be adopted by the industry for the design and verification phase of the product.

Finally, once the model has been proved to give reliable results in assessing the system stability, it has been applied to evaluate the sensitivity of the models to some key parameters of the Morton effect. In particular, the sensitivity to the thermal expansion coefficient of the shaft has been tested since there were no previous study in the open literature. The analysis showed that a slight reduction, of about a 10%, of the thermal expansion coefficient resulted in a strong reduction both of the extension of the instability range and of the vibration amplitudes obtained within the stable operation range. A further 10% reduction has driven the whole system to a completely stable behaviour clearly showing the sensitivity

of the models to the tested parameter.

Appendix A

Orders of magnitude: time scales and governing equations

Contents

As mentioned in Chapter 2 and Chapter 3 the analysis of the time scales involved in the process and the analysis of the orders of magnitude of the governing equations has been performed in order, respectively, to

select the appropriate approach for the Morton effect prediction, and in order to simplify the governing equations maintaining physical consistency.

A.1 Time scales analysis

As previously stated, in order to improve the knowledge of the problem and allow an aware selection of the approach to be used for its prediction and analysis, it is necessary to perform a study of the orders of magnitude of the involved time scales.

A.1.1 Reference

The first step in the analysis is to evaluate some reference values to be used as a comparison. The analysed phenomenon is driven by synchronous vibrations and hence, time scales of the rotation are selected for the purpose. Three different rotational speed are selected in order to span some typical working range: 3000 rpm, 8000 rpm, 13000 rpm.

Table A.1 reports the rotational speed, frequencies and time scales for the three selected reference cases. As it is possible to observe, the reference time scales (τ_{ref}) of the phenomena related to the synchronous precession motion are of the order of 10^{-2} s - 10^{-3} s.

Rotational speed [rpm]	Frequency [Hz]	Reference time scale [s]
3000	50	0.020
8000	133.3	0.0075
13000	216.7	0.0046

Table A.1: Reference values of rotational speed, frequency and time scales.

Before time scales are evaluated, a brief introduction is presented. Lets imagine a step change of one of the variables affecting the problem, as for example the rotational speed, the static load or the dynamic load. The rotordynamic system finds a new working condition characterized by a new equilibrium point and orbit. About the oil flow, the fluid-dynamics

is modified and the variation is transmitted through the whole system transported by convection, diffusion and conduction terms. When these perturbations reach the solid surfaces, which constitute the boundaries of the fluid system, an interaction is performed by means of what we will refer to as convective heat transfer terms. Finally, the perturbation is diffused inside of the solid parts (shaft, pads and bush) by means of conduction, which drives the thermal deformation of the system and hence affects its rotordynamics behaviour which in turn affects again the fluid-dynamics behaviour closing the loop. Elastic phenomena are not considered in the present analysis since their time scale are lower than the thermal ones and since thermal phenomena are the main topic of the work. The complete analysis is proposed in the following adopting a different section for each different field of application of the the time scale.

A.1.2 Time scales of the conductivity within the solid domain

The time scales of the conduction within the solid parts are studied by means of the unsteady heat equation. Since radial and axial dimensions of fluid-film bearings are usually of the same order of magnitude, the time scale is studied for the radial diffusion only. The equation adopted is reported in polar coordinates in Equation A.1 where T is the temperature of the solid component, r is the radial coordinate, t is the time variable, and ρ_s, k_s and c_s are respectively the density, the conductivity and the specific heat characteristic of the material of the solid component (shaft, pads or bush).

$$\frac{\partial T}{\partial t} = \frac{k_s}{\rho_s c_s}\left(\frac{\partial^2 T}{\partial r^2} + \frac{1}{r}\frac{\partial T}{\partial r}\right) \tag{A.1}$$

Considering as constant the material properties and by means of selection of the following variables:

$$\tilde{T} = \Theta \tilde{T}^* \tag{A.2}$$

$$t = \tau t^* \tag{A.3}$$

$$r = R_j r^* \tag{A.4}$$

where $\tilde{T} = T - T_{ref}$ is the differential temperature with respect to a reference temperature value and R_j is the journal radius, it is possible to write the non-dimensional formulation proposed in Equation A.5.

$$\frac{\Theta}{\tau}\frac{\partial \tilde{T}^*}{\partial t^*} = \frac{k_s}{\rho_s c_s}\frac{\Theta}{R_j^2}\left(\frac{\partial^2 \tilde{T}^*}{\partial r^{*2}} + \frac{1}{r^*}\frac{\partial \tilde{T}^*}{\partial r^*}\right) \tag{A.5}$$

In order for the two terms to have the same orders of magnitude it is necessary that the physical time scale related to the problem is written in the following form:

$$\tau_{sc-shaft} = \frac{\rho_s c_s R_j^2}{k_s} \tag{A.6}$$

where ρ_s is the density, c_s and k_s are respectively the specific heat capacity and the thermal conductivity of the material composing the shaft and R_j is the journal radius.

Similar considerations can be done to find the conductive time scale of the conduction inside of the pads and of the bush of the bearing (reported in Equation A.7).

$$\tau_{sc-pads/bush} = \frac{\rho_s c_s (\Delta R)^2}{k_s} \tag{A.7}$$

Here, ΔR is the thickness of the pads (or of the bush). Since this latter is usually a fraction of the journal radius it is possible to understand that the bottleneck of the phenomenon is the thermal inertia of the shaft.

About the tangential and axial conduction, it is possible to consider similar results of the one obtained in Equation A.6. In fact, the axial length, the tangential extension (of shaft and pads) and the radial length of the bearing are usually of the same order of magnitude.

A.1.3 Time scales of the interaction within fluid and solid domains

Here is presented what will be referred to as the "convective time scale". Once the fluid has changed its own temperature, time is needed for the heat exchange between the fluid and solid surfaces to happen. It

is then the solid surface to drive the conductive action analysed in the previous section.

In the work of Ettles et al. [98] the surface temperature variation of both shaft and bush, driven by a step change of the fluid temperature, is presented as a function of the Nusselt number. According to the proposed diagrams and according to the value of the Nusselt number proposed in the same work as an upper bound value for fluid film bearings, it is possible to derive the time scales of the convective terms. These result to have a lower bound of the same order of magnitude of the conductive scales presented in Equation A.6.

In the same work [98], diagrams of the proportional thermal strain are also presented as a function of the Nusselt number. Once more, time scales similar to the one of the solid conduction mechanism are found. This is an expected result since it is the thermal diffusion which generates the temperature variation and hence the thermal deformation. In Equation A.8 the thermal strain ϵ_T is presented as a function of the thermal expansion coefficient λ, of the temperature variation ΔT and of the proportional thermal strain ϵ_T^*. This latter ranges from zero to one that is from a no strain condition to a complete thermal expansion or contraction.

$$\epsilon_T = \lambda \Delta T \epsilon_T^* \tag{A.8}$$

A.1.4 Time scales of the phenomena within the fluid domain

The thermal time scales related to the energy equation of the fluid are analysed starting from its non-dimensional form presented in Equation A.9. The procedure to obtained the proposed formulation and the introduced non-dimensional parameters are shown and detailed further, when the analysis of the orders of magnitudes of the equations is presented.

$$Pe(\frac{\partial \tilde{T}^*}{\partial t^*} + u_1^* \frac{\partial \tilde{T}^*}{\partial x_1^*} + u_2^* \frac{\partial \tilde{T}^*}{\partial x_2^*} + u_3^* \frac{\partial \tilde{T}^*}{\partial x_3^*}) = \frac{\partial^2 \tilde{T}^*}{\partial x_2^{*2}} + Br[\mu^* (\frac{\partial u_1^*}{\partial x_2^*})^2 + \mu^* (\frac{\partial u_3^*}{\partial x_2^*})^2] \tag{A.9}$$

By means of comparison between the unsteady term with the convective, conductive and dissipative one it is possible to evaluate the expected time scales. About the convective terms, the same order of magnitude of the reference time scale is obtained. It means, as expected, that the thermal convection is driven by the shaft rotation and hence has the same characteristic time.

Instead, about the dissipative and conductive terms it is possible to obtained the following formulations:

$$\tau_{fc} = \frac{\rho c}{k} C_b^2 \tag{A.10}$$

$$\tau_{fd} = \frac{\rho c}{\mu} \frac{C_b^2}{U^2} \tag{A.11}$$

where U is the peripheral speed of the shaft, C_b is the assembled bearing clearance and ρ, k, c and μ are respectively the density, conductivity, specific heat and dynamic viscosity of the fluid.

A.1.5 Results

The results obtained from the time scale analysis are summarized in Table A.2 according to some of the test-case presented in Chapter 3.

time scale type	symbol	value [s]	normalized value τ/τ_{ref} [-]
reference	τ_{ref}	$10^{-3} - 10^{-2}$	1
fluid convection	τ_{fcv}	$10^{-3} - 10^{-2}$	1
fluid conduction	τ_{fcd}	10^{-1}	$10^{-2} - 10^{-1}$
fluid dissipation	τ_{fd}	10^{-3}	$10^{-1} - 10^{0}$
convective heat transfer	τ_{cht}	$\geq 10^2$	$\geq 10^4$
solid conduction	τ_{sc}	$10^2 - 10^3$	$10^4 - 10^6$
thermal deformation	τ_{td}	$10^2 - 10^3$	$10^4 - 10^6$

Table A.2: Comparison among the thermal time scales of the problem.

The main outcome, as expected, is that thermal inertia of the metallic parts is responsible for very long conductive time scales and hence, this specific physical process results to be the bottleneck of the phenomenon.

A.2 Dimensionless equations

An analysis of the orders of magnitude of the governing equations of the incompressible lubrication problem is performed in this section. Continuity and momentum equations will be firstly considered together with some considerations about the consequent simplifications, then, the energy equation will be analysed for the same purpose.

The following conditions constitute some classical hypothesis for this kind of problems:

- $h/B \simeq C_b/B << 1$
- $h/R_j \simeq C_b/R_j << 1$
- Incompressible fluid
- Newtonian fluid
- Stokes relation
- Fourier's law
- Laminar flow
- Constant specific heat capacity of the oil
- Constant thermal conductivity of the oil

The main consequence of the geometrical condition related to the length scale of the problem ($C_b/R_j << 1$) is the opportunity to neglect curvature effects and hence, adopt Cartesian coordinates. A sketch of the problem with its reference system is shown in Figure A.1.

A.2.1 Continuity and momentum equations

The general conservative form of the continuity and momentum equations are shown in Equations A.12 A.13, expressed with the Einstein notation:

$$\frac{\partial \rho}{\partial t} + \frac{\partial \rho u_j}{\partial x_j} = 0 \tag{A.12}$$

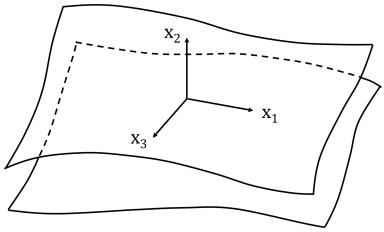

Figure A.1: Sketch of a lubrication problem and its reference system.

$$\frac{\partial \rho u_i}{\partial t} + \frac{\partial \rho u_i u_j}{\partial x_j} = \frac{\partial \tau_{ij}}{\partial x_j} + \rho f_i \tag{A.13}$$

where the stress tensor τ_{ij} with the Newtonian fluid hypothesis and the Stokes relation is represented by Equation A.14.

$$\tau_{ij} = -p\delta_{ij} + \mu(\frac{\partial u_i}{\partial x_j} + \frac{\partial u_j}{\partial x_i}) - \frac{2}{3}\mu(\frac{\partial u_j}{\partial x_j})\delta_{ij} \tag{A.14}$$

The flow is incompressible, hence, the continuity equation simplify as follows:

$$\frac{\partial u_j}{\partial x_j} = 0 \tag{A.15}$$

Moreover, rearranging the momentum equations, considering a constant density, it is possible to obtain the following expression:

$$\frac{\partial u_i}{\partial t} + \frac{\partial u_i u_j}{\partial x_j} = -\frac{1}{\rho}\frac{\partial p}{\partial x_i} + \frac{1}{\rho}\frac{\partial [\mu(\frac{\partial u_i}{\partial x_j} + \frac{\partial u_j}{\partial x_i})]}{\partial x_j} + f_i \tag{A.16}$$

Dimensional variables are written in terms of non-dimensional ones as defined in Equations A.17, A.18 for both spatial coordinates and velocities.

$$x_1 = x_1^* R_j \qquad x_2 = x_2^* C_b \qquad x_3 = x_3^* B \simeq x_3^* R_j \tag{A.17}$$

$$u_1 = u_1^* U \qquad u_2 = u_2^* V \qquad u_3 = u_3^* W \simeq u_3^* U \tag{A.18}$$

In the presented definitions R_j is the bearing radius, $U = \Omega R_j$ is the sliding velocity of the runner surface, C_b is the bearing clearance and B

is the axial extension of the bearing.

By means of substitutions of the defined variables and rearranging, the continuity equation can be written in its non-dimensional form, shown in Equation A.19.

$$\frac{V}{C_b}\frac{\partial u_2^*}{\partial x_2^*} + \frac{U}{R_j}(\frac{\partial u_1^*}{\partial x_1^*} + \frac{\partial u_3^*}{\partial x_3^*}) = 0 \tag{A.19}$$

In order to have all the terms in the continuity equation of the same order of magnitude the cross-film velocity V must be defined as in Equation A.20. Thus, the cross-film velocity results much smaller than the tangential and axial ones ($V << U$).

$$V = \frac{U}{R_j}C_b \tag{A.20}$$

For the momentum equation some other variables need to be defined in terms of their nondimensional representation (Equation A.21). Here, τ is the characteristic time, which for bearings is $\tau = R_j/U = 1/\Omega$, g is the gravitational acceleration and μ_0 is the oil viscosity.

$$\begin{aligned} t &= t^*\tau & p &= p^*\frac{\mu_{oil}UR_j}{C_b^2} \\ \mu &= \mu^*\mu_{oil} & f_i &= f_i^* g \end{aligned} \tag{A.21}$$

By means of substitution and manipulation, considering the momentum equation in the x_1 direction, Equation A.22 is obtained.

$$\begin{aligned} &\frac{\rho\Omega C_b^2}{\mu_{oil}}\frac{\partial u_1^*}{\partial t^*} + \frac{\rho U C_b^2}{\mu_{oil}R_j}(u_1^*\frac{\partial u_1^*}{\partial x_1^*} + u_2^*\frac{\partial u_1^*}{\partial x_2^*} + u_3^*\frac{\partial u_1^*}{\partial x_3^*}) = -\frac{\partial p^*}{\partial x_1^*} + \frac{\partial(\mu^*\frac{\partial u_1^*}{\partial x_2^*})}{\partial x_2^*} + \\ &+ (\frac{C_b}{R_j})^2[2\frac{\partial(\mu^*\frac{\partial u_1^*}{\partial x_1^*})}{\partial x_1^*} + \frac{\partial(\mu^*\frac{\partial u_2^*}{\partial x_1^*})}{\partial x_2^*} + \frac{\partial(\mu^*\frac{\partial u_1^*}{\partial x_3^*})}{\partial x_3^*} + \frac{\partial(\mu^*\frac{\partial u_3^*}{\partial x_1^*})}{\partial x_3^*}] + \frac{\rho g C_b^2}{\mu_{oil}U}f_1^* \end{aligned} \tag{A.22}$$

Since for journal bearings the term C_b/R_j is usually of the order of 10^{-3}, the term $(C_b/R_j)^2 << 1$ and hence can be neglected. Furthermore, the following terms are defined: the flow Reynolds number (Re), the modified

Reynolds number (Re^*), the squeeze film Reynolds (Re_s) and the Froude number (Fr).

$$Re = \frac{\rho U C_b}{\mu_{oil}} \tag{A.23}$$

$$Re^* = Re(\frac{C_b}{R_j}) \tag{A.24}$$

$$Re_s = \frac{\rho \Omega C_b^2}{\mu_{oil}} \tag{A.25}$$

$$Fr = \frac{U^2}{g R_j} \tag{A.26}$$

By means of substitution of Equations A.23, A.24, A.25, A.26 in Equation A.22, the nondimensional momentum equation in the x_1 direction is obtained (Equation A.27):

$$Re_s \frac{\partial u_1^*}{\partial t^*} + Re^*[(u_1^* \frac{\partial u_1^*}{\partial x_1^*} + u_2^* \frac{\partial u_1^*}{\partial x_2^*} + u_3^* \frac{\partial u_1^*}{\partial x_3^*})] = -\frac{\partial p^*}{\partial x_1^*} + \frac{\partial(\mu^* \frac{\partial u_1^*}{\partial x_2^*})}{\partial x_2^*} + \frac{Re^*}{Fr} f_1^* \tag{A.27}$$

Same considerations can be done for the momentum equation in direction x_3, driving to the Equation A.28.

$$Re_s \frac{\partial u_3^*}{\partial t^*} + Re^*[(u_1^* \frac{\partial u_3^*}{\partial x_1^*} + u_2^* \frac{\partial u_3^*}{\partial x_2^*} + u_3^* \frac{\partial u_3^*}{\partial x_3^*})] = -\frac{\partial p^*}{\partial x_3^*} + \frac{\partial(\mu^* \frac{\partial u_3^*}{\partial x_2^*})}{\partial x_2} + \frac{Re^*}{Fr} f_3^* \tag{A.28}$$

In Table A.3, proposed at the end of this section, the values of the typical non-dimensional groups evaluated on some plain and tilting pad bearings found in literature are reported. It has to be noted that for the given definition of τ in bearings application the two defined Reynolds number Re^* and Re_s result to be identical.

As it is possible to observe, except for the test cases of Daniel and Cavalca [47] and Taniguchi et al. [51] where inertial effects are of importance, for the majority of the presented cases the modified Reynolds number is about one order of magnitude below the unitary value. Hence, the inertial terms can be disregarded. Furthermore, according to the values of Fr number the terms related to the volume forces can be even

more neglected. Hence, momentum equations can be further simplified, obtaining the final dimensional momentum Equations A.29, A.30:

$$\frac{\partial p}{\partial x_1} = \frac{\partial(\mu \frac{\partial u_1}{\partial x_2})}{\partial x_2} \tag{A.29}$$

$$\frac{\partial p}{\partial x_3} = \frac{\partial(\mu \frac{\partial u_3}{\partial x_2})}{\partial x_2} \tag{A.30}$$

About the x_2 direction, momentum equation can be further simplified. In fact, as it is possible to observe from the non-dimensional form presented in Equation A.31, similar non-dimensional groups, with respect to the x_1 and x_3 directions, are highlighted multiplied by factors C_b/R_j and $(C_b/R_j)^2$ which further reduce their order of magnitude.

$$\begin{aligned}&\frac{\rho\Omega C_b^2}{\mu_{oil}}(\frac{C_b}{R_j})^2\frac{\partial u_2^*}{\partial t^*} + \frac{\rho U C_b^2}{\mu_{oil} R_j}(\frac{C_b}{R_j})^2(u_1^*\frac{\partial u_2^*}{\partial x_1^*} + u_2^*\frac{\partial u_2^*}{\partial x_2^*} + u_3^*\frac{\partial u_2^*}{\partial x_3^*}) = -\frac{\partial p^*}{\partial x_2^*} + \\ &+ (\frac{C_b}{R_j})^4\frac{\partial(\mu^*\frac{\partial u_2^*}{\partial x_1^*})}{\partial x_1^*} + (\frac{C_b}{R_j})^2[(\frac{C_b}{R_j})\frac{\partial(\mu^*\frac{\partial u_1^*}{\partial x_2^*})}{\partial x_1^*} + 2\frac{\partial(\mu^*\frac{\partial u_2^*}{\partial x_2^*})}{\partial x_2^*} + (\frac{C_b}{R_j})^2\frac{\partial(\mu^*\frac{\partial u_2^*}{\partial x_3^*})}{\partial x_3^*} + \\ &+ \frac{\partial(\mu^*\frac{\partial u_3^*}{\partial x_2^*})}{\partial x_3^*}] + \frac{\rho g C_b^2}{\mu_{oil} U}\frac{C_b}{R_j} f_2^*\end{aligned} \tag{A.31}$$

As a consequence, the final viscous terms of the momentum equation in the cross film direction results to be even more simplified with respect to the other two directions, as shown in Equation A.32. The dimensional formulation shown in Equation A.33 is finally obtained considering the characteristic values of the non-dimensional groups of the lubrication problem.

$$Re_s(\frac{C_b}{R_j})^2\frac{\partial u_2^*}{\partial t^*} + Re^*(\frac{C_b}{R_j})^2(u_1^*\frac{\partial u_2^*}{\partial x_1^*} + u_2^*\frac{\partial u_2^*}{\partial x_2^*} + u_3^*\frac{\partial u_2^*}{\partial x_3^*}) = -\frac{\partial p^*}{\partial x_2^*} + \frac{Re^*}{Fr}\frac{C_b}{R_j} f_2^* \tag{A.32}$$

$$\frac{\partial p}{\partial x_2} = 0 \tag{A.33}$$

One of the main outcome of such analysis, together with the simplification

of the momentum equations is that pressure variation across the fluid film result to be negligible ($p(x, y, z, t) \simeq p(x, z, t)$), thus enabling a two-dimensional thin-film approach.

A.2.2 Energy equation

The energy equation adopted to start the analysis is written for the incompressible lubrication problem in terms of differential temperature and is shown in Equation A.34.

$$\rho c(\frac{\partial \tilde{T}}{\partial t} + u_j \frac{\partial \tilde{T}}{\partial x_j}) = \frac{\partial (k \frac{\partial \tilde{T}}{\partial x_j})}{\partial x_j} + \Phi_{ij} \tag{A.34}$$

The term Φ_{ij} represents the dissipation function, k is the conductivity of the oil, c is the specific heat capacity and $\tilde{T} = T - T_{ref}$, where T_{ref} is a reference temperature.

In order to enable the non-dimensionalization together with the variables defined in Equations A.17, A.18 and A.21 a new variable needs to be defined:

$$\tilde{T} = \tilde{T}^* \Theta \tag{A.35}$$

By means of substitution and manipulation, considering the order of magnitude of V evaluated with the continuity equation, the energy equation is written as follows:

$$\begin{aligned}
&\rho c \frac{\Theta}{\tau} \frac{\partial \tilde{T}^*}{\partial t^*} + \rho c \frac{U\Theta}{R_j}(u_1^* \frac{\partial \tilde{T}^*}{\partial x_1^*} + u_2^* \frac{\partial \tilde{T}^*}{\partial x_2^*} + u_3^* \frac{\partial \tilde{T}^*}{\partial x_3^*}) = k \frac{\Theta}{C_b^2}[\frac{C_b^2}{R_j^2} \frac{\partial^2 \tilde{T}^*}{\partial x_1^{*2}} + \\
&+ \frac{\partial^2 \tilde{T}^*}{\partial x_2^{*2}} + \frac{C_b^2}{R_j^2} \frac{\partial^2 \tilde{T}^*}{\partial x_3^{*2}}] + \mu_{oil} \frac{U^2}{C_b^2}[2\frac{C_b^2}{R_j^2}\mu^*(\frac{\partial u_1^*}{\partial x_1^*})^2 + 2\frac{C_b^2}{R_j^2}\mu^*(\frac{\partial u_2^*}{\partial x_2^*})^2 + \\
&+ 2\frac{C_b^2}{R_j^2}\mu^*(\frac{\partial u_3^*}{\partial x_3^*})^2 + \mu^*(\frac{\partial u_1^*}{\partial x_2^*})^2 + \frac{C_b^4}{R_j^4}\mu^*(\frac{\partial u_2^*}{\partial x_1^*})^2 + 2\frac{C_b^2}{R_j^2}\mu^* \frac{\partial u_1^*}{\partial x_2^*}\frac{\partial u_2^*}{\partial x_1^*} + \\
&+ \frac{C_b^4}{R_j^4}\mu^*(\frac{\partial u_2^*}{\partial x_3^*})^2 + \mu^*(\frac{\partial u_3^*}{\partial x_2^*})^2 + 2\frac{C_b^2}{R_j^2}\mu^* \frac{\partial u_2^*}{\partial x_3^*}\frac{\partial u_3^*}{\partial x_2^*} + \frac{C_b^2}{R_j^2}\mu^*(\frac{\partial u_3^*}{\partial x_1^*})^2 + \\
&+ \frac{C_b^2}{R_j^2}\mu^*(\frac{\partial u_1^*}{\partial x_3^*})^2 + 2\frac{C_b^2}{R_j^2}\mu^* \frac{\partial u_1^*}{\partial x_3^*}\frac{\partial u_3^*}{\partial x_1^*}]
\end{aligned} \tag{A.36}$$

By means of simplification of the lower order terms and considering the definition adopted for the reference time within the journal bearing field, Equation A.37 is obtained as follows:

$$\rho c\frac{U\Theta}{R_j}(\frac{\partial\tilde{T}^*}{\partial t^*}+u_1^*\frac{\partial\tilde{T}^*}{\partial x_1^*}+u_2^*\frac{\partial\tilde{T}^*}{\partial x_2^*}+u_3^*\frac{\partial\tilde{T}^*}{\partial x_3^*})=k\frac{\Theta}{C_b^2}\frac{\partial^2\tilde{T}^*}{\partial x_2^{*2}}+ \\ +\mu_{oil}\frac{U^2}{C_b^2}[\mu^*(\frac{\partial u_1^*}{\partial x_2^*})^2+\mu^*(\frac{\partial u_3^*}{\partial x_2^*})^2] \tag{A.37}$$

Non-dimensional terms related to the energy equation are defined in Equations A.38, A.39, A.40 and A.41.

$$Pr=\frac{c\mu_{oil}}{k} \tag{A.38}$$

$$Pe=\frac{\rho c}{k}\frac{UC_b^2}{R_j}=PrRe^* \tag{A.39}$$

$$Ec=\frac{U^2}{c\Theta} \tag{A.40}$$

$$Br=\frac{\mu_{oil}U^2}{k\Theta}=PrEc \tag{A.41}$$

The Peclet number (Pe) is the ratio of advective transport rate and diffusive transport rate, while the Brinkman number (Br) is the ratio of viscous dissipation rate to thermal conduction.

If further manipulation is done, together with the substitution of the defined non-dimensional terms, the non-dimensional energy equation is finally obtained (Equation (A.42)).

$$Pe(\frac{\partial\tilde{T}^*}{\partial t^*}+u_1^*\frac{\partial\tilde{T}^*}{\partial x_1^*}+u_2^*\frac{\partial\tilde{T}^*}{\partial x_2^*}+u_3^*\frac{\partial\tilde{T}^*}{\partial x_3^*})=\frac{\partial^2\tilde{T}^*}{\partial x_2^{*2}}+Br[\mu^*(\frac{\partial u_1^*}{\partial x_2^*})^2+\mu^*(\frac{\partial u_3^*}{\partial x_2^*})^2] \tag{A.42}$$

The numerical values of the characteristic groups for some cases found in literature are shown in Table A.3. Particular focus is devoted to the Pe and Br numbers although also Pr and Ec numbers are reported. The variation of both the numbers is substantial: the Pe number varies from 14.9 of Fitzgerald and Neal [45] to 1557 of Taniguchi et al. [51] (for lower

rotational speed, not reported in the table, a value of 3.7 is found for the case of Fitzgerald and Neal [45]), while the Br number varies from 3.8 of the Lund and Tonnesen [46] case up to 155 of the work of Daniel and Cavalca [47] (again, for lower rotational speed a unitary value of Br is obtained for the case of Fitzgerald and Neal [45]). This highlights the opportunity for some specific cases to adopt the adiabatic solution, which has been introduced as the first approximation to solve the problem, even if, more in general, the complete three dimensional energy equation to be adopted is shown in Equation A.43.

$$\rho c(\frac{\partial T}{\partial t} + u_1\frac{\partial T}{\partial x_1} + u_2\frac{\partial T}{\partial x_2} + u_3\frac{\partial T}{\partial x_3}) = k\frac{\partial^2 T}{\partial x_2^2} + [\mu(\frac{\partial u_1}{\partial x_2})^2 + \mu(\frac{\partial u_3}{\partial x_2})^2] \tag{A.43}$$

Of course if a steady state problem is studied, as in this case, the first term of the equation is neglected.

Furthermore, if the differential temperature developed along the tangential, radial and axial directions are no more represented by the generic term Θ, but have the specific representation of respectively Θ_1, Θ_2 and Θ_3 then an evaluation of the goodness of the approximation adopted when dealing with the convective terms can be obtained. The radial and axial differential temperature have been evaluated in terms of the tangential one by means of a coefficient C_{12} and C_{13} as shown in Equation A.44:

$$\Theta_2 = C_{12}\Theta_1 \qquad\qquad \Theta_3 = C_{13}\Theta_1 \tag{A.44}$$

A research of some typical values has been done in literature between experimental and numerical results. Some of the evaluated papers are: He et al. [78], Ettles [59], Fillon et al. [48] and Daniel and Cavalca [47]. Values of C_{12} between 0.3 and 0.5 are highlighted, while values of C_{13} result to be ranging between 0.16 and 0.3. Hence, if an approximation has to be chosen it is better to consider the radial temperature variation than the axial one.

A.3 Non-dimensional characteristic groups

An analysis of the values of the non-dimensional groups characteristic of the problem is presented. Data have been taken from literature and are referred to the works listed below.

1. Ferron et al. [44] (PJB): referred to as TC01
2. Fitzgerald and Neal [45] (PJB): referred to as TC02
3. Lund and Tonnesen [46] (PJB): referred to as TC03
4. Daniel and Cavalca [47] (TPJB): referred to as TC04
5. Fillon et al. [48] (TPJB): referred to as TC05
6. Knight [49] (TPJB): referred to as TC06
7. Monmousseau et al. [50] (TPJB): referred to as TC07
8. Taniguchi et al. [51] (TPJB): referred to as TC08

	TC01	TC02	TC03	TC04	TC05	TC06	TC07	TC08
C_b/R	0.0029	0.001	0.0013	0.0015	0.0016	0.0016	0.0016	0.0026
Re	93	59	81	606	51	60	51	1429
Re^*	0.27	0.05	0.1	0.9	0.1	0.1	0.1	3.7
Ta	5	1.9	3	24	2	2.4	2	72
Fr	895	2728	1398	6875	895	2721	895	2412
Pr	430	252	244	540	426	396	426	426
Pe	116	15	26.5	498	34.6	37.6	34.6	1556
Br	9.4	5.3	3.8	155	3.7	9.1	6.2	48
Ec	0.02	0.02	0.01	0.3	0.01	0.02	0.01	0.11

Table A.3: Main nondimensional groups of the lubrication problem for some typical test cases found in literature.

Appendix B

Simplified mixing model for plain journal bearings

Contents

As explained in Chapter 3, in case the code is used as a plain bearing solver, the simplified mixing model (i.e., the one based on the Petroff's type hypothesis) is slightly modified.

B.1 Description of the problem

The need for the development of a novel mixing model is substantially due to some geometrical considerations. The typical film-thickness distribution along the tangential direction of the pad in case a TPJB is evaluated has been shown in Chapter 3, when the improved mixing model has been described. For these kind of bearings the trailing edge of the pad has a film-thickness that is usually similar to its minimum film-thickness,

and hence, considering the Petroff's type hypothesis, the flow rate considered at the trailing edge (on the base of the trailing edge film-thickness) is quite representative of the real flow rate observed downstream of the pad.

When plain journal bearings are considered the previously highlighted consideration is no more effective, and the model, based on the inlet and outlet film-thickness, needs to be changed.

B.2 Mixing model for PJBs

The novel model considers different mixing models on the base of the region of the bearing. As shown in Figure B.1, a bearing can have a loaded region, defined as the region where the minimum film-thickness is obtained, and zero, one or more unloaded regions, on the base of the number of sectors (or grooves) composing the bearing.

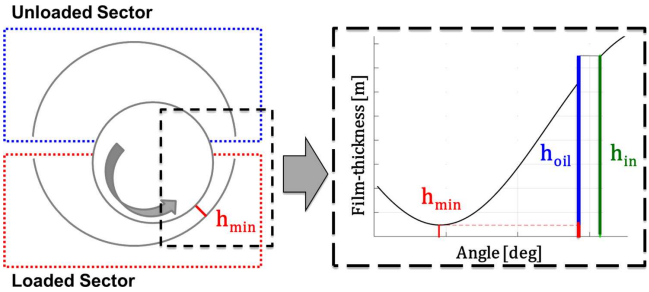

Figure B.1: Schematic of the geometrical configuration for the mixing model of plain journal bearings.

In case a PJB is solved two mixing models are adopted: the first one is based on continuity and thermal balance downstream of the loaded region, while the second is a percentage model adopted downstream of the unloaded sectors.

When the model based on the balance in the groove is considered, the improved mixing model presented for TPJBs is adopted considering the minimum film-thickness instead of the one at the trailing edge of the pad.

The inlet temperature formulation obtained is shown in Equation B.1.

$$T_{in} = \frac{h_{min}}{h_{in}} T_{out} + \frac{h_{in} - h_{min}}{h_{in}} T_{oil} \tag{B.1}$$

Downstream of the unloaded region the percentage model shown in Equation B.2 is adopted, where η represents the percentage coefficient of hot oil at the inlet of the following section.

$$T_{in} = \eta T_{out} + (1 - \eta) T_{oil} \tag{B.2}$$

Since a percentage approach has been considered, although only downstream of the unloaded regions, the model needs to be assessed in comparison with experimental data in order to obtained the value of η to be adopted for the simulations. Figure B.2 shows the results of the model assessment, which has been performed on the Lund and Hansen [57] test case, in terms of normalized relative eccentricity and frictional power losses at 3500 $[rpm]$ and 5600 $[N]$. The obtained value of hot oil at the

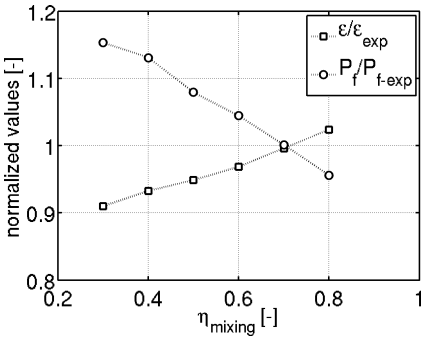

Figure B.2: Results of the mixing model assessment.

inlet section is about 70% represented by a value of $\eta = 0.7$. All of the results for plain journal bearings shown in Chapter 3 are obtained with the present model configuration.

B.3 Literature models

Three models found in the open literature have been also tested. The first one is referred to the work of Brito [99], where a mixing model based on a fixed percentage of hot and cold oil is presented, the second one is referred to the work of Balbahadur [19], where the temperature of the inlet oil flow is evaluated by means of an effective temperature raise (discussed in Chapter 3) and the third is referred to the work of Heshmat and Pinkus [100], where an experimental correlation is given.

The first model is taken from the work of Brito [99]. In his work a percentage model is presented with the inlet temperature defined as shown in Equation B.3, where $\eta = Q_{out}/Q_{in}$.

$$T_{in} = \eta T_{out} + (1 - \eta) T_{oil} \tag{B.3}$$

The second model is taken from the work of Balbahadur [19]. In his work, inlet temperature is considered to be the sum of lubricant supply temperature and the estimated average temperature raise on the bearing (ΔT_{ave}), this latter multiplied by a scaling ratio that is function of the minimum inlet film thickness h_{min-in} and of the inlet film-thickness h_{in} of the analysed pad. The obtained formulation is shown in Equation B.4.

$$T_{in} = T_0 + \frac{h_{min-in}}{h_{in}} \cdot \Delta T_{ave} \tag{B.4}$$

The last model, is taken from the work of Heshmat and Pinkus [100] and is based on an experimental correlation. Here, an extensive discussion on the mechanism of the mixing is given, presenting some features characteristic of the real process, as for example: the hot oil layer attached to the shaft, the cold oil layer entering in the inlet section, the recirculation at the leading edge, the back flow upstream of the groove, the cavitation, three-dimensional effects, heat exchange with the walls of the groove and dissipation inside of the mixing groove.

About the model, starting from the thermal balance on the mixing groove (Equation B.5), the value of the inlet temperature is obtained by

means of the following equation:

$$cQ_{out}(T_{out} - T_{ref}) + cQ_{oil}(T_{oil} - T_{ref}) = cQ_{in}(T_{in} - T_{ref}) \tag{B.5}$$

According to the authors, the inlet temperature obtained (T_{in}) is not realistic due to the mechanisms previously highlighted, which the simple thermal balance cannot account for. Hence, an experimental correlation has been defined in terms of the parameter ι which is a function of the tangential velocity U and of the feeding oil temperature T_{oil}. The obtained inlet temperature is shown in Equation B.6 where $T_{ref} = -17.7°C$.

$$T_{in} = \frac{Q_{oil}T_{oil} + Q_{out}T_{out} - (\frac{160}{9})\iota Q_{in}}{Q_{in}(1+\iota)} \tag{B.6}$$

The results of the comparison among the tested literature models are shown in Figure B.3. The percentage model obviously fits the assess-

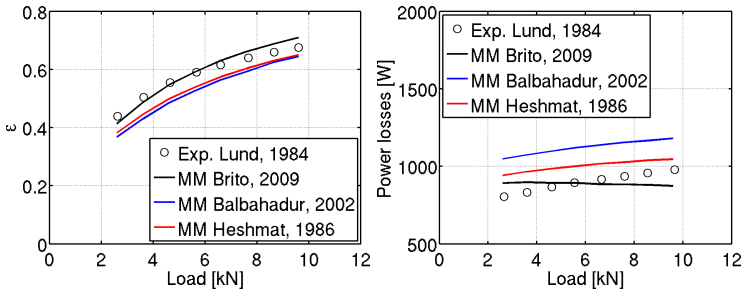

(a) Relative eccentricity. **(b)** Frictional power losses.

Figure B.3: Comparison of the three models found in literature.

ment condition (3500 $[rpm]$ and 5600 $[N]$) but results are not in good agreement with experiments particularly for the frictional power losses where the trend is also mispredicted. About the eccentricity ratio a maximum difference with respect to the experimental data of about 6% is obtained for low loads.

The other two models show good trend prediction for both the relative eccentricity and the power losses, with 13% and 16% underestimantion

of the relative eccentricity, respectively obtained for the Balbahadur [19] model and for the Heshmat and Pinkus [100] model. Moreover, overestimation of about 17% to 30% is obtained for the frictional power losses respectively by Balbahadur [19] and Heshmat and Pinkus [100] models.

Bibliography

[1] F. De Jongh and P. G. Morton. The Synchronous Instability of a Compressor Rotor Due to Bearing Journal differential Heating. *ASME paper No. 94-GT-35*, 1994.

[2] American Petroleum Institute. *API Recommended Practice 684, API Standard Paragraphs Rotordynamic Tutorial: Lateral Critical Speeds, Unbalance Response, Stability, TrainTorsionals, and Rotor Balancing*. Second edition edition, 2005.

[3] F. De Jongh. The Synchronous Rotor Instability Phenomenon - Morton Effect. *37th, Turbomachinery Symposium Proceedings*, 2008.

[4] B. L. Newkirk. Shaft Rubbing. *Proaceedings of the American Society of Mechanical Engineering*, pages pp. 830–832, 1926.

[5] A. D. Dimarogonas. Newkirk Effect: Thermally Induced Dynamic Instability of High-Speed Rotors. *ASME Paper No.73-GT-26*, 1973.

[6] J. Schmied. Spiral Vibrations of Rotors. *Proceedings of 11th Biennial ASME Design Engineering Div. Conf., Vib. Noise, DE-Vol2 "Rotating Machinery Dynamics", ASME H0400B, Boston, MA*, pages pp. 449–456, 1987.

[7] P. G. Morton. Some Aspects of Thermal Instability in Generators. *G.E.C. Internal Report No.S/W40 u 183*, 1975.

[8] P. G. Morton. An Interim Note on One Aspect of the Running Characteristics of a Gas Turbine. *G.E.C. Internal Report No. S/W40 u 226*, 1976.

[9] B. Hesseborn. Measurements of Temperature Unsymmetries in Bearing Journal Due to Vibration. *Internal Report ABB Sta*, 1978.

[10] D. Panara, L. Baldassarre, D. Griffini, A. Mattana, S. Panconi, and Meli E. Numerical Prediction and Experimental Validation of Rotor Thermal Instability. *44th Turbomachinery Symposium, College Station, TX*, 2015.

[11] Z. Guo and G. Kirk. Morton Effect Induced Synchronous Instability in Mid-Span Rotor–Bearing Systems - Part I: Mechanism Study. *Journal of Vibration and Acoustics*, Vol. 133, December 2011, 2011.

[12] A. Phuttipongsit. The Morton Effect and Light Rubs in Rotating Machinery. *ORBIT Magazine, 27,(1)*, pages pp. 44–51, 2007.

[13] R. Gomiciaga and P. S. Keogh. Orbit Induced Journal Temperature Variation in Hydrodynamic Bearings. *Journal of Tribology*, Vol. 121: pp. 77–84, 1999.

[14] J. Suh. High Fidelity Simulation of Rotordynamic Morton Effect by Nonlinear Transient Approach. *Ph.D. dissertation, Texas University*, 2014.

[15] B. S. Grigorev, A. E. Fedorov, and J. Schmied. New Mathematical Model for the Morton Effect Based on the THD analysis. *Proceedings of the International Conference on Rotordynamics, Milan 2014 IFTOMM*, 2014.

[16] B.T. Murphy and J.A. Lorenz. Simplified Morton Effect Analysis for Synchronous Spiral Instability. *Proceedings of PWR2009, ASME Power, 21-23 July, Albuquerque, New Mexico, USA*, Paper No. POWER2009-81030, 2009.

[17] J. S. Schmied, J. Pozivil, and J. Walch. Hot Spots in Turboexpander Bearings: Case History, Stability Analysis, Measurements and Operational Experience. *ASME Paper Number GT2008-51179*, 2008.

[18] F. De Jongh and P. Van Der Hoeven. Application of a Heat Barrier Sleeve to Prevent Synchronous Rotor Instability. *27th, Turbomachinery Symposium Proceedings*, pages pp. 17–26, 1998.

[19] A. C. Balbahadur. A Thermoelastohydrodynamic Model of the Morton Effect Operating in Overhung Rotors Supported by Plain or Tilting Pad Journal Bearings. *Ph.D. dissertation, Virginia Polytechnic Institute and State University, Blacksburg, Virginia*, 2001.

[20] F. Berot and H. Dourlens. On Instability of Overhung Centrifugal Compressors. *ASME Paper No. 99-GT-202*, 1999.

[21] J. A. Kocur and F. M. de Jongh. Thermal Rotor Instability in Gas Compressors. *AVPG 14th International Gas Convention, Caracas, Venezuela*, 2000.

[22] R. G. Kirk, Z. Guo, and A. C. Balbahadur. Synchronous Thermal Instability Prediction for Overhung Rotors. *Proceedings of the Thirty-Second Turbomachinery Symposium, Turbomachinery Laboratory, Texas University, Texas*, pages pp. 121–135, 2003.

[23] H. B. Faulkner, W. F. Strong, and R. G. Kirk. Thermally Induced Synchronous Instability of a Radial Inflow Overhung Turbine, Part II. *Proceedings of ASME Design Engineering Technical Conference, Sacramento, California*, 1997.

[24] H. B. Carrick. Integrally Geared Compressors and Expanders in the Process Industry. *IMechE Seventh European Congress on Fluid Machinery for the Oil, Petrochemical, and Related Industries, The Hague, The Netherlands*, 1999.

[25] W. D. Marscher and J. J. McGinley. Experimental Investigation of Cyclic Vibration Morton Effect in the Bearings of a Double Overhung Compressor. *58th Meeting of the Society for Machinery Failure Prevention Technology, Virginia Beach, Virginia*, 2004.

[26] R. Saha. A New, Iterative, Synchronous-Response Algorithm for Analyzing the Morton Effect. *Master of science thesis, Texas University*, 2010.

[27] P. S. Keogh and P. G. Morton. Journal Bearing Differential Heating Evaluation with Influence on Rotor Dynamic Behaviour. *Proceedings of the Royal Society, London, England*, pages pp. 527–548, 1993.

[28] P. S. Keogh and P. G. Morton. The Dynamic Nature of Rotor Thermal Bending Due to Unsteady Lubricant Shearing Within a Bearing. *Proceedings of the Royal Society, London, England*, pages pp. 273–290, 1994.

[29] L. Gu and F. Chu. An Analytical Study of Rotor Dynamics Coupled with Thermal Effect for a Continuous Rotor Shaft. *Journal of Sound and Vibration*, pages pp. 4030–4050, 2014.

[30] W. Kellenberger. Spiral Vibrations Due to Seal Rings in Turbogenerators.Thermally Induced Interaction Between Rotor and Stator. *ASME Paper No. 79-DET-61. Also published in ASME Transactions, Journal of Mechanical Design*, pages pp. 177–184, 1979.

[31] B. Larsson. Heat Flow Induced Alteration of Rotor Response. *Linkoping University, Thesis No 661*, 1997.

[32] A. C. Balbahadur and R. G. Kirk. Part I – Theoretical Model for a Synchronous Thermal Instability Operating in Overhung Rotors. *Proceedings of IFTOMM, Sixth International Conference on Rotor Dynamics, Sydney, Australia*, 2002.

[33] J. G. Lee and A. Palazzolo. Morton Effect Cyclic Vibration Amplitude Determination for Tilt Pad Bearing Supported Machinery. *ASME Journal of Tribology*, Vol. 135, 2013.

[34] D. W. Childs and R. Saha. A New, Iterative, Synchronous-Response Algorithm for Analyzing the Morton Effect. *Journal of Engineering for Gas turbines and Power*, Vol. 134, 2012.

[35] U. Ericsson. Temperature Distribution in the Oil Film of a Vibrating Tilting-Pad Bearting. *Chalmers University of technology, Gotebort, Sweden*, 1980.

[36] B. J. Hamrock, S. R. Schmid, and B. O. Jacobson. *Fundamentals of fluid film lubrication*. New York: Marcel Dekker, 2004.

[37] N. Patir and H.S. Cheng. An Average Flow Model for Determining Effects of Three-Dimensional Roughness on Partial Hydrodynamic Lubrication. *ASME. J. of Lubrication Tech.*, 100(1):pp: 12–17, 1978.

[38] N. Patir and H.S. Cheng. Application of Average Flow Model to Lubrication Between Rough Sliding Surfaces. *ASME. J. of Lubrication Tech.*, 101(2):pp: 220–229, 1979.

[39] Q. Wang, F. Shi, and S.C. Lee. A Mixed-TEHD Model for Journal-Bearing Conformal Contact—Part II: Contact, Film Thickness, and Performance Analyses. *ASME. J. Tribol.*, 120(2):pp: 206–213, 1998.

[40] F. Shi and Q. Wang. A Mixed-TEHD Model for Journal-Bearing Conformal Contacts—Part I: Model Formulation and Approximation of Heat Transfer Considering Asperity Contact. *ASME. J. Tribol.*, 120(2):pp: 198–205, 1998.

[41] W. K. Liu, S. Xiong, Y. Guo, Q. J. Wang, Y. Wang, Q. Yang, and K. Vaidyanathan. Finite element method for mixed elastohydrodynamic lubrication of journal-bearing systems. *International Journal for Numerical Methods in Engineering*, 60:1759–1790, 2004.

[42] M. B. Dobrica, M. Fillon, and P. Maspeyrot. Mixed Elastohydrodynamic Lubrication in a Partial Journal Bearing - Comparison Between Deterministic and Stochastic Models. *ASME. J. Tribol.*, 128:pp: 778–788, 2006.

[43] F. Martelli and G. Manfrida. Some applications of finite element technique in journal bearing hydrodynamics. *Int. Conf. on Numerical Methods in Laminar and Turbulent Flow, University College, Swansea*, 1978.

[44] J. J. Ferron, J. J. Frene, and R. R. Boncompain. A Study of the Thermohydrodynamic Performance of a Plain Journal Bearing Comparison Between Theory and Experiments. *ASME. J. of Lubrication Tech.; doi:10.1115/1.3254632*, pages pp. 422–428, 1983.

[45] M. K. Fitzgerald and P. B. Neal. Temperature Distributions and Heat Transfer in Journal Bearings. *ASME. J. Tribol., 114(1):122-130; doi:10.1115/1.2920850*, 1992.

[46] J. W. Lund and J. J. Tonnesen. An Approximate Analysis of the Temperature Conditions in a Journal Bearing. Part II: Application. *ASME. J. Tribol.; 106(2):237-244. doi:10.1115/1.3260891*, 1984.

[47] G. B. Daniel and K. L. Cavalca. Evaluation of the Thermal Effects in Tilting Pad Bearing. *International Journal of Rotating Machinery, Article ID 725268, doi:10.1155/2013/725268*, vol. 2013, 2013.

[48] M. Fillon, J. Bligoud, and J. Frene. Experimental Study of Tilting-Pad Journal Bearings—Comparison With Theoretical Thermoelastohydrodynamic Results. *ASME. J. Tribol.;114(3):579-587. doi:10.1115/1.2920920*, 1992.

[49] J. D. Knight. Prediction of Temperatures in Tilting Pad Journal Bearings. *Tribology Transactions*, Vol. 33, 1990.

[50] P. P. Monmousseau, M. M. Fillon, and J. J. Frene. Transient Thermoelastohydrodynamic Study of Tilting-Pad Journal Bearings

Under Dynamic Loading. *ASME. J. Eng. Gas Turbines Power; 120(2):405-409. doi:10.1115/1.2818137*, 1998.

[51] S. Taniguchi, T. Makino, K. Takeshita, and T. Ichimura. A thermohydrodynamic analysis of large tilting-pad journal bearing in laminar and turbulent flow regimes with mixing. *ASME Journal of Tribology*, Vol. 112:pp. 542–550, 1990.

[52] A. Z. Szeri. *Fluid Film Lubrication.* Cambridge University Press. doi:.10.1017/CBO9780511626401., 1998.

[53] J. Frene, D. Nicholas, B. Degueurce, D. Berthe, and M. Godet. *Hydrodynamic Lubrication – Bearings and Thrust Bearings.* Elsevier, Trib. Series, 33.

[54] M. M. Reddi. Finite element solution of the incompressible lubrication problem. *ASME Transactions, Journal of lubrication technology*, pages pp 524–533, 1969.

[55] C. A. Felippa. Refined Finite Element Analysis of Linear and Nonlinear Two-Dimensional Structures. *Report No. SESM 66-22, Structural Engineering Lab, University of California*, 1964.

[56] W. F. Cope. The Hydrodynamical Theory of Film Lubrication. *Proc. R. Soc. Lond. A 1949 197 201-217; DOI: 10.1098/rspa.1949.0059*, 1949.

[57] J. W. Lund and P. K. Hansen. An Approximate Analysis of the Temperature Conditions in a Journal Bearing. Part I: Theory. *ASME. J. Tribol.; 106(2):228-236. doi:10.1115/1.3260890*, 1984.

[58] F. Stefani and A. Rebora. Steadily loaded journal bearings: Quasi-3D mass–energy-conserving analysis. *Tribology International*, Volume 42, Issue 3:pp. 448–460, 2009.

[59] C. M. Ettles. The analysis of pivoted pad journal bearing assemblies considering thermoelastic deformation and heat transfer effects. *Tribology Transactions, 35,(1)*, pages pp. 156–162, 1992.

[60] P. Monmousseau, Fillon M., and J. Frene. MTransient Thermoelastohydrodynamic Study of Tilting-Pad Journal Bearings—Comparison Between Experimental Data and Theoretical Results. *ASME. J. Tribol.*, Vol. 119(3):pp. 401–407, 1997.

[61] J.A. Williams. *Engineering Tribology.* Cambridge university press edition, 1994.

[62] T. Verstraete. Multi-Disciplinary Trubomachinery Component Optimization Considering performance, Stress and Internal Heat Transfer. *PhD thesis, Universiteit Gent/von Karman Institute for Fluid Dynamics*, 2008.

[63] J. D. Knight and L. E. Barrelt. Analysis of Axially Grooved Journal Bearings with Heat Transfer Effects. *ASLE Transactions*, Vol. 30, Iss. 3, 1987.

[64] C. H. T. Pan and J. H. Vohr. Super Laminar Flow in Bearings and Seals. *Bearing and seal design in nuclear power machinery, ASME*, pages pp. 219–245, 1967.

[65] G. I. Taylor. Stability of a Viscous Liquid Contained between Two Rotating Cylinders. *Philosophical Transactions of the Royal Society of London, Series A*, Vol. 223:pp. 289–343, 1923.

[66] S. Grossmann, D. Lohse, and C. Sun. High–Reynolds number Taylor-Couette turbulence. *Annu. Rev. Fluid Mech., 48:1, 53-80. doi:10.1146/annurev-fluid-122414-034353.*, 2016.

[67] R. Lueptow. Taylor-Couette flow. *Scholarpedia, 4(11):6389*, 2009.

[68] D. Deng. A Numerical and Experimental Investigation of Taylor Flow Instabilities in Narrow Gaps and their Relationship to Turbulent Flow in Bearings. *Dissertation, University of Akron*, 2007.

[69] R. C. Di Prima. A note on the stability of flow in loaded journal bearings. *ASLE Trans.*, vol. 6:pp. 249–253, 1963.

[70] G. S. Ritchie. On the Stability of Viscous Flow Between Eccentric Rotating Cylinders. *Journal of Fluid mechanics*, vol. 32, part 1:pp. 131–144, 1968.

[71] J. Frene and M. Godet. Transition from laminar to Taylor vortex flow in journal bearing. *J. of Tribology*, vol. 4:pp. 216–217, 1971.

[72] L. Bouard, M. Fillon, and J. Frene. Comparison between three turbulent models: Application to thermohydrodynamic performances of tilting-pad journal bearings. *Tribology International 29(1):11-18*, 1996.

[73] V. N. Constantinescu. On Turbulent Lubrication. *Proceedings of the Institution of Mechanical Engineers*, vol. 173:pp. 881–900, 1959.

[74] V. N. Constantinescu. Basic Relationships in Turbulent Lubrication and Their Extension to Include Thermal Effects. *Journal of Lubrication Technology*, 1973.

[75] V. N. Constantinescu and S. Galetuse. On the Determination of Friction Forces in Turbulent Lubrication. *ASLE Trans.*, Vol. 8:pp. 367, 1965.

[76] G. G. Hirs. A Systematic Study of Turbulent Film Flow. *ASME. J. of Lubrication Tech.; 96(1):118-126, doi:10.1115/1.3451881*, 1974.

[77] J. W. Lund. Spring and Damping Coefficients for the Tilting-Pad Journal Bearing. *ASLE Transactions*, Vol. 7, 1964.

[78] M. He, C. H. Cloud, and J. M. Byrne. Fundamentals of Fluid Film Journal Bearing Operation and Modeling. *Proceedings of the Thirty-Fourth Turbomachinery Symposium, Turbomachinery Laboratory, Texas University, Texas*, pages pp. 155–175, 2005.

[79] J. K. Parsell, P. E. Allaire, and L. E. Barrett. Frequency Effects in Tilting-Pad Journal Bearing Dynamic Coefficients. *ASLE Transactions*, Vol. 26 , Iss. 2, 1983.

[80] J. C. Wilkes and D. W. Childs. Tilting Pad Journal Bearings: A Discussion on Stability Calculation, Frequency Dependence, and Pad and Pivot Flexibility. *ASME Turbo Expo 2012: Turbine Technical Conference and Exposition; Paper No. GT2012-69809, Copenhagen, Denmark*, Volume 7:pp. 991–1006, 2012.

[81] P. E. Allaire, J. K. Parsell, and L. E. Barrett. A pad perturbation method for the dynamic coefficients of tilting-pad journal bearings. *Wear*, vol. 72:pp. 29–44, 1981.

[82] J. Glienicke. Experimental Investigation of the Stiffness and Damping Coefficients of Turbine Bearings and their Application to Instability Prediction. *Proc. IMechE: 181(3B)*, pages pp. 116–129, 1966.

[83] T. Someya, J. Mitsui, J. Esaki, S. Saito, and Y. Kanemitsu. *Journal-Bearing Databook*. Springer-Verlag, Berlin, ed. by t. someya edition, 1989.

[84] K. R. Brockwell and D. Kleinbub. Measurements of the Steady State Operating Characteristics of the Five Shoe Tilting Pad Journal Bearing. *Tribology Transactions*, Vol. 32, Iss. 2, 1989.

[85] P. E. Allaire, J. K. Parsell, and L. E. Barrett. A Pad Perturbation Method for Tilting Pad Journal Bearing Dynamic Coefficients. *UVA Report No. UVA-643092-MAE81-183*, 1980.

[86] N. McCoull and C. Walther. Viscosity–Temperature Chart. *Lubrication vol. 7 no. 6. Texaco Inc., New York*, pages pp. 221–248, 1921.

[87] J. Bouyer. *Etude des performances thermoélastohydrodynamiques de paliers soumis à des conditions sévères*. Theses, Université de Poitiers, October 2003.

[88] I. Pierre, J. Bouyer, and M. Fillon. Thermohydrodynamic behavior of misaligned plain journal bearings: Theoretical and experimental approaches. *Tribology Transactions*, 47(4):594–604, 2004.

[89] R. K. Gadangi, A. B. Palazzolo, and J. Kim. Transient Analysis of Plain and Tilt Pad Journal Bearings Including Fluid Film Temperature Effects. *ASME Journal of Tribology*, Vol. 118:pp. 423–430, 1996.

[90] W. L. Oberkampf, S. M. DeLand, B. M. Rutherford, K. V. Diegert, and K. F. Alvin. Error and uncertainty in modeling and simulation. *Reliability Engineering and System Safety*, Volume 75, Issue 3:Pages 333–357, 2002.

[91] C. J. Roy and W. L. Oberkampf. A comprehensive framework for verification, validation, and uncertainty quantification in scientific computing. *Computer Methods in Applied Mechanics and Engineering*, Volume 200; Issues 25–28:Pages 2131–2144, 2011.

[92] A. D'Ammaro and F. Montomoli. Uncertainty quantification and film cooling. *Computers and Fluids*, Vol: 71:Pages: 320–326, 2013.

[93] F. Montomoli, M. Massini, and S. Salvadori. Geometrical uncertainty in turbomachinery: Tip gap and fillet radius. *Computers and Fluids*, Vol:46:Pages:362–368, 2011.

[94] F. Montomoli, M. Carnevale, M. Massini, A. D'Ammaro, and S. Salvadori. Uncertainty Quantification in Computational Fluid Dynamics and Aircraft Engines. *Springer*, 2015.

[95] F. Montomoli, M. Insinna, A. Cappelletti, and S. Salvadori. Uncertainty Quantification and Stochastic Variations of Renewable Fuels. *ASME Turbo Expo: Turbine Technical Conference and Exposition*, 2015.

[96] R. Tiwari, A. W. Lees, and M. I. Friswell. Identification of dynamic bearing parameters: a review. *Shock and Vibration Digest*, Vol. 36(2):pp: 99–124, 2004.

[97] W. Nicodemi. *Acciai e Leghe non Ferrose*. Zanichelli editore s.p.a., bologna edition, 2000.

[98] C. M. Ettles, H. Heshmat, and K. R. Brockwell. Elapsed time for the decay of thermal transients in fluid film bearing assemblies. *Tribology Series, Elsevier*, Vol. 14:pp. 229–235, 1989.

[99] F. P. Brito. Thermohydrodynamic performance of twin groove journal bearings considering realistic lubricant supply conditions : a theoretical and experimental study. *PhD Thesis, Universidade do Minho*, 2009.

[100] H. Heshmat and O. Pinkus. Mixing Inlet Temperatures in Hydrodynamic Bearings. *ASME JoT*, Vol. 108:pp. 221–248, 1986.